ADVANCES IN SPIN CROSSOVER: SYNTHESIS, MECHANOSYNTHESIS AND SWITCHABLE MULTIFUNCTIONAL HYBRIDS.

David Nieto Castro

UNIVERSITAT ROVIRA i VIRGILI

Advances in Spin Crossover: Synthesis, Mechanosynthesis and Switchable Multifunctional Hybrids

DAVID NIETO CASTRO

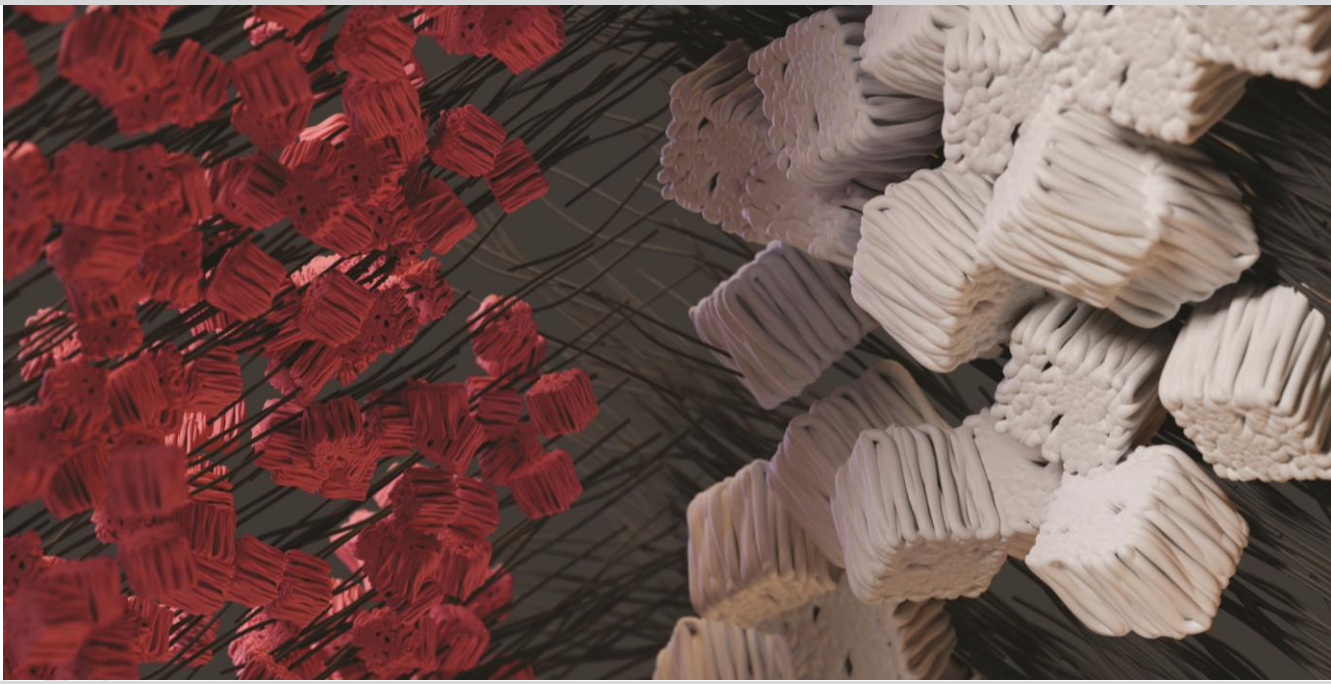

TESI DOCTORAL – TESIS DOCTORAL- DOCTORAL THESIS
2021

David Nieto Castro

Advances in Spin Crossover: Synthesis, Mechanosynthesis and Switchable Multifunctional Hybrids

Doctoral Thesis

Supervised by

Prof. Dr. José Ramón Galán Mascarós

Institut Català d'Investigació Química

Tarragona, 2021

ICIQ
Institut Català d'Investigació Química

UNIVERSITAT ROVIRA i VIRGILI

Prof. Dr. José Ramón Galán Mascarós, Group Leader at the at the Institute of Chemical Research of Catalonia (ICIQ) and Research Professor of Catalan Institution for Research and Advanced Studies (ICREA),

CERTIFIES that the present study entitled "**Advances in Spin Crossover: Synthesis, Mechanosynthesis and Switchable Multifunctional Hybrids**", presented by David Nieto Castro to receive the PhD degree in Chemistry, has been carried out under my supervision, in the Institute of Chemical Research of Catalonia (ICIQ).

Tarragona, 19th November 2021

PhD Thesis supervisor

Prof. Dr. José Ramón Galán Mascarós

Dedicada a mi Yayi, a Mari, a Adri, a Montse y a Floren

“El tipo puede cambiar de todo. De cara, de casa, de familia, de novia, de religión, de Dios. Pero hay una cosa que no puede cambiar. No puede cambiar de pasión.”

Pablo Sandoval – *El secreto de sus ojos*

Acknowledgements

Gracias a mi supervisor, José Ramón Galán Mascarós, por haberme dado la oportunidad de desarrollar mi tesis en su grupo de investigación, dándome gran libertad de investigación, estando siempre disponible para consultas y para discutir ciencia. También me gustaría agradecer a Felipe Andrés Garcés Pineda ya que ha sido como un supervisor para mí, apoyándome en todo momento y dándome nuevas ideas cada día. Los dos sois fuente de inspiración.

Muchas gracias a todos los compañeros de laboratorio que he conocido: Felipe, Vanesa, Jesús, Pili, Ximo, Marta, Álvaro, Franziska, Andrea, Khalid, Breogán, Cristina, Irene, Pavle, Jiahao, Mabel, Anna, Bruno, Stefano, Santi, Juanjo, Scott, Ilario, Neus y Katherine. En especial, gracias Mijo y Andrea, porque más que compañeros sois amigos para toda la vida, os aprecio mucho. Muchas gracias Breo por todo lo que me enseñaste de caracterización, has sido una persona muy importante en mi tesis. Gracias Vanesa por la rapidez en pedir productos y por las risas en la oficina. Agradecer también a JR por todas las victorias en los partidos de ping pong y por todas nuestras conversaciones, mayormente sobre cine. A Laia, por introducirme en el mundo de la divulgación y por lo bien que lo pasábamos en las ferias de ciencia. A José Luis León, por atendernos siempre y dar soluciones. A Francesc Gispert, por toda la ayuda en el análisis de difractogramas y su gran amabilidad.

A Jordi, Débora, Delia, Nacho, Anand y, sobre todo, Ani, por hacer que la comuna fuera mi hogar. Gracias Ani por todos los bonitos e inolvidables momentos en la playa, en las terrazas (siempre con vermut), en casa, en el Cau, en USA y en muchos sitios más. A Ángel, Pablo y Patri por su alegría y por todas las cenas por tarragona. A mis compañeros de correr: Ángel, Felipe, Andrea, Ani y, a veces, Alba. A Àlex, mi némesis en pádel. A Jordi por todas las comidas en la URV. A mis amigos pingboleros, Joan, Leo y Pipe. A Aida, aunque después de 4 años siga sin saber pronunciar su nombre. A las dos Albas y Ana, por querer hacer planes en todo momento. A la terraza más chula de Tarragona, habitada por Leo, Marc, muchas plantas y Marcos. A los miércoles de fútbol. A las chicas del 2.3. A Miquel Purrà por las portadas. A Marc, mi compi de comidas y de chistes

malos, te conocí en el tramo final de mi tesis y has sido un gran apoyo. A mis amigos de Salamanca con los que a pesar de la distancia y gracias a *Whatsapp*, he logrado pasar muy buenos ratos. Al CS:GO, a la música y al cine, por ayudarme a desconectar.

A mis padres, no por esta tesis, sino por toda mi vida, apoyándome en todo momento y haciéndome inmensamente feliz. A mi hermano y mejor amigo, la persona que más admiro en este mundo, no sabes cuanto te quiero. A mi yayi Rosi, por hablar conmigo cada día, manteniéndome informado de quien ganaba en *Pasapalabra*, por todo su amor y por ayudarme a cocinar por teléfono. A mi abuela Mari, por todo el cariño que me diste y las innumerables partidas al parchís y la oca.

La persona que más se merece las gracias es Alba. Muchas gracias por hacer que los días brillen más, por siempre sonreír, por hacerme muy feliz y por hacer que hasta las cosas más sencillas sean especiales.

Index

Summary

Spin crossover (SCO) complexes are molecular materials with d^4–d^7 metal ions that possess a set of properties relevant for practical applications, since they are able to display a spin transition in response to external perturbation, such as a change of temperature, pressure, light irradiation or pulsed magnetic field. To date, many coordination SCO complexes have been studied with different metallic SCO active centres. Among the diverse variety of metal ions, Fe(II) has been the most studied one as, in some cases, the spin transition occurs abruptly, with hysteresis, close to room temperature and is stable over successive cycles. These features make Fe(II) SCO complexes suitable for relevant practical applications in molecular electronics, data storage, display devices, non-linear optics, and photomagnetism.

In the present doctoral thesis, several approaches in the field of SCO have been performed. Firstly, a neutral SCO polymeric chain has been obtained via coprecipitation of mixed-ligand, obtaining the compound with formula $[Fe(L)(NH_2–trz)_2]$ (L = 4−(1,2,4−triazol−4−yl)ethanedisulfonate and NH2–trz = 4NH2−1,2,4−triazole). Secondly, a new compound has been synthesised via mechanosynthesis of L and $Fe(ClO_4)_2$ with completely different magnetic properties and structure than the solution-synthesised SCO compound from the same precursors. Thirdly, the post-synthetic grinding of the well-studied $[Fe(trz)(Htrz)_2]_n(BF_4)_n$ and $[Fe(NH_2–trz)_3]_n(SO_4)_n$ compounds has been used to fine tune their magnetic properties, downshifting the transition temperatures in both of the cases due to a mechanical recrystallization process. Finally, the last mentioned SCO polymers have been successfully inserted into a conductive organic conductive matrix via mechanical processing, obtaining highly conductive hybrid composites with memory effect close to room temperature.

List of Publications

The results of this PhD thesis have delivered the following publications:

D. Nieto-Castro, F. A. Garcés-Pineda, A. Moneo-Corcuera, B. Pato-Doldan, F. Gispert-Guirado, J. Benet-Buchholz, J. R. Galán-Mascarós, Effect of Mechanochemical Recrystallization on the Thermal Hysteresis of 1D FeII–triazole Spin Crossover Polymers. *Inorganic chemistry*, **2020**, 59, 7953. (Chapter 4)

D. Nieto-Castro, F. A. Garcés-Pineda, A. Moneo-Corcuera, I. Sánchez-Molina, J. R. Galán-Mascarós, Mechanochemical Processing of Highly Conducting Organic/Inorganic Composites Exhibiting Spin Crossover–Induced Memory Effect in Their Transport Properties. *Advanced Functional Materials*, **2021**, 2102469. (Chapter 5)

Publications non-related to this thesis:

I. Sánchez-Molina, D. Nieto-Castro, A. Moneo-Corcuera, E. Martínez-Ferrero, J. R. Galán-Mascarós, Synergic Bistability between Spin Transition and Fluorescence in Polyfluorene Composites with Spin Crossover Polymers. *J. Phys. Chem.* **2021**, 12, 10479.

I. Sánchez-Molina, A. Moneo-Corcuera, D. Nieto-Castro, J. Benet-Buchholz, J. R. Galán-Mascarós, Solvent Effect on the Spin State of an Iron (II)-Triazole Trimer. *European Journal of Inorganic Chemistry*, **2021**, 2021, 112.

A. Moneo-Corcuera, B. Pato-Doldan, I. Sánchez-Molina, D. Nieto-Castro, J. R. Galán-Mascarós, Crystal Structure and Magnetic Properties of Trinuclear Transition Metal Complexes (MnII, CoII, NiII and CuII) with Bridging Sulfonate-Functionalized 1, 2, 4-Triazole Derivatives. *Molecules*, **2021**, 26, 6020.

F. A. Garcés-Pineda, M. Blasco-Ahicart, D. Nieto-Castro, N. López, J. R. Galán-Mascarós, Direct magnetic enhancement of electrocatalytic water oxidation in alkaline media. *Nature Energy*, **2019**, 4, 519.

A. Moneo-Corcuera,* D. Nieto-Castro,* C. S. de Pipaón, V. Gómez, P. Maldonado-Illescas, J. R. Galan-Mascaros, Tuning the spin crossover behavior of the polyanion $[(H_2O)_6Fe_3(\mu\text{–}L)_6]^{6-}$: the case of the cesium salt. *Dalton Transactions*, **2018**, 47, 11895.
* These authors contributed equally

Abbreviations

1	$[Fe(NH_2–trz)_3]_n(ClO_4)_n$
2	$[Fe_3(L)_6(H_2O)_6](Me_2NH_2)_6$
3	$[Fe(L)(NH_2–trz)_2]$
4	$[Fe(L)_x]$
5	$[Fe(trz)(Htrz)_2]_n(BF_4)_n$
6	$[Fe(NH_2–trz)_3]_n(SO_4)_n$
10Dq/Δ	Ligand field strength
Δ_c	Critical ligand field strength
ΔE_{HL}	Zero-point energy difference
ΔV	Volume change
ΔT	Hysteresis wideness
γ_{HS}	HS fraction
χ_m	Molar magnetic susceptibility
Γ	Cooperativity
σ	Electrical conductivity
σ_{LS}	Electrical conductivity in the LS state
σ_{HS}	Electrical conductivity in the HS state
AC	Alternating current
BCE	Before current era
C	Curie constant
CE	Current era
CFT	Crystal field theory
DSC	Differential scanning calorimetry
E_a	Activation energy
EDX	Energy dispersive X-ray
EPR	Electron paramagnetic resonance
ESEM	Emission scanning electron microscopy
EXAFS	Extended X-ray absorption fine structure

FESEM	Field emission scanning electron microscopy
FIR	Far-infrared
G	Gibbs energy
H	Enthalpy
H	Applied magnetic field
HS	High Spin
Htrz	4H−1,2,4−triazole
ICP-MS	Inductively coupled plasma mass spectrometry
IR	Infrared
k_b	Boltzmann constant
L	4−(1,2,4−triazol−4−yl)ethanedisulfonate)
LD-LISC	Light-driven ligand-induced spin change
LD-CISSS	Light-driven coordination-induced spin-state
LIESST	Light-Induced Excited Spin State Trapping
LS	Low Spin
M	Magnetization
M_w	Molecular weight
MOF	Metal-organic framework
NH_2−trz	4−Amino−4H−1,2,4−triazole
NMR	Nuclear magnetic resonance
O_h	Octahedral symmetry
P	Pairing energy
PANI	Polyaniline
PEDOT	Poly(3,4−ethylenedioxythiophene)
PEDOT−PT	Poly−(3,4−ethylenedioxythiophene)−paratoluenesulfonate
PEDOT−PSS	Poly(3,4−ethylenedioxythiophene)−poly(styrenesulfonate)
POM	Polyoxometalate
PPY	Polypyrrole
PSM	Post-synthetic modifications

PT	Polythiophene
PXRD	Powder X-ray diffraction
S	Entropy
SCXRD	Single crystal x-ray diffraction
SCO	Spin crossover
SQUID	Superconducting quantum interference device
$\mathbf{S_w}$	Sample weight
SWCNT	Single-walled carbon nanotube
T	Temperature
$\boldsymbol{T_{1/2}}$	Transition temperature
$\boldsymbol{T_{1/2}}\uparrow$	LS→HS transition temperature
$\boldsymbol{T_{1/2}}\downarrow$	HS→LS transition temperature
$\boldsymbol{T_b}$	Blocking temperature
TIESST	Thermal-induced excited spin-state
T(TIESST)	Thermal-induced excited spin-state temperature
TIP	Temperature independent paramagnetism
UV	Ultraviolet
UV-Vis	Ultraviolet-visible
XAFS	X-ray absorption fine structure
XAS	X-ray absorption
XANES	X-ray absorption near the edge structure

Chapter 1. General Introduction

1.1. A brief walk through the history of magnetism

The origin of magnetism dates back to the ancient Greece, where the first observations of natural remanent magnetization in minerals were produced. In 900 BCE at Magnesia, a territory in the northwest of what nowadays is Turkey, a shepherd named Magnes was looking for new grazing pastures and led his flock of sheep to Mount Ida. On the way up, he realized that it was harder to lift his feet each time he stepped on the stones due to the attraction of the stones and the metallic nails in his shoes. This legend was reported a millennium later by Pliny the Elder and some authors have attributed the etymological origin of the word magnetism to the mythological figure of Magnes. However, others attribute the origin of the word magnetism to the cities of Magnesia ad Sipylum or Magnesia ad Maeandrum, two ancient territories whence native iron was extracted for hundreds of years.

Figure 1. Illustration of Magnes the shepherd from a 19th–century text (left). Early Chinese Compass (right).

300 years after (600 BCE), Thales of Miletus discovered that animal fur rubbed with amber produced a similar attraction than iron to lodestone. By the time, this behaviour was associated to the "soul" of the objects, while in reality he was observing static electricity and magnetism. Between the 200 BCE and 100 CE, the compass was invented in China. Shen Kua attached needles to a silk fibre and rubbed its tip with a lodestone, observing that some needles pointed in one direction while others in the opposite one. While first compasses were used to choose suitable areas for building and farming (Figure 1), they were adapted for navigation purposes in 1100 CE. Petrus Peregrinus studied in depth the needles alignment with spherical magnets, distinguishing the north

and south poles, he also described a floating compass for astronomical purposes as well as a dry compass for seafaring.

The origin of the magnetic phenomena remained unsolved until 1600 CE, when William Gilbert hypothesized that the earth is a giant magnet, explaining how compasses work. He also studied how the magnetism and static electricity disappear when heat was applied. However, he did not relate the magnetism and electricity phenomena. Between 1785 and 1789 CE, Charles-Augustin de Coulomb presented his reports in electricity and magnetism, in which he explained the laws of attraction and repulsion between electric charges and magnetic poles. He also calculated the electric force of two electrically charged spheres and developed the Coulomb's law, which postulates that two objects with electric charge exert an electric force on each other which is linearly proportional to the net charge and inversely proportional to the square of the distance between them.

The first connection between magnetism and electricity was made by Hans Christian Ørsted in 1820. He observed that, when approaching a wire with current to a compass, the needle was oriented perpendicular to the wire. Following this experiment, André-Marie Ampère discovered that the direction of the needle depends on the direction of the current. One year later, Michael Faraday began to work in this field and performed the inverse experiment in 1831, producing electricity through magnetic motion. In particular, he moved a magnet inside a coil copper wire, producing current (electromagnetic induction). Faraday also discovered diamagnetism, defined as the opposition of a material to an applied magnetic field, in a heavy piece of glass. Shortly after, Wilhelm Weber postulated that diamagnetism is an intrinsic property to all the compounds and those compounds which, under the influence of a magnetic field, show weak attraction, is due to another intrinsic component of the material (paramagnetism) is higher than the diamagnetic one. This is the case for most elements with unpaired electrons. However, paramagnetism and diamagnetism are weak forces and disappear when the external field is removed. Ferromagnetic, ferrimagnetic and antiferromagnetic materials are other type of magnetic compounds with stronger long-range interactions

along the crystallographic domains, thus being capable to retain the magnetic order (Ferro and ferrimagnets in the same direction than the magnetic field and antiferromagnets in the opposite direction). In 1985, Pierre Curie experimentally studied the correlation among the magnetization of a paramagnetic material (magnetic susceptibility), the applied magnetic field and the temperature, concluding that the magnetic susceptibility of the material is proportional to the applied field and inversely proportional to the temperature, which is known as the Curie's Law.

One of the most remarkable invents in this century was done by Tesla in 1887. He created the induction motor with alternating current (AC) using a rotating magnet field. In 1897, Joseph John Thomson identified the electron as a particle with his experiments with cathode rays and, in the beginning of the 20th century, the electronic and magnetic properties of the materials were attributed to the electrons and their intrinsic charge and rotation and translation movements. Since then, the discovery of new and unusual magnetic properties of previously known and new materials have gathered outstanding scientists to discuss and develop new theories for a better understanding of the magnetic phenomena (see Figure 2 for one of these meetings).

Figure 2. The 1930 Solvay Conference on Magnetism (courtesy of Université Libre de Bruxelles). Back row: Herzen, Henriot, Verschaffelt,Manneback, Cotton, Errera, Stern, Piccard, Gerlach, Darwin, Dirac, Bauer, Kapitza, Brioullin, Kramers, Debye, Pauli, Dorfman, van Vleck, Fermi, Heisenberg. Front Row: de Donder, Zeeman, Weiss, Sommerfeld, Curie, Langevin, Einstein, Richardson, Cabrera, Bohr, de Haas.

1.2. Molecular magnetism

In the middle of the 20th century, the discovery of materials that, at the molecular level, showed unusual magnetic properties which previously had only been attributed to bulk compounds, fascinated both chemists and physicists.[1] The first molecule showing a strong coupling between the metallic centres at the molecular level was the dimer $[Cu_2(OAc)_4(H_2O)_2]$ (OAc = acetate), which was synthesised and analysed by Guha in 1952.[2] One year later, Bleaney and Bowers described the behaviour of this dimer and attributed its decrease in the magnetic susceptibility upon lowering the temperature due to a strong exchange coupling through the acetate bridging ligand.[3] Another inescapable compound in the history of molecular magnetism is the Prussian blue ($Fe_4[Fe(CN)_6]_3 \cdot 14–16H_2O$),[4] whose magnetic properties were analysed in 1962, presenting ferromagnetic order at temperatures lower than 5.6 K. Moreover, its 3D structure allowed assembling other transition metals in its structure. Following this strategy, Prussian blue analogues were synthesised, showing magnetic ordering at much higher temperatures than the original compound, such as 240 K and 376 K for $Cr_3[Cr(CN)_6]_2 \cdot 10H_2O$ (ferrimagnet),[5] and $KV[Cr(CN)_6]_2 \cdot 2H_2O$ (anitiferromagnet), respectively.[6] It was also determined that, for this kind of complexes, the super-exchange interactions could be antiferromagnetic or ferromagnetic depending on the orbital overlapping through the cyanide bridge.[7] Simultaneously to these approaches, Orgel explained an unusual phenomenon nowadays known as spin crossover (SCO), which had been observed decades ago by Cambi and Szegö in tris(N,N-disubstituted dithiocarbamate) iron(III) complexes.[8,9] This phenomenon consists of a spin transition from a low spin (LS) to a high spin (HS) state in some d^4–d^7 metals in an octahedral environment and it is explained by the crystal field theory. Lastly, one of the most recent and fascinating discoveries within the molecular magnetism field took place in the nineties, when the research groups led by Gatteschi, Barbara, Sarachick and Christou and Hendrickson independently reported an unusual behaviour of a Mn_{12} cluster in which Mn(III) ions define an external octagon and Mn(IV) ions an internal tetrahedron linked via acetate bridges.[10–14] At 4 K, this compound showed a hysteresis loop analogous to

a bulk ferromagnet but without magnetic domains. This compound was the first single-molecule magnet (SMMs) and its behaviour was attributed to the coupling between the different Mn centres, producing an energy barrier among the different magnetic sublevels. Since then, there have been major efforts in understanding how chemical structure enhances the wideness of the magnetic hysteresis in SMMs and increases the temperature at which hysteresis can be retained, also known as the magnetic blocking temperature (T_b). To date, the highest T_b achieved has been of 80 K through the use of 4f elements such as Dy(III), presenting high anisotropy and slow relaxations of magnetization.[15]

Among all these approaches, SCO is one of the most remarkable examples of true molecular electronic bistability and memory effect, in which the electronic configuration can switch between two spin states due to external stimuli, exhibiting, in some cases, hysteresis at room temperature. Moreover, this transition is accompanied by modifications in the optical, structural and morphological properties of the compound. For all these features, SCO materials stand as promising building blocks for the fabrication of electronic devices, molecular memories and actuators.

This chapter introduces the general background of the SCO phenomenon with the different types of systems that perform it, remarking the tuning of its properties and showing its potential implementations into devices.

1.3. Spin crossover

1.3.1. First approaches

As previously mentioned, SCO is a particular and interesting phenomenon that occurs in some metals with d^4–d^7 electronic configurations linked to ligands that, in an octahedral configuration, break the energy degeneration of the five *d* orbitals into a subset of three orbitals with t_{2g} symmetry and a subset of two orbitals with e_g symmetry and higher energy. Two scenarios are therefore possible. On the one hand, a large splitting will produce an arrangement of the electrons firstly in the lower energy orbitals, which is known as the low spin state (LS). On the other, a modest splitting will lead to the

electrons be filled with a higher multiplicity in the five orbitals, being this state named as the high spin state (HS). SCO occurs when the ligands produce an intermediate splitting, in which a transition can be induced from the ground LS to the entropically favoured HS state due to external stimuli such as temperature, pressure, light irradiation, magnetic field or insertion of a guest molecule.[16] SCO compounds exhibit different magnetic, structural (difference metal-donor distances), optical and electrical properties in the LS and HS states.

Since the discovery of SCO,[8] and its association to the crystal field theory and the population of the non-degenerated orbitals,[17] novel SCO complexes have been synthesised using *3d* transition metals such as Fe(II), Fe(III), Co(II), Co(III), Mn(II), Mn(III), Ni(III) or Cr(II),[18–20] with new coordination ligands, and their magnetic properties have been analysed in different states of matter (solid, liquid and as soft matter). Moreover, the spin state of Fe(II) and Fe(III) has been demonstrated to have a fundamental role in our organism reactions, when linked to biological molecules like porphyrins enzymes and hemoproteins (myoglobin, hemoglobin and catalase).[21]

During the last decades, a large number of SCO complexes with completely different molecular structures have been obtained using, in most of the cases, Fe(II) as the switching metallic centre. Advancements in coordination chemistry have also allowed designing mononuclear and polynuclear complexes with different magnetic behaviours. Among all the different approaches, one of the most important was the first observations of hysteresis in Fe(II) complexes such as $[Fe(4,7–CH_3)_2phen)_2(NCS)_2]$,[22] or $[Fe(bi)_3](CLO_4)_2$.[23] Hysteresis appears in SCO systems with strong interactions among the SCO centres and opens the door to the use of these bistable materials as molecular switches with memory effect. The next advance in the field occurred in 1982, when McGarvey observed that the LS–HS equilibrium in Fe(II) complexes in solution was perturbed via nanosecond light irradiation at 530 nm. Two years after, Gutlich et al. observed that, in solid state and at low temperatures (T < 50 K), the HS state of $[Fe(ptz)_6](BF_4)_2$ (ptz = 1–propyltetrazole) was gradually populated and trapped after light irradiation.[24,25] This is known as light-induced excited spin state trapping

(LIESST). Hauser extended the LIESST phenomenon, showing that red light switches the system back to the LS state (reverse-LIESST).[26] This photoswitching mechanism opens potential applications for SCO systems in optical writing/magnetic reading for magnetic data storage.[27]

Nowadays, different strategies are followed to obtain new SCO complexes or to modify previously studied materials via new synthetic routes and post-synthetic modifications. Moreover, ligand design and building blocks are used in the pursuit of multifunctional systems to combine the spin switching with other useful properties such as conductivity, photo-luminescence, porosity or sensing.[28]

1.3.2. Crystal field theory

The magnetic properties of SCO compounds can be rationalized on the basis of crystal field theory (CFT). In a coordination complex, CFT describes the breaking of energy degeneration of the electron orbital states due to the electrostatic interaction between the ligand and the orbitals of the metal ion.[29] Depending on the symmetry, the orbitals will interact differently with the located charges from the ligands. For example, in an octahedral complex (O_h), not all the *d* orbitals will interact equally with the six located ligand charges (+x, −x, +y, −y, +z, −z). The orbitals that lie in the axes (the $d_{x^2-y^2}$ and d_{z^2}, with e_g symmetry) will suffer a higher destabilization than those between the axes (d_{xy}, d_{xz} and d_{yz}, with t_{2g} symmetry), provoking two sets of orbitals with an energy barrier between them called ligand field strength, denoted as *10Dq* or Δ_o. Depending on the complex geometry (tetrahedral, square planar, pentagonal, etc.), the splitting of the *d* orbitals will be completely different (Figure 3).

10Dq is also affected by the nature of the metal ion and its oxidation state and by the nature of the ligands. The spectrochemical series, based in the absorption data for a wide variety of complexes, arranges some ligands in order of their increasing splitting power:[30]

$I^- < Br^- < S_2^- < SCN^- < Cl^- < N_3^-$, $F^- < CO(NH_2)_2$, $OH^- < O_2^- < H_2O < NCS^-$ < pyridine, NH_3 < ethylenediamine < bypiridine < $NO_2^- < CH_3^- < C_6H_5^- < CN^-$ < CO.

Ligands on the left are generally regarded as weak field ligands (cause lower splitting) and those on the right as strong field ligands (cause larger splitting). Ligands with localized charges interact more strongly with the metal orbitals, producing higher *10Dq* values, as observed in the halides. However, the difference in the strength is more dependent on the donor or acceptor abilities of the ligands, π and σ donor ligands show higher metal–ligand interactions and produce weaker *10Dq*, opposite than acceptor ligands with vacant antibonding or *d* orbitals.

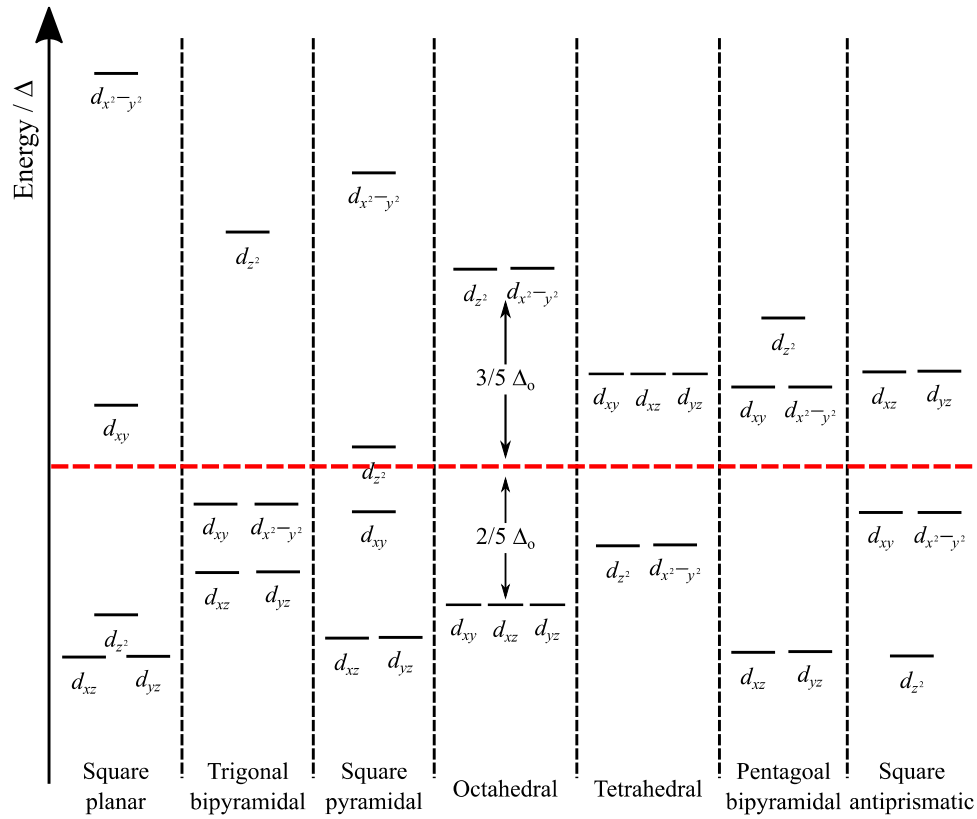

Figure 3. Crystal field splitting in different coordination symmetries.

Following the Aufbau principle and Hund's rule, the electronic configuration of coordination complexes with d^4–d^7 transition metal ions is determined by the *10Dq* and the spin-pairing energy (*P*). For cases in which *10Dq* is greater than *P*, the electrons are arranged in the set of orbitals with lower energy: t_{2g} firstly filled and then e_g orbitals, following the Aufbau principle and adopting the low spin (LS) configuration. In contrast, if *10Dq* < *P*, the electrons are filled in order to have highest number of unpaired electrons

(Hund's rule), resulting in the high spin (HS) configuration. Particularly, for *10Dq* values close to *P*, it is possible to switch between the LS and HS state upon external stimuli, like temperature, pressure, or light, or in other words SCO phenomenon.[31] In this last situation and taken Fe(II) ($3d^6$) as an example, the $t_{2g}^6\ e_g^0$ diamagnetic LS configuration ($S = 0$), can be triggered to the triply degenerated $t_{2g}^4 e_g^2$ paramagnetic HS state ($S = 2$) by an extrinsic perturbation (Figure 4). This spin transition involves changes not only in the magnetic behaviour, but also in the metal to ligand bond distances, which changes due to the population or depopulation of the antibonding e_g orbitals. In Fe(II) SCO compounds, the spin transition produces a 5–15% increase in the Fe–N bond lengths and a change in colour, usually from pink (LS) to white (HS).

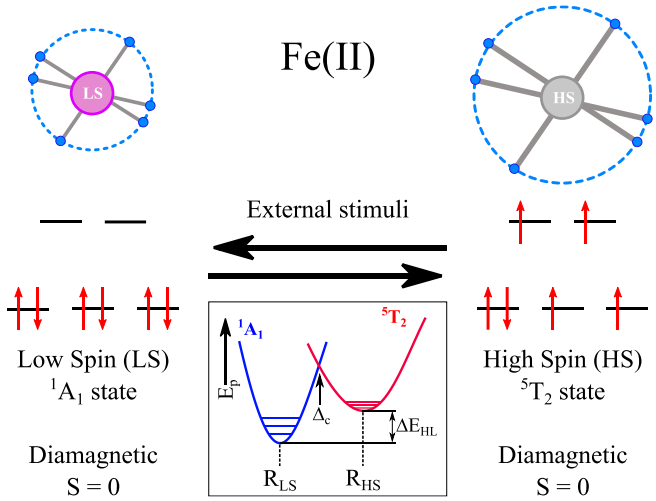

Figure 4. Scheme of the two possible electronic states for Fe(II) in an octahedral complex. The inset includes the potential energy of the LS ($^1A_1$) and HS ($^5T_2$) states.

An important contribution to CFT was made by Tanabe and Sugano, who studied the absorption spectra of transition metal coordination complexes in octahedral configuration and, using the Racah parameters,[32] calculated the energy of all the electronic states in the different configurations.[33] These diagrams are very useful to predict absorptions in UV, visible and IR spectrum. In addition, they can be used to approximate the *10Dq* value of coordination complexes. Figure 5 shows the Tanabe-Sugano diagrams for d^4, d^5, d^6 and d^7 configurations in octahedral geometry, whose spin

states are found in the HS state for low *Dq* values (maximum multiplicity) until the critical ligand field strength (Δ_c) is reached, blue dashed line in the diagrams, which corresponds to the crossing point of the LS and HS potential wells (Figure 4, inset). For higher values of *Dq* than Δ_c, the LS state becomes the ground state.

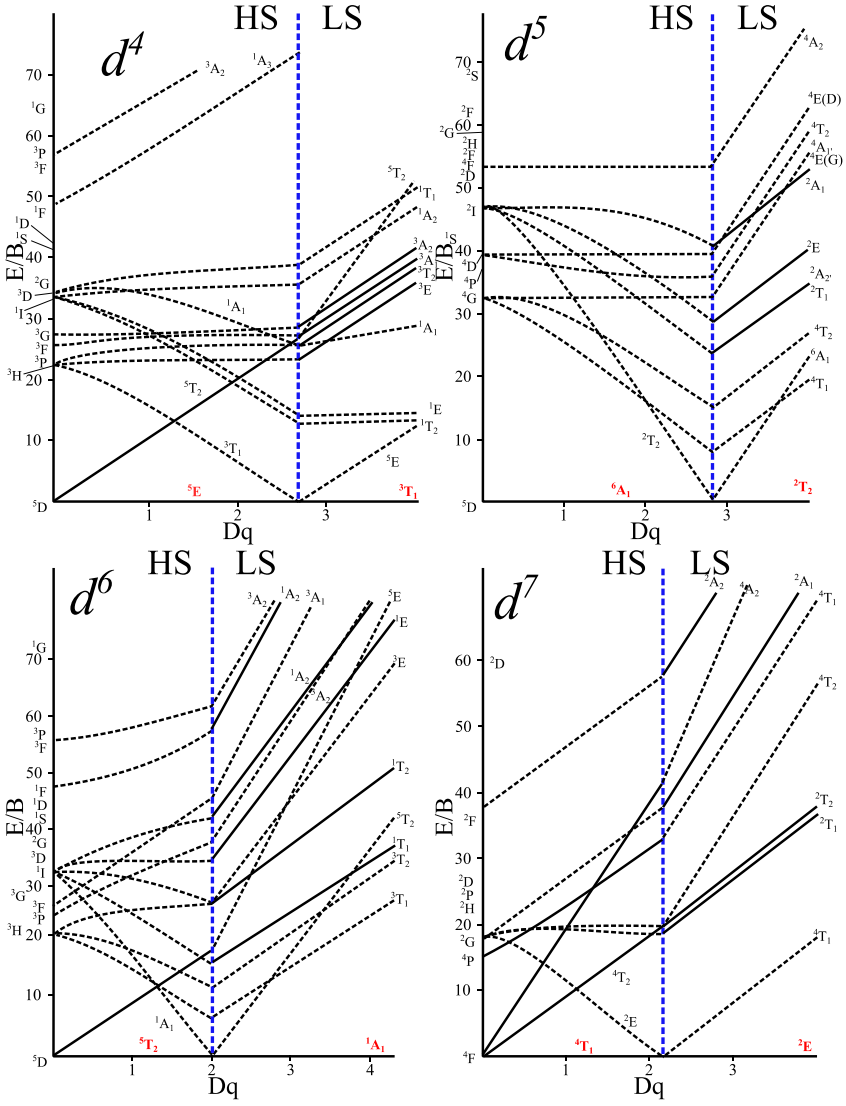

Figure 5. Tanabe-Sugano diagrams for d^4, d^5, d^6 and d^7 electronic configurations. Solid lines correspond to the allowed spin transitions ($\Delta S = 0$) and dashed lines correspond to the not allowed transitions. The ground states is red marked and the blue dashed line represents the critical ligand field strength (Δ_c).

1.3.3. Detection of the SCO transition

As previously described, the spin transition is accompanied by changes in different chemical and physical features, allowing the study and quantification of the properties with different techniques. The most used ones will be described in this section.

Magnetic susceptibility measurements

The number of unpaired electrons is directly related to the molar magnetic susceptibility (χ_m) of the material and, for SCO complexes, the LS state is less paramagnetic than the HS state. χ_m is calculated applying the following equation:

$$\chi_m = \left(\frac{M}{H}\right) \cdot \left(\frac{M_w}{S_w}\right) \qquad \text{Equation 1}$$

Where M is the magnetization of the sample, H the applied magnetic field, M_w the molecular weight of the sample and S_w the sample weight. χ_m is expressed in emu/mol. $\chi_m \cdot T$ product vs T is the typical way to plot the magnetic properties of a thermal induced SCO compound. HS fraction (γ_{HS}) vs T plot is also used to represent the magnetic susceptibility of a compound. The equation to calculate the γ_{HS} is:

$$\gamma_{HS} = \left(\frac{\chi T - \chi_{LS}}{\chi_{HS} - \chi_{LS}}\right) \qquad \text{Equation 2}$$

Where χ_{LS} and χ_{HS} are the magnetic susceptibilities in the LS and HS state, respectively.

Some complexes which are expect to have a $\chi_m T$ value of 0 emu·K/mol, like Fe(II) in the LS state (S = 0), present residual paramagnetism from defects in the structure, from the sample holder or due to temperature independent paramagnetism (TIP). This residual paramagnetism can be completely corrected using the Curie Weiss law:[34]

$$\chi = \left(\frac{C}{T - \theta}\right) + \chi_{residual} \qquad \text{Equation 3}$$

Where C is the Curie constant and θ the correction term or Weiss constant.

Magnetic susceptibility measurements are usually performed in the solid state, using a superconducting quantum interference device (SQUID). A technique to measure the magnetic properties in solution is the Evans NMR method.[35] Electron paramagnetic

resonance (EPR) can also be used to obtain information about the unpair electrons in a compound and is normally used to follow the spin transition of paramagnetic transition metals like Fe(III). There are also tools to measure the magnetization structure of materials such as the magneto-optic Kerr microscope, based in how light interacts with a magnetic surface.

X-ray diffraction

As previously described, the bond distances between the SCO active centre and the ligand increase during the LS→HS transition. This produces a distortion and expands the unit cell, increasing the distances between the planes (d) which is related with θ by the bragg's law (Equation 4). In this situation, θ should decrease to maintain $n\lambda$ constant.

$$n\lambda = 2d \cdot sen(\theta) \qquad \text{Equation 4}$$

If single crystals of the SCO can be obtained, then the crystallographic structure can be determined by single crystal X-ray diffraction (SCXRD) at different temperatures, providing information of the cell parameters and symmetry in the LS and HS states.

Synchrotron techniques can be also used to determine the crystal properties of the compound in both spin states, using X-ray absorption (XAS) near the edge structure (XANES) or extended X-ray absorption fine structure (EXAFS).

Mössbauer spectroscopy

Mössbauer effect involves the resonant absorption of gamma radiation by an atomic nuclei bond in solids. On the basis of the isomer shift and quadrupole splitting values, the spin states of SCO complexes can be assigned. ^{57}Fe Mossbauer spectroscopy is used for Fe(II) compounds. In addition, this technique is element specific and proportional to the fraction of spin state, enabling an easy quantification.

Optical spectroscopy

Tanabe-Sugano plots give us information about the electronic transitions in the UV-Vis and IR. Different transitions are allowed to happen in the LS or HS states. For example in a Fe(II) compound, d^6 configuration, in the LS state the $^1A_1 \rightarrow {}^1T_1$, $^1A_1 \rightarrow {}^1T_2$, $^1A_1 \rightarrow {}^1A_2$ transitions are allowed (3 peaks), meanwhile in the HS state the only transition allowed

is the $^5T_2 \rightarrow {}^5E$ (1 peak). Thus, the transition can be easily followed via UV-Vis or IR spectroscopy. Raman spectroscopy, that detects how a molecule scatters incident light from a high intensity light source, can also give information about the chemical structure. Moreover, many SCO complexes present thermochromism. In most of Fe(II) triazole-based SCO, there is a change from pink (LS) to white (HS).

Differential scanning calorimetry

In some cases, the SCO transition is accompanied by a phase transition that involves an absorption or heat release. Thus, differential scanning calorimetry (DSC) can give information about the spin transitions.

1.3.4. Thermal driven spin transition

Among all the external perturbations to induce SCO, temperature is the most extended one. The thermoinduced SCO is possible when the difference between the zero-point energies of the LS and HS states, defined by the sum of the electronic and vibrational contributions (ΔE_{HL} in Figure 4), have the same order of magnitude than the thermal energy (Equation 5).

$$\Delta E_{HL} = E_0^{HS} - E_0^{LS} \sim k_B T \qquad \text{Equation 5}$$

Where k_B is the Boltzmann constant.

From the measurements of the HS fraction (γ_{HS}) vs T in solid systems, different behaviours have been observed depending on the interactions among the SCO active centres (Figure 6). In systems with weak interactions among the SCO centres, similar than to solution behaviour, the transition occurs following a Boltzmann distribution, performing a gradual transition (Figure 6a) that, in some cases, may be incomplete (Figure 6b). In these cases, the SCO transition can be thermodynamically explained by the Gibbs equation at constant pressure (Equation 6)

$$\Delta G = G_{HS} - G_{LS} = \Delta H - T \cdot \Delta S \qquad \text{Equation 6}$$

where $\Delta H = H_{HS} - H_{LS}$ and $\Delta S = S_{HS} - S_{LS}$ are the enthalpy and entropy variations, respectively. At low temperatures, enthalpy dominates the Gibbs energy, being the zero-point energy the LS state. Whereas, at high temperatures, the HS state becomes the

thermodynamic stable state due to the entropic contributions from the higher spin multiplicity.

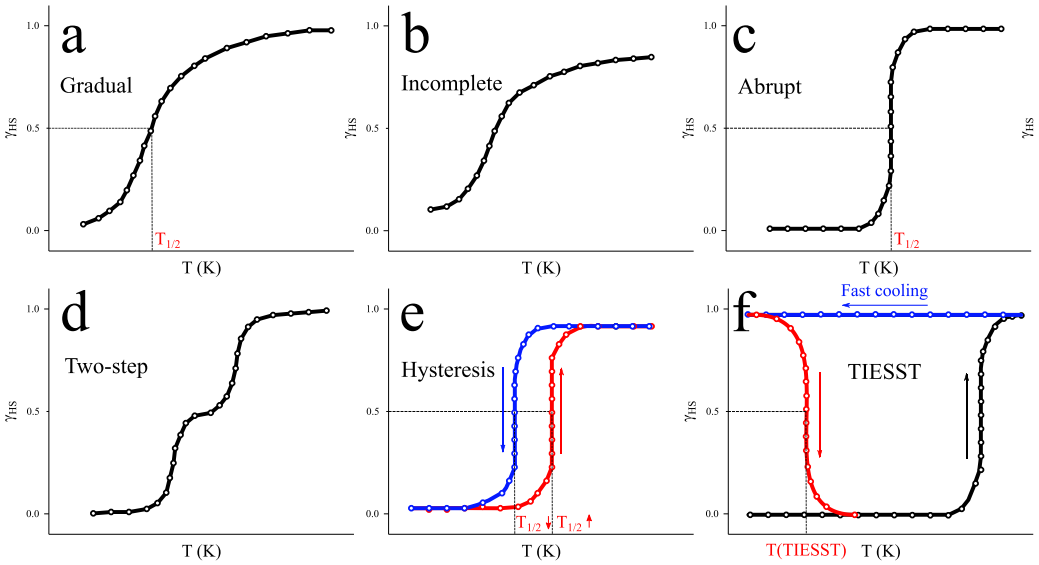

Figure 6. Types of thermal spin transitions plotted as γ_{HS} vs T.

In solid systems, the transition does not follow a Boltzmann distribution, as in the crystal packing, a change in the structural properties affects the whole lattice.[36] The volume expansion, induced by the spin transition, produces compressive stress in the neighbouring molecules, playing a significant role in the SCO behaviour. These systems show abrupt transition (Figure 6c) that, in some occasions, can occur in several steps (Figure 6d) and, exceptionally, might be accompanied by a hysteresis loop (Figure 6e).

The thermal hysteresis is characterized by the wideness of the hysteresis (ΔT) and its transition temperatures $T_{1/2}(\uparrow)$ and $T_{1/2}(\downarrow)$, defined as the temperatures at which 50% of the SCO centres have reached the HS state in the heating and cooling branches, respectively.

In order to predict this kind of behaviours, Drickramer and Slitcher introduced the first thermodynamic model in which they introduced the concept of cooperativity (Γ), proposing the following expression:

$$T = \frac{\Delta H + \Gamma(1-2\gamma_{HS})}{R\ln(\frac{1-\gamma_{HS}}{\gamma_{HS}})+\Delta S} \qquad \text{Equation 7}$$

$$\left(\frac{\partial^2 G}{\partial^2 \gamma_{HS}}\right)_{T,P,\gamma_{HS}=0.5} = -2\Gamma + 4RT_{1/2} \qquad \text{Equation 8}$$

Inspecting the second derivative (Equation 8), three situations can be described:

- For $\Gamma < 2RT_{1/2}$ (Figure 7, blue line), the transition is continuous and gradual, showing a minimum point of Gibbs energy.
- For $\Gamma = 2RT_{1/2}$ (Figure 7, black line), the transition is abrupt without hysteresis.
- For $\Gamma > 2RT_{1/2}$ (Figure 7, red line), there is a temperature range ($T_b<T<T_a$) where three solutions are possible, where the two extremes (T_a and T_b) correspond to the transition temperatures ($T_{1/2}(\uparrow)$ and $T_{1/2}(\downarrow)$, respectively).

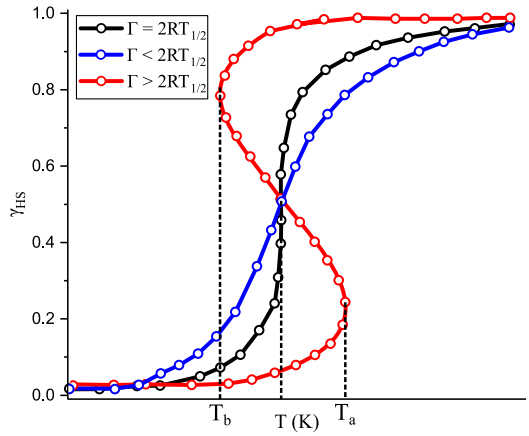

Figure 7. Simulated spin transition curves (γ_{HS} vs T plot), according to equation 7 with different cooperativity values (Γ).[36]

The last of the profiles (Figure 6f) shows how, in some SCO systems, the HS state can be trapped in a metastable–HS state via fast scan rates (> 10 K/min). This phenomenon is known as temperature-induced excited spin-state trapping (TIESST) and is characterized by the metastable–HS→LS relaxing temperature ($T(TIESST)$), obtained by slow increase of the temperature (0.3 K/min).[37]

1.3.5. Light driven spin transition

Since the discovery of light driven spin transition phenomenon,[24] different irradiation phenomenon have been studied to promote photo-induced processes like photothermal irradiation or due to the interaction of the light with the ligands. The latest is the case of light-driven ligand-induced spin change (LD-LISC), based in the cis-trans or photocyclization of the photoisomers, and of light-driven coordination-induced spin-state switching (LD-CISSS), where light causes coordination/dissociation of the species.[38–40]

In the case of light-induced excited spin state trapping (LIESST), the used wavelength produces *d*–*d* or metal–ligand charge transfer transitions. Numerous investigations have clarified the mechanism of LIESST.[41] For example, in a d^6 complex the excited singlet states $^1T_{1g}$ and $^1T_{2g}$ can be populated by light irradiation from the fundamental $^1A_{1g}$ state. These states have a short lifetime and decay to the lowest spin triplet state and via intersystem crossing fill the $^5T_{2g}$ HS state (Figure 8).

As the $^5T_{2g} \rightarrow {}^1A_{1g}$ is forbidden, this state remains stable unless other perturbation (temperature or reverse-LIESST) occurs. LIESST is monitored via magnetic susceptibility measurements. First, the sample is cooled down at 10 K, followed by light irradiation until saturation, then light is switched off and, finally, sample is heated up at a 0.3 K/min scan rate. This last heating process produces the relaxation from the metastable HS state to the LS state and the temperature at which occurs is known as *T(LIESST)*. Different studies have concluded that cooperativity induces self-acceleration and non-linear behaviours, increasing the relaxations kinetics of the phenomenon.[42] Moreover, LIESST occurs mostly in non-cooperative systems and its *T(LIESST)* can be increased with the denticity of the ligands and with the distortion of the coordination sphere.[38]

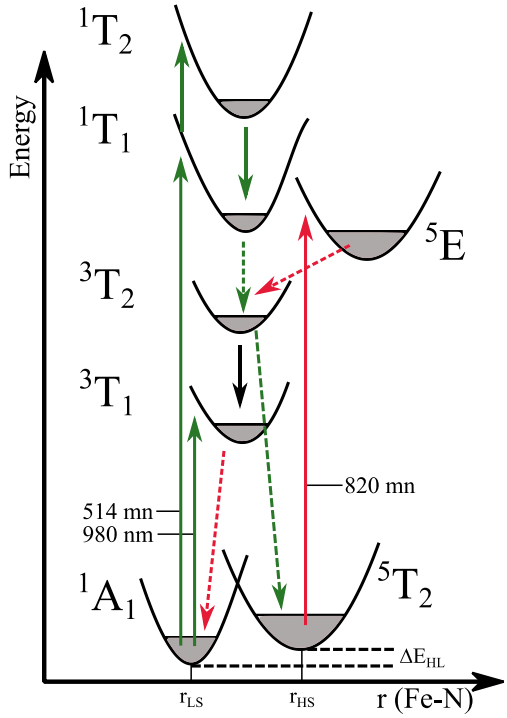

Figure 8. Schematic mechanism of LIESST (green) and reverse LIESST (red) phenomenon in a d^6 SCO complex. Spin allowed *d*–*d* transitions and relaxation processes are denoted by full and dashed lines, respectively.

1.4. 1,2,4–Triazole based iron(II) SCO

1,2,4–trizaole derivative are the most used ligands for the obtention of SCO complexes, as they can bridge metal ions through five different coordination modes (Figure 9). Protonated or 1/4–functionalized–1,2,4–triazole, also known as 1/4H–1,2,4–triazole or 1/4R–1,2,4–triazole (R = functional group) can link two metals via its 1,2 or 1,4 positions ($\mu_{1,2}$ and $\mu_{1,4}$ respectively), meanwhile the deprotonated triazole (triazolate) can be able to coordinate two or three metal ions ($\mu_{1,2}$, $\mu_{1,4}$ and $\mu_{1,2,4}$), providing infinite possibilities for designing new ligands and, thus, a wide range of mononuclear and polynuclear structures. Nevertheless, most of this kind of coordination complexes remain in the HS state due to the too weak ligand field provided by the triazole ligands.

However, there are several exceptions when complementary strong donor group are used as substituents or when strong supramolecular interactions occur in the network.[43,44]

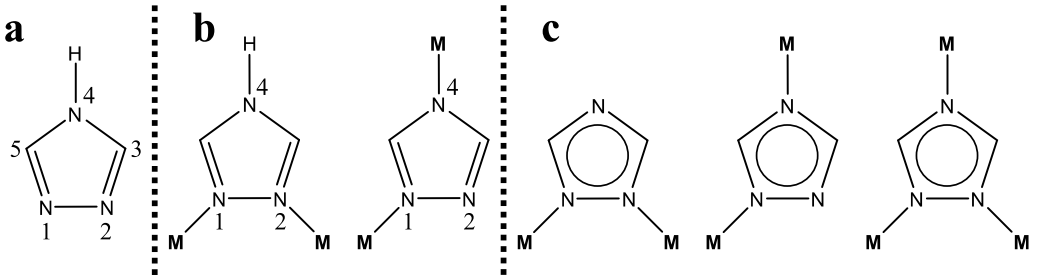

Figure 9. structure of 4H–1,2,4–triazole (a), binding modes of 4H–1,2,4–triazole (b) and of 1,2,4–triazolate (c).

1.4.1. Mononuclear complexes

Mononuclear Fe(II) SCO compounds have been obtained with monodentate, bidentate and tridentate chelating 1,2,4–triazole derivatives. As previously mentioned, due to the weak crystal field, in most of the cases, HS state is stabilized. For SCO mononuclear complexes, the transition observed is usually gradual without hysteresis. One example of a mono-coordinating ligand in a SCO complex is the bis{hydrotris(1,2,4–triazolyl)borato}Fe(II), in which one nitrogen is linked to the metal ion and the other one to a boron atom (Figure 10a). This compound showed a gradual spin transition in solid and solution.[45] The 3–(pyridin–2–yl)–1,2,4–triazole (Hpt) bidentate ligand led to the formation of $[Fe(Hpt)_3](BF_4)_2 \cdot 2H_2O$ with a gradual and incomplete spin transition (Figure 10b).[46] 2,6–Bis(triazol–3–yl)pyridine (Figure 10c) was used to obtain a tri-coordinating SCO complex, with formula [Fe(2,6–bis(triazol–3–yl)pyridine)2]$Cl_2 \cdot 3H_2O$, that remains in the HS state at room temperature and exhibits a partial transition to the LS state upon cooling.[47]

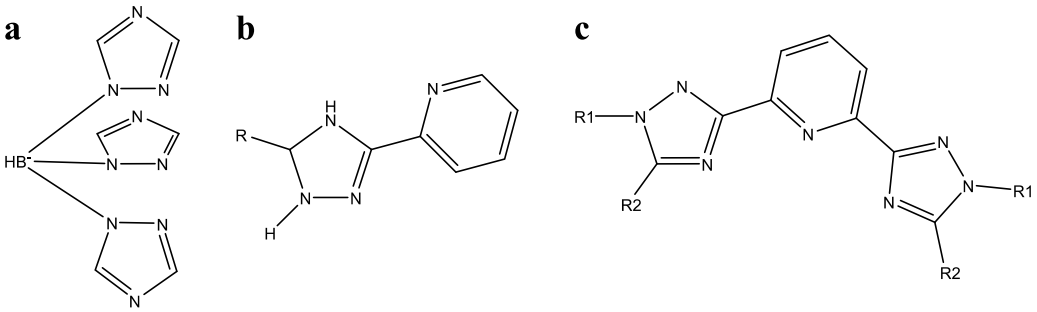

Figure 10. Structures of (1,2,4–triazolyl)borato (a), 3–(pyridin–2–yl) –1,2,4–triazole (b) and 2,6–Bis(triazol–3–yl)pyridine (c).

1.4.2. Dinuclear complexes

Dinuclear complexes are of great interest as they are discrete molecules that can present three spin states (LS–LS, HS–LS or HS–HS), giving the possibility to store the information in multi-states and not only in binary code.[48] Some examples of dinuclear complexes are $[Fe_2(PMAT)_2](BF_4)_4 \cdot DMF$ (Figure 11a for PMAT structure), which exhibit an abrupt transition at 224 K,[49] or $[Fe(NCBH_3)(py)]_2(l–bpytz)_2$ (py = 3,5–bis(2–pyridyl) –1,2,4–triazolate) (Figure 11b).[50] The latest complex shows a two-step SCO transition, suggesting that the Fe(II) centers can be in the HS–HS, HS–LS or LS–LS configurations. Another interesting example is the $[Fe_2(N–salicylidene–4–amino–1,2,4–triazole)_5(NCS)_4]$ (Figure 11c for the ligand structure). In this case, the two Fe(II) centres are linked by three triazole ligands and complete their octahedral configuration with another triazole and two NCS^-. In this case, the cooperative transition occurs without intermediate LS–HS state and, as the ligand shows photochromism, the dinuclear compound is fluorescent, allowing to follow the transition through luminescence measurements.[51]

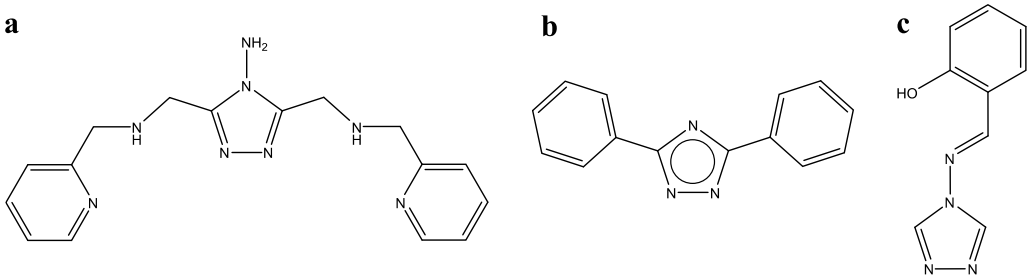

Figure 11. Structures of PMAT (a), 3,5–bis(2–pyridyl) –1,2,4–triazolate and N–salicylidene–4–amino–1,2,4–triazole (c).

1.4.3. Trinuclear complexes

Most of the trinuclear SCO active complexes are linear species where the metal ions are linked by triple bridges made of 1,2,4–triazoles. The first structurally trinuclear SCO active compound was the $[Fe(4–Ettr)_2(H_2O)_2]_3(CF_3SO_3)_6$ (4–ettr = 4–ethyltriazole, Figure 12a). Crystals of this compound can be isolated, like in most trinuclear, dinuclear and mononuclear complexes, allowing the structure determination in the different spin states and revealing that the only SCO active centre is the central Fe(II).[52] Trinuclear complexes always respond to the general formula $[Fe_3(trz)_6(L)_6](A)_6$, where trz is the triazole derivative ligand, L is a neutral monodentade ligand that complete the outer Fe octahedral environment, and A^- the counterion. In Figure 12, nime more ligands that lead to trimers when mixed with Fe(II) salts following different routes are included.[43,44]

In 2014, with the purpose of obtaining the first trimeric anionic specie, our group synthetized the 4–(1,2,4–triazol–4–yl)ethanesulfonate ligand (Figure 12b) that, reacting with Zn^{2+}, Cu^{2+}, Ni^{2+}, Co^{2+}, and Fe^{2+}, gave trinuclear neutral complexes with formula $[M_3(L)_6(H_2O)_6]$. In the as-synthetized Fe(II) trimer, the three iron centres were in the HS state (HS–HS–HS) and a gradual HS→LS transition is observed in the central iron at 150 K. Upon dehydration at 35ºC under N_2 for 3 h, a crystallographic phase transition occurs in which the central iron remains in LS state at room temperature. Surprisingly, this dehydrated phase displays an abrupt transition with memory effect ($T_{1/2}(\uparrow)$ = 357 K and $T_{1/2}(\downarrow)$ = 343 K and ΔH = 14 K) similar the observed in a SCO polymer. [53]

One year later, a trimer with a similar structure than the previous described was reported. In this case, the ethanesulfonate functional group of the 1,2,4-triazole was substituted by ethanedisulfonate (4–(1,2,4–triazol–4–yl)ethanedisulfonate Figure 12c). This new complex showed one of the widest thermal hysteresis with $T_{1/2}(\uparrow)$ = 400 K and $T_{1/2}(\downarrow)$ = 310 K (ΔH = 14 K) and thermal-induced spin-state trapping (TIESST) with a *T(TIESST)* of 240 K.

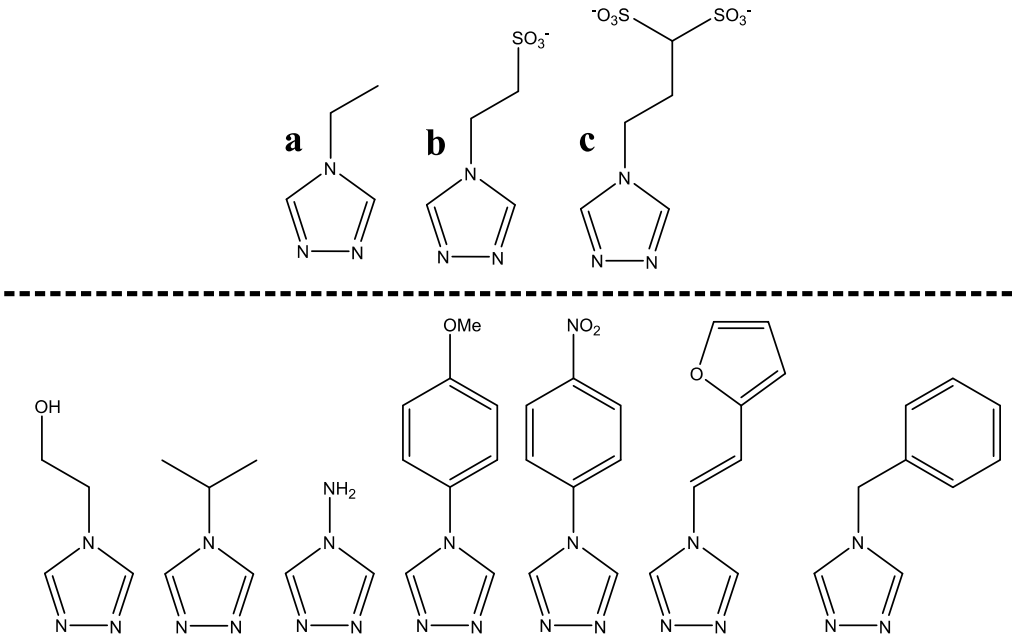

Figure 12. Structures of 4–ethyltriazole (a), 4–(1,2,4–triazol–4–yl)ethanesulfonate (b) and 4–(1,2,4–triazol–4–yl)ethanedisulfonate (c). seven 1,2,4–triazole based ligands that lead to trimer complexes are included (bottom).[43]

1.4.4. 1D polymers

Only a few multi-dentate ligands can be appropriate to create a true infinite coordination structure and the appropriate ligand field strength to observe SCO behaviour. Coordination chains have been only obtained with discrete 4-substituted triazoles, as bulky substituents such as quinoline or tertbutyl impede the formation of extended chains.

These compounds hardly crystallize and its polymer structure was firstly determined using Cu(II) analogues: $[Cu(hyetrz)_3](CF_3SO_3)_2 \cdot H_2O$, $[Cu(hyetrz)_3](ClO_4)_2 \cdot 3H_2O$ (hyetrz = 4–(2'–hydroxyethyl) –1,2,4–triazole]),[54] and $[Cu(NH_2–trz)_3]X_2$ (X = BF_4, SiF_6 and BF_4^-/SiF_6^{2-}).[55] Synchrotron X-ray powder diffraction analysis (EXAFS and WAXS) and Raman spectroscopy were used to obtain more information about the structure of these kind of complexes.[56,57] To date, the 1D polymer structure (Figure 13) has been also confirmed in single crystals of $[Fe(bntrz)_3][Pt(CN)_4] \cdot H_2O$ (bntrz = 4–(Benzyl) –1,2,4–triazol) and $[Fe(NH_2–trz)_3](NO_3)_2 \cdot nH_2O$ and refining high crystalline powder samples of $[Fe(NH_2–trz)_3](SO_4)$ and $[Fe(Htrz)_2(trz)](BF_4)$.[58–61]

The SCO transitions of the 1D polymers are expected to be abrupt given the long-range connectivity between the active centres as they are linked by covalent bonds and not only by Van der Waals forces among isolated molecules. Unfortunately, many 1D structures perform incomplete or multi-step transitions with intermediate phases.[44]

Different strategies have been developed to fine-tune the magnetic properties of 1D SCO polymers, based on new synthetic routes, post-synthetic modifications or modifying some chemical parameter with no alteration of the molecular structure but obtaining completely new properties. These approaches will be addressed in section 1.5.

1.4.5. 2D and 3D complexes

1,2,4–triazole ligands may also act as terminal ligands to yield 2D and 3D networks. Regarding to 2D complexes, one example is the $[Fe(NCS)_2(4,4'–bis–1,2,4–triazole)_2] \cdot H_2O$, which shows a hysteresis of 21 K with transition temperatures of 123 and 144 K for $T_{1/2}(\uparrow)$ and $T_{1/2}(\downarrow)$, respectively.[62] Another example is the 2D material synthetized with the ligand 4–(2–pyridyl) –1,2,4,4H–triazole. In this Fe(II) 2D framework, a transition from a HS–HS state to a HS–LS state is observed at 153 K but the only way to reach the LS–LS state is via near infrared (830 nm) irradiation at 10 K.[63]

The first 3D SCO compound was reported in 1999, the formula of the compound was $[Fe(btr)_3](ClO_4)_2$ (btr = 4,4′–bis–1,2,4–triazole). This compound has a two-step SCO transition with a plateau of 20 K. The btr ligand was also used to obtain 1D or 2D complexes when other coordinating anions are present (NCS^-). In the absence of this kind of ions, the 3D structure is favoured.[64] Recently, 3–methyl–2–(5–(4–(pyridin–4–yl)phenyl)–4H–1,2,4–triazol–3–yl)–pyridine)(Hmptpy) was used to synthetize a 3D chiral MOF $[Fe(Hmptpy)_2]$ exhibiting also a two-step spin transition.[65,66]

1.5. Regarding 1D SCO polymers

1,2,4–triazole based 1D coordination polymers have attracted much interest due to their SCO properties, easy preparation and processability and chemical stability.[67] Figure 13 represents a typical scheme of 1D SCO chain formed by Fe(II) centers linked by 4R–1,2,4–triazole based ligands. As previously described this kind of materials display abrupt magnetic and chromatic spin transition, exceptionally accompanied by a hysteresis loop.

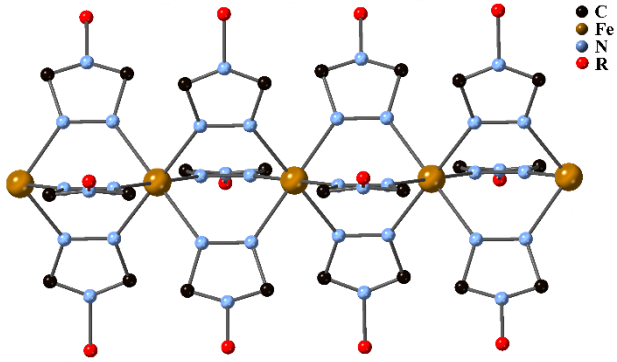

Figure 13. Structure Fe(II) 1D polymeric chains.

Two of the most studied 1D SCO polymer chains are $[Fe(Htrz)_2(trz)](BF_4)$ and $[Fe(NH_2–trz)_3](SO_4)$. Indeed, all the chapters of this thesis are related to them. Figure 14, left shows the $\chi_m T$ of $[Fe(Htrz)_2(trz)](BF_4)$ in the 280–400 K range. The abrupt transitions, with $T_{1/2}(\uparrow)$ = 382 K and $T_{1/2}(\downarrow)$ = 343 K, define a wide hysteresis loop of ΔT = 39 K. In the case of $[Fe(NH_2–trz)_3](SO_4)$ (Figure 14, right), the hysteresis loop is much

narrower, ΔT = 21 K, but with transition temperatures closer to room temperature, $T_{1/2}(\uparrow)$ = 349 K and $T_{1/2}(\downarrow)$ = 328 K. These two compounds have been deeply studied due to its abruptness and close to room temperature hysteresis, being great candidates for memory storage applications, actuators and sensors.

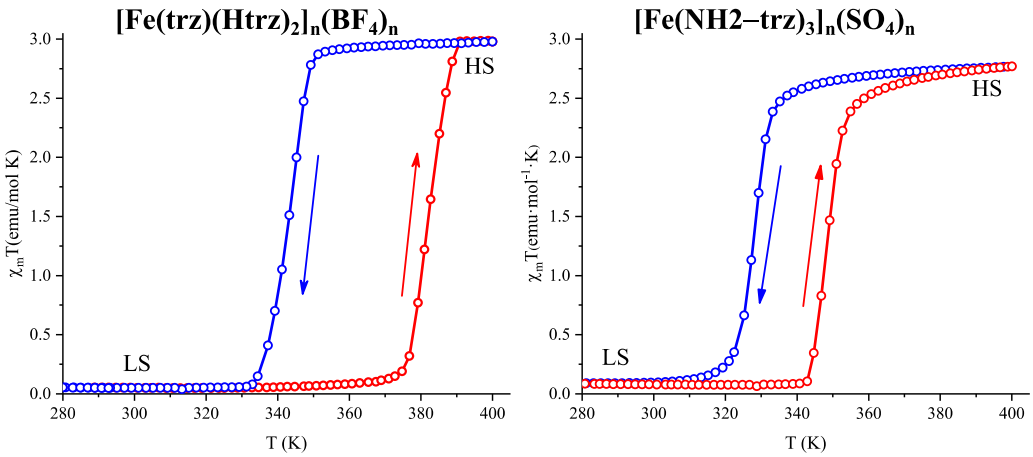

Figure 14. Magnetic properties of $[Fe(Htrz)_2(trz)](BF_4)$ (left) and $[Fe(NH_2–trz)_3](SO_4)$ (right). The warming branch is represented with the red colour and the cooling branch with blue colour.

1.5.1. Synthesis of 1,2,4–triazole derivates 1D SCO polymers

The synthesis of $[Fe(4R–1,2,4–trz)_3](A)_x$ compounds (A = anion, x = 1 or 2 for divalent or monovalent anions, respectively) is easily achieved by the reaction of the respective Fe(II) salt with the selected triazole ligand with a 1:3 ratio in solution, obtaining high yields.[67] Organic solvents such as methanol, ethanol DMF, THF can be the reaction media. However, the coprecipitation reaction can be done in aqueous solution after adding an antioxidant agent, usually ascorbic acid, to avoid the Fe(II) oxidation. In most of the cases, the precipitation reaction occurs rapidly, leading to insoluble powders and hampering the obtention of crystals. However, there are exceptions like the highcrystalline structure of $[Fe(NH_2–trz)_3](SO_4)$ obtained via simple co-precipitation, as previously mentioned in section 1.4.4.[60]

Recently, mechanosynthesis was used as a new synthetic approach for the obtention of SCO materials. This solvent-free procedure offers advantages over conventional chemical synthesis in solution, such as rapidity, high selectivity, high yields and less energy consumption. Askew and shepherd synthetized $[Fe(NH_2–trz)_3](SO_4)$ by mixing the two solid reagents, $[Fe(SO_4)_2](NH_4)_2·6H_2O$ and $NH_2–trz$, in a mortar for 5 minutes without any solvent (Figure 15a caption). Figure 15 shows the comparison of the magnetic properties of the solution-synthetized and the mechanosynthetized compounds. Despite $T_{1/2}(\uparrow)$ and $T_{1/2}(\downarrow)$ were similar, the powder diffraction patterns of the samples showed additional peaks, attributed to irreversible structural differences due to the water loss of the lattice.[68] In the same publication, the authors extended this synthesis approach to the mononuclear Fe(II) SCO $[Fe(phen)_2(NCS)_2]$ (phen = 1,10–phenanthroline), the 3D hofmann-like $[Fe(pz)\{Au(CN)_2\}_2]$ (pz = pyrazine) and $[Fe(NH_2–trz)_3](BF_4)_2$.

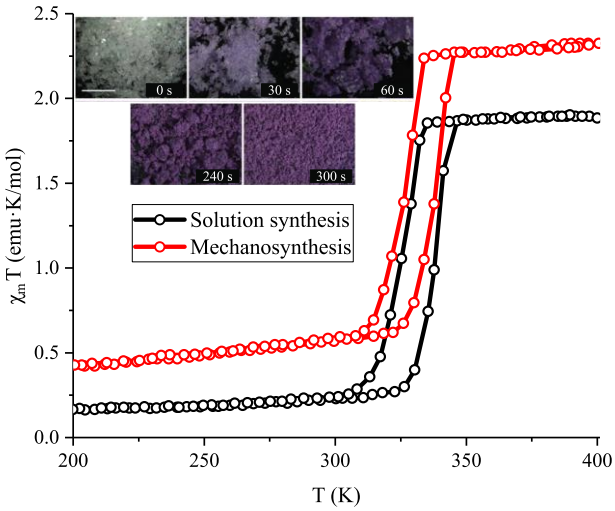

Figure 15. $\chi_m T$ vs T measurements of $[Fe(NH_2–trz)_3](SO_4)$ prepared in solution (black) and via mechanosyntesis (red).[68]

Motivated by the miniaturization of next generation devices, new synthetic routes have been developed for the obtention of SCO nanoparticles. In 2007, stable nanoparticles of $[Fe(trz)(Htrz)_2](BF_4)$ up to 10 nm size were prepared using the reverse micelle technique.[69] Remarkably, this nanoparticles preserved the spin transition of the bulk

material. Years later, this procedure was improved by adding more surfactant ratio and using faster centrifugation, obtaining smaller nanoparticles (4 nm).[70,71] In this case, the effect of reducing the size of the nanoparticles from 18 nm to 4 nm resulted in a significant decrease of the hysteresis width (from 38 to 24 K) due to the decrease in cooperativity when the chain is shortened (Figure 16a).

A similar trend was observed in the 3D Hoffman clathrate $Fe(pz)[Pt(CN)_4]\cdot 2H_2O$ (pz = pyrazine) (Figure 16b). In this research, they also observed that the transition abruptness remarkably decreased and the remaining HS fraction increased upon downsizing.[31] To overcome the limitation of the quenching of the cooperativity, Mallah et al covered $[Fe(pz)(Pt(CN)_4)]$ (pz = pyrazine) with a rigid matrix made of silica, restoring the hysteresis loop.[72]

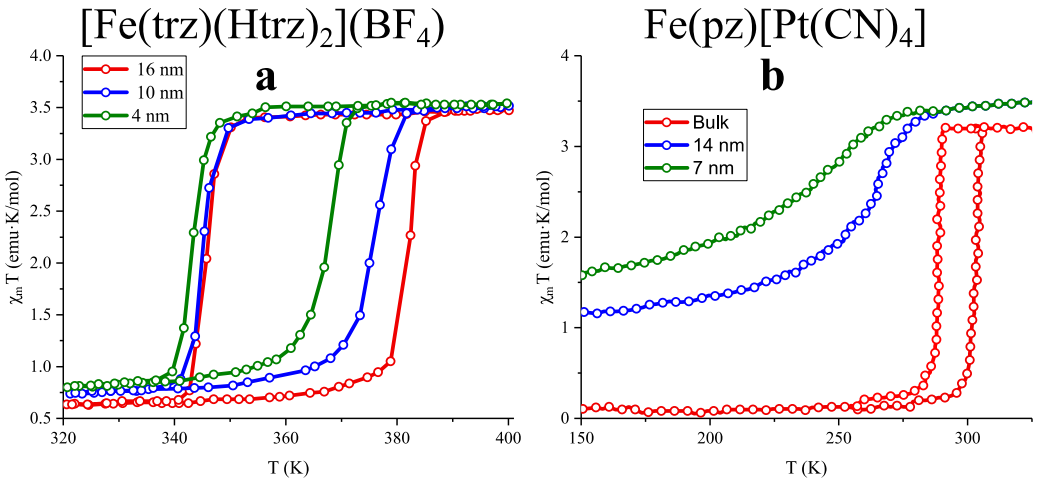

Figure 16. $\chi_m T$ vs T plots for different sized particles of $[Fe(trz)(Htrz)_3](BF_4)$ (a) and $Fe(pz)[Pt(CN)_4]$ (b).[31,70]

1.5.2. Chemical modifications of 1,2,4–triazole derivates 1D SCO polymers

The four chemical factors that can induce changes in the magnetic properties are the nature of the R group in the 4R–1,2,4–trizaole, doping with non SCO active centers, the change of the counteranion and the presence of crystallographic solvent molecules in the structure.[67]

Regarding to the nature of the R group, it has been pointed that the *n*–alkyl tails in the 4R substituent of the triazole results in a steady decrease of the transition temperatures (Figure 17a).[73] Moreover, Similar R substituents in the triazole can induce changes in the magnetic properties. This is the case of 4H–1,2,4–trizaole and $4NH_2$–1,2,4–trizaole reacting with $Fe(ClO_4)_2$ to lead the 1D polymers. $[Fe(trz)(Htrz)_2](ClO_4)_2$ shows a transition with hysteresis above room temperature ($T_{1/2}(\uparrow)$ = 375 K and $T_{1/2}(\downarrow)$ = 333 K), whereas $[Fe(NH_2{-}trz)_2](ClO_4)_2$ exhibits a transition at low temperatures and with a narrow hysteresis ($T_{1/2}(\uparrow)$ = 217 K and $T_{1/2}(\downarrow)$ = 212 K). Due to the similarities in the molecular structures for 1D polymers with similar 4R substituents, "molecular alloys" have been studied. The general formula of these kind of alloys is $[Fe(R_1{-}trz)_{3-3x}(R_2{-}trz)_{3x}]X_2{\cdot}nH_2O$. In the case of $[Fe(Htrz)_{3-3x}(NH_2{-}trz)_{3x}](ClO_4)_2{\cdot}nH_2O$, the transition temperatures were found to vary linearly as a function of concentration (Figure 17b). The alloy with x = 0.05 was the first SCO compound exhibiting bistability at room temperature.[74,75]

Another kind of alloys are those in which some SCO active metal centres are substituted with non SCO active metallic ions, such as Cd, Mn, Zn, Co or Ni in the 2+ oxidation state. It has been extensively reported that metal doping produces a strong effect in the magnetic and photomagnetic properties of polynuclear species.[76,77] For example, metals such as Cd(II) and Mn(II), which are larger than Fe(II) in HS, stabilize the HS state by exerting a "negative" internal pressure, decreasing the transition temperatures. Zn(II) and Co(II) with similar sizes than Fe(II) in HS also stabilize the HS state, downshifting $T_{1/2}$. On contrary, Ni(II), with an intermediate radius between those in HS and LS Fe(II), tends to stabilize the LS state.[78]

The dilution effect has been studied in a wide range of trinuclear compounds. In the family of 1D polymers, dilution effects were studied in $[Fe_xZn_{1-x}(btzp)_3](BF_4)_2$ and $[Fe_xZn_{1-x}(endi)_3](BF_4)_2$ (btzp = 1,2–bis(tetrazol–1–yl)propane and endi = 1,2–bis(tetrazol–1–yl)ethane) alloys (Figure 17c). As expected, the dilution induces a progressive loss of cooperativity, since the SCO active centres become further away. The HS state is, as previously mentioned, stabilized due to the similar radii between

Zn(II) (r = 74 pm) and HS Fe(II) (r = 78 pm).[79] The doping also produces a decrease in the charge carrier hopping frequencies.[80]

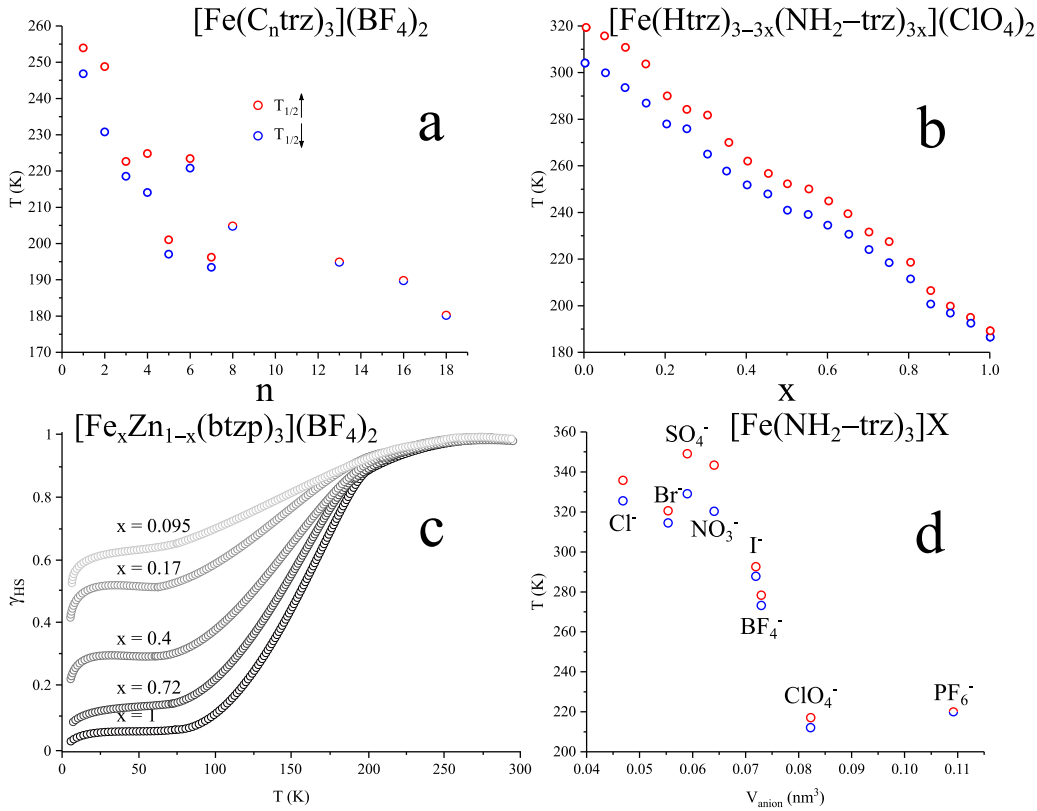

Figure 17. Transition temperatures for $[Fe(C_ntrz)_3](BF_4)_2$ (a).[73] effect of (Htrz)/(NH_2–trz) ratio in the transition temperatures of the $[Fe(Htrz)_{3-3x}(NH_2–trz)_{3x}](ClO_4)_2$ (b).[75] Zn doping effect in $[Fe_xZn_{1-x}(btzp)_3](BF_4)_2$ (c).[79] $T_{1/2}$ Countercation dependence for $[Fe(NH_2–trz)_3]X$ chain (d).[67]

Counteranion dependence in the magnetic behaviour plays a key role in the packing of the structure and in the interchain distances. It is well stablished that, for the same 4R–1,2,4–trziazole ligand, the transition temperatures are found to increase with the size of the counteranion. As observed in Figure 17d, there is a near-linear dependence with the volume of spherical anions and the magnetic properties in $[Fe(NH_2–trz)_3]X_2$, where X = Cl^-, Br^-, I^-, NO_3^-, BF_4^-, ClO_4^-, SO_4^{2-}, and PF_6^-.[67]

To conclude with the chemical modifications, solvent-dependency in the SCO properties has been also studied. The insertion of non-coordinated solvent molecules can stabilize the LS state. This is the case of $[Fe(hyetrz)_3](3–nitrophenylsulfonate)$ (hyetrz = 4–(2′–hydroxyethyl)–1,2,4–triazole). The transition of the non-solvated compound (105 K) can be modified when solvated with DMA (145 K), MeOH (175 K), DMF (235 K) or with $3·H_2O$ (LS at room temperature).

1.5.3. Processing of 1D SCO materials

Post-synthetic modifications (PSM) have attracted the interest of many research groups to tune properties or give new features to synthesized materials.[81] PSM gives the possibility to create new materials from the same precursor compound, preserving the features of its solid-state structure. However, this strategy has not been deeply studied in SCO materials. First PSM approaches were based in the post-synthetic grafting of the fluorophore on the 1D SCO $[Fe(NH_2–trz)_3]_n(ClO_4)_{2n}$ for the obtention of fluorescence-SCO materials, resulting in new SCO compounds with different transition temperatures.[82,83] In 2019, Bousseksou et al converted the complex $[Fe(NH_2–trz)_3](NO_3)_2$ into $[Fe(L2)_3](NO_3)_2$ (L2 = (E) –N–(4–Methoxybenzylidene)–4H–1,2,4–triazol–4–amine) via a 72h post-synthetic reaction between $[Fe(NH_2–trz)_3](NO_3)_2$ and p-anisaldehyde. Moreover, alloys with formula $[Fe(NH_2–trz)_{3–x}(L2)_{3x}](NO_3)_2$ were obtained playing with the reaction time (Figure 18a).[84] Recently, the same group demonstrated the efficiency and versatility of PSM, being able to synthetize new compounds, which are not accessible using the direct synthesis.[81]

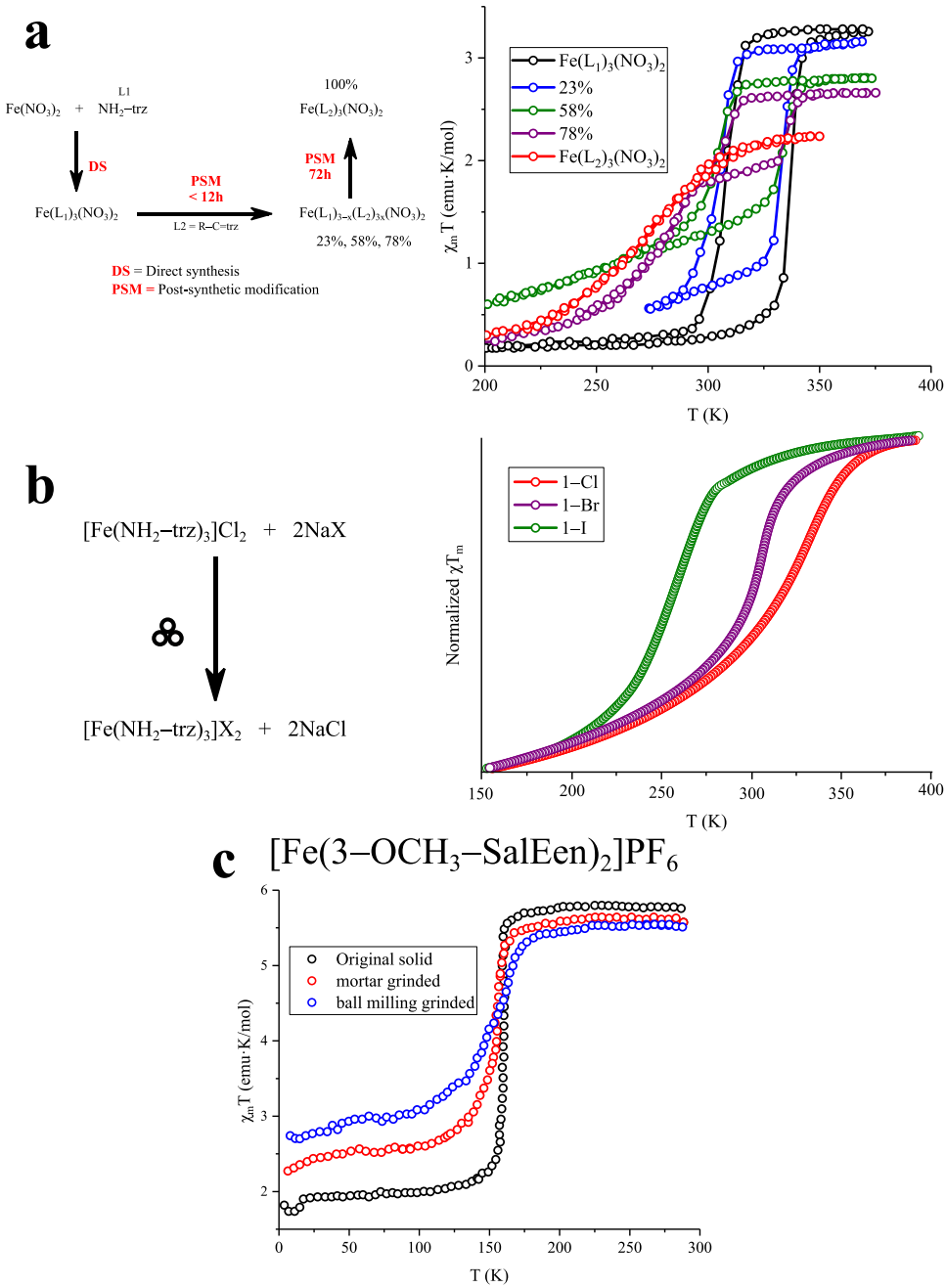

Figure 18. Scheme of the post-synthetic modification and magnetic properties of the initial, final and intermediate SCO compounds (a).[84] Post-synthetic exchange of the Cl^- anion for Br^- and I^- in $[Fe(NH_2–trz)_3]Cl_2$ by mechanochemistry (b).[85] grinding effects in the $[Fe(3–OCH_3–SalEen)_2]PF_6$ (c).[86]

A similar approach was used to exchange the Cl^- anion for Br^- and I^- through solid state metathesis reaction, grounding $[Fe(NH_2–trz)_3]Cl_2$ with the corresponding sodium salt in a mortar.[85] The chloride anions were fully exchanged for bromide and iodide using excess of the sodium salts, obtaining SCO complexes with the expected properties for $[Fe(NH_2–trz)_3]I_2$ and $Fe(NH_2–trz)_3]Br_2$ but with a slight decrease in $T_{1/2}(\uparrow)$ and $T_{1/2}(\downarrow)$, attributed to the grinding procedure (Figure 18b). Post-synthetic grinding effects in Fe(III) SCO complexes were also studied in the past by Hendrickson et al. [86–89] In these reports, they observed that grinding led to gradual and incomplete transitions with a downshift in $T_{1/2}$ and a decrease of the enthalpy and entropy of the phase transition (Figure 18c). They assigned changes to the generation of defects in the crystalline structure.

1.6. Road to technological applications of SCO

As exposed along the previous sections, SCO complexes offer a remarkable versatility due to its change in their magnetic, optical, mechanical and electrical properties. Thus, this paradigmatic compounds are very promising as components in molecular switches, optoelectronic devices, actuators and sensors.[90] In this section, some attempts to realize the true potential of SCO materials in next generation devices will be described.

1.6.1. Actuating applications

Actuators are devices that convert a source of energy into motion. Typical actuators are made of bimetallic strips that produce motion under thermal stimuli due to the different thermal expansion of the components. SCO compounds expansion upon transition is usually around 5%, but values up to 15% have been obtained for framework SCO materials like {Fe(pyrazine)$[Pt(CN)_4]$}. Moreover, the transition in some SCO complexes is close to room temperature, accompanied by hysteresis and can performe LIESST or TIESST. For all of these features, many groups decided to fabricate actuators from different SCO.[91–94] A recent example is the elaboration of a centimeter-scale bilayer actuator device compromising a 50 μm film of polyester coated with a 22 μm thick film of $[Fe(trz)(Htrz)_2](BF_4)$ composite. This cantilever showed macroscale

mechanical movements induced by the volume change of the SCO and was able to lift weight upon temperature raise (Figure 19).[95]

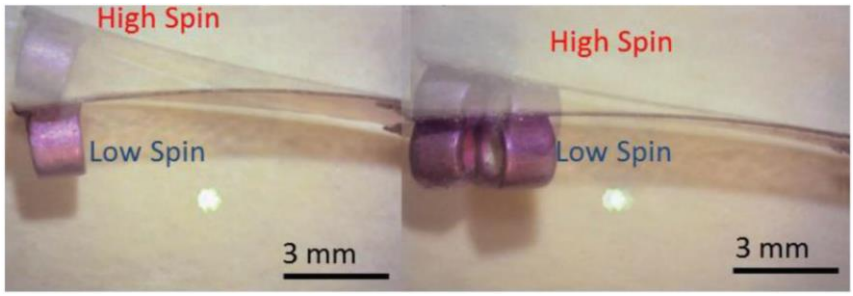

Figure 19. Bilayer cantilevers actuated by SCO. The attached loads (purple rings) weigh 4.785 mg (left) and 9.57 mg (right). Cantilever dimensions are 11 × 2 × 0.075 mm^3.[95]

1.6.2. Optical applications

The first display incorporating a SCO compound was fabricated by Kahn et al.[96] In this report, $[Fe(trz)(Htrz)_2](BF_4)$ was dispersed over an alumina plate with resistive dots able to dissipate and release heat, allowing to write and erase "pixels" depending on the spin state of the SCO complex.

More recent reports have tried to combine SCO and luminescence due to its potential application in the field of drug delivery, biomarkers or thermometry. Fluorescence is a sensitive probe and SCO may provide a modulation on the signal. A common approach in this field consists in the incorporation of fluorophores in the ligands attached to the metal centre. In these studies, a small increase in the fluorescence was observed upon the spin transition.[97,98] A more effective strategy was the combination of SCO material and fluorophores into hybrid composites. For example, SiO_2 nanoparticles with a core of $[Fe(trz)(Htrz)_2](BF_4)$ and an organic luminescent coating on the surface, have shown great synergy between SCO and fluorescence. As represented in Figure 20, luminescence decreases as a function of temperature due to the thermal activation of non-radiative relaxation channels but, upon the LS→HS and HS→LS transitions, it abruptly increases or decreases, respectively. This fact can be explained by an energy transfer mechanism between the SCO and the fluorophore, as observed in the overlap between the LS absorption band and the excimer emission at 525 nm.[99,100] More

approaches in the same direction have been reported with quantum dots,[101] or with Fe(II) –triazole nanoparticles doped with rhodamine.[102]

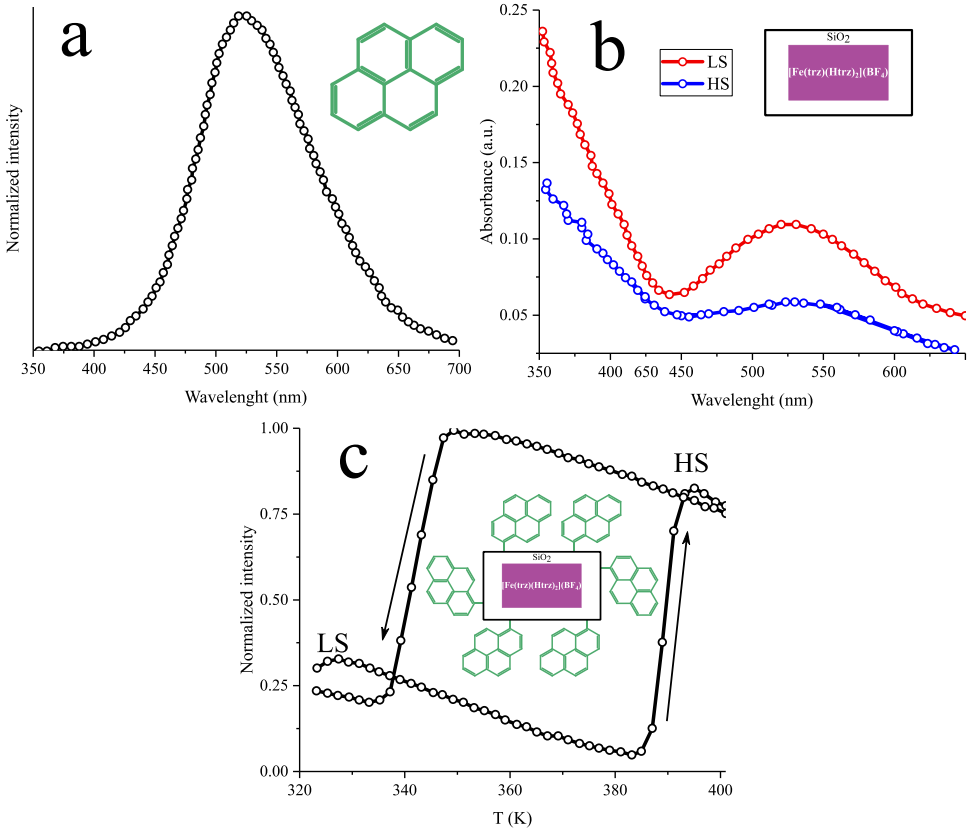

Figure 20. Emission spectra (λ_{exc} = 348 nm, T = 293 K) of the pyrene attached to the NPs (a), absorption spectra of the SCO complex in the LS (293 K) and HS (400 K) states (b) and normalized excimer luminescence intensity recorded at 550 nm as a function of the temperature (c).[99]

1.6.3. Sensors

Novel materials are needed as sensors to face challenges as climate change, ecological collapse, health prevention, food quality or safety. In this direction, Metal Organic Frameworks (MOFs) have been presented as new promising materials for sensing devices.[103] SCO–MOFs can be used for sensor applications due to its changes in the physico-chemical properties associated with the spin transition. In the case of the porous

SCO compound Fe(pyrazine)[Pt(CN)$_4$], chemo-switching at room temperature was demonstrated using different guest molecules like CS_2 or benzene. In this example, guest molecules such as N_2, O_2 and CO_2 did not produce any change in the magnetic properties; H_2O, MeOH or EtOH stabilized the HS state; and CS_2 stabilized the LS state (Figure 21). Theoretical studies attributed this different stabilizations to the absorbed molecule interactions with the pz–bridges or with the Pt centers of the framework.[104] SCO–MOFs can be also used as sensors for failure of pressure or temperature in some industrial processes.[103]

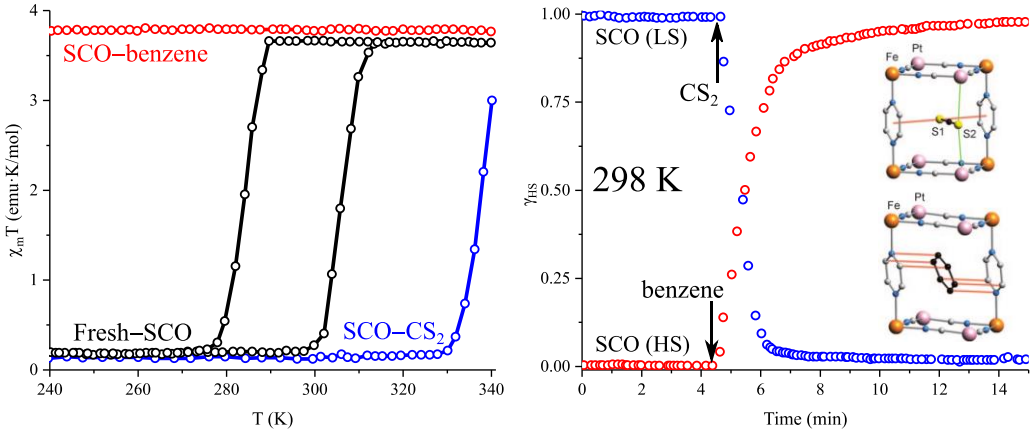

Figure 21. Magnetic behaviours of fresh Fe(pyrazine)[Pt(CN)$_4$](black) and with benzene (red) and CS_2 as guest molecules in the porous (left). γ_{HS} vs time dependence of Fe(pyrazine)[Pt(CN)$_4$] under benzene (red) and CS_2 (blue) atmosphere at 298 K. The arrows indicate the starting guest injection. The inset shows the interactions with between the host molecule and the different sites of the framework (right).[104]

1.6.4. Conducting applications

The direct exploitation of SCO compounds in electronic devices is limited due to their very high insulating nature. As [Fe(trz)(Htrz)$_2$](BF$_4$) is one of the more studied SCO complexes, its implementation into electronic devices has been arduously studied. This compound behaves as an electrical insulator in the LS and HS state.[105,106] In 2011, Coronado et al. reported a switchable molecular device fabricated by placing individual nanoparticles, made of [Fe(trz)$_3$](BF$_4$)$_2$ coated with a surfactant shell, in between two

nanometer-spaced gold electrodes. Thermal hysteresis in the conductance similar than the observed to the isolated SCO NPs was observed. Although the mechanism for this behaviour was not clear, the authors suggested that the increase in the Fe–N distances reduces the tunnel barrier width, increasing the conductance between the electrodes.[107] However, this system showed high insulating character and low reproducibility. This strategy was improved organizing the nanoparticles in a 4 μm gap between the electrodes by dielectrophoresis, achieving better reproducibility, but difference in conductivity was still low.[108] In 2015, two different rod-like nanoparticles of 25 x 10 nm and 44 x 6 nm were contacted between gold electrodes substrates with a 50 nm gap. In this report, the electrical conductance increased in two orders of magnitude upon the spin transition (Figure 22a).[109]

SCO-Graphene hybrid materials have been also proposed due to the attractive properties offered by graphene, such as high electrical conductivity, studied transport mechanism and transparency. In 2016, $[Fe(trz)(Htrz)_2](BF_4)$ nanoparticles (110 x 50 nm) covered with a silica shell were placed between single-layer graphene electrodes. This hybrid device showed hysteresis in conductivity and possessed a higher conductance and robustness than the reports exposed previously.[110] The same year, the electrical properties of a similar device were also measured in a four-probe configuration as a function of temperature and gate voltage (Figure 22b). According to the calculations performed, the memory effect in the electrical properties were associated to the different dielectric constants of the SCO in the LS and HS states, affecting the charge-carrier-scattering mechanism in graphene.[111]

Single-walled carbon nanotubes (SWCNTs) and silver nanowires give the possibility of hosting SCO nanoparticles into their cavities while maintaining the electrical conductivity along their surface. This year (2021), $[Fe(H_2Bpz_2)_2(L)]$ (H_2Bpz_2 = dihydrobis(pyrazolyl) borate molecules were encapsulated inside 1D cavities of SWCNTs. The SCO–SWCNT interactions produced a shift to higher temperatures of $T_{1/2}(\uparrow)$ and $T_{1/2}(\downarrow)$ while maintaining its large hysteresis. Electrical measurements showed how the SCO triggers distinct large-conductance bistability through the SWCN

(Figure 22c).[112] In the case of SCO-silver nanocomposites, high conductivities were achieved with no memory effect. [113]

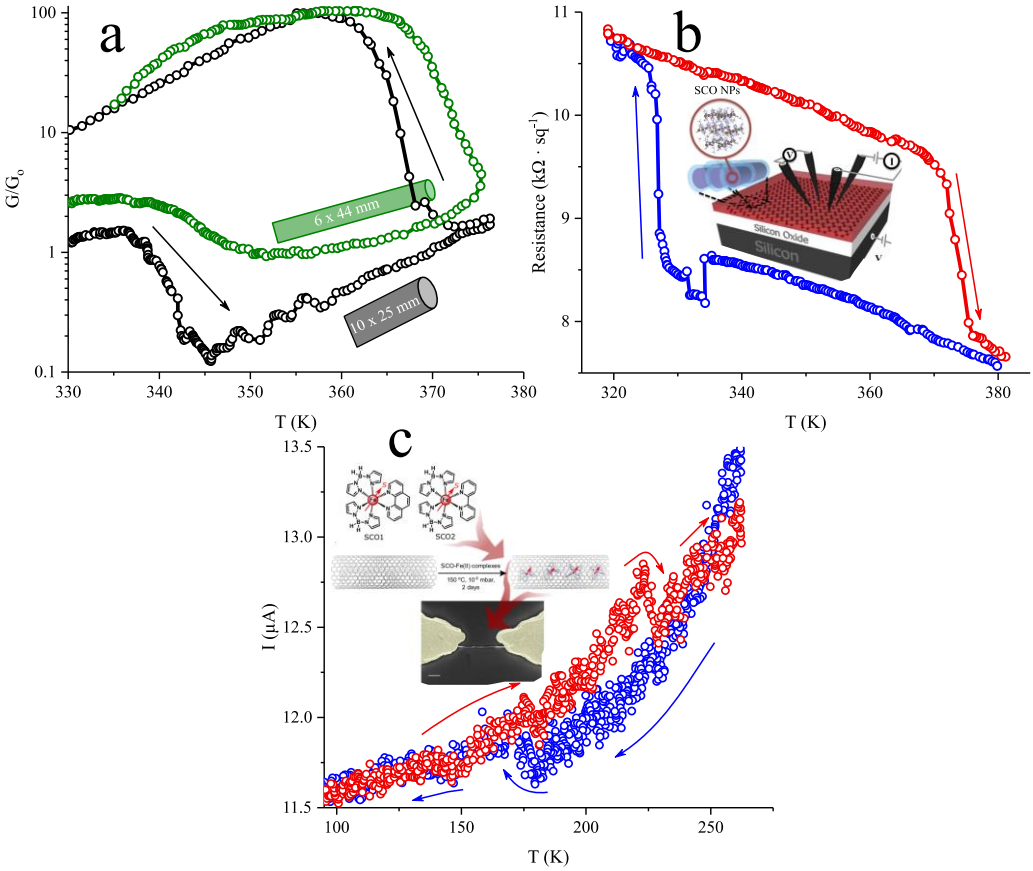

Figure 22. Electrical characterization of devices made with 25/100nm (color) and 44/6 nm (color) samples (a).[109] Temperature dependence of graphene electrical properties after the deposition of nanoparticles and schematic of the device with nanoparticles over CVD graphene on top of a Si/SiO_2 (b).[111] Current (*I*) measured at as a function of the temperature in a SCO@SWCNT (c).[112]

Other synthetic approaches to give conductive properties to SCO complexes were based on the functionalization of the ligand attached to the metallic centre with tetrathiafulvalene (TTF) or its derivates.[114] Figure 23a shows the resistivity vs *T* graph of $[Fe(dppTTF)_2][Ni(mnt)_2]_2(BF_4)\cdot PhCN$ (mnt = maleonitriledithiolate) crystals. These crystals showed higher conductivities than the previously analyzed systems ($2.6 \cdot 10^{-3}$

$S \cdot cm^{-1}$) and, more importantly, an anomaly in the range of temperature of the spin transition (160–280 K) with different activation energies below and above it.

Another approach in this direction was the co-crystallization of SCO with conductive organic radical anions. This approach offers more versatility than the previous mentioned since different building blocks can be chosen, allowing modular design of functional materials. Recently, Shatruk et al. used this strategy to co-crystallize a Fe(II) complex with fractionally charged 7,7,8,8–tetracyanoquinodimethane. As in the previous approach, an inflection point in the resistivity vs *T* plot was observed in the range of the LS→HS transition, leading to two regimes with distinct activation energies (Figure 23b).[115] However, none of these approaches have achieved SCO conductive complexes with hysteretic behaviour in the electrical properties.

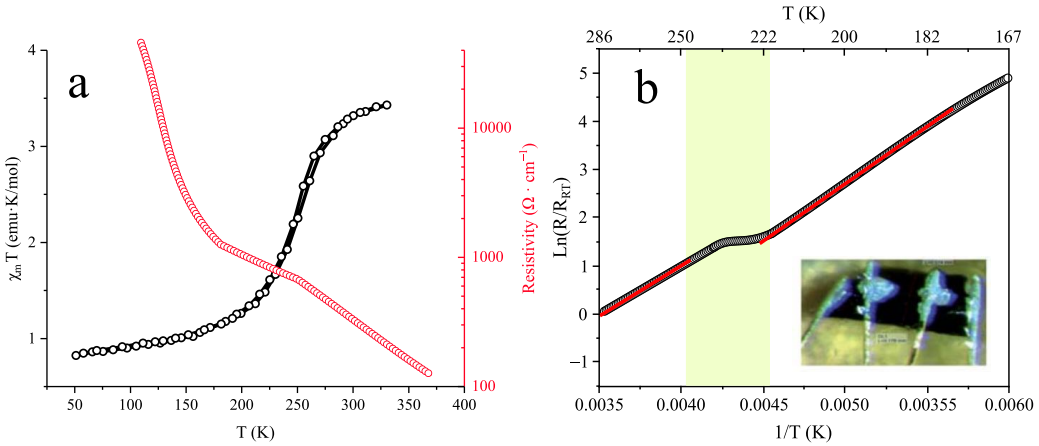

Figure 23. Temperature dependence of $\chi_m T$ values and resistivity in $[Fe(dppTTF)_2][Ni(mnt)_2]_2(BF_4)\cdot PhCN$ (mnt = maleonitriledithiolate) (a).[114] The temperature dependence of the log of normalized electrical resistance measured on single crystals of $[Fe(3\text{–}bpp)_2](TCNQ)_3$ (3–bpp = 2,6–bis(pyrazol–3–yl)pyridine, TCNQ = 7,7,8,8–tetracyanoquinodimethane) (b).[115]

In 2014, our group incorporated $[Fe(trz)(Htrz)_2](BF_4)$ and $[Fe(trz\text{–}NH_2)_3](SO_4)$ into polypyrrol (PPY), one of the most studied conducting polymers due to its high stability and conductivity, flexibility, low-cost, processability and the possibility of transparency in thin films.[116] As observed in Figure 24, memory effect was successfully maintained

over several reproducible cycles with differences in conductivity around 60% close to room temperature.[117]

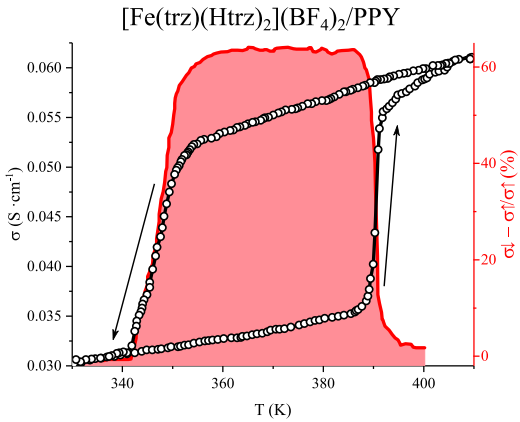

Figure 24. Conductivity (σ) measurements as a function of temperature for Fe(trz)(Htrz)$_2$](BF$_4$)/PPY. The difference in conductivity during a cooling ($\sigma\downarrow$) and heating ($\sigma\uparrow$) cycle for all the composites is represented with the red filled area.[117]

1.7. Thesis objective and outline

During this chapter, the importance of molecular magnetism has been presented and, within it, SCO as a remarkable example of true thermal bistability which properties have been studied and tuned by different research groups. Among all the wide range of different compounds, 1D chains present abrupt transitions with a remarkable hysteresis making them potential candidates for next generation hybrid devices. During this thesis, I will show the research I have developed during the last years at Galán-Mascarós group for the synthesis of novel SCO compounds showing abrupt transitions with hysteresis close to and at room temperature, the tuning of the magnetic properties of the previously studied SCO compounds and the implementation of SCO materials into electrical devices.

In the Chapter 2, the magnetic and structural properties of new SCO compound made with the 4–(1,2,4–triazol–4–yl)ethanedisulfonate (L) and 4NH$_2$–1,2,4–triazole (NH$_2$–trz) ligands will be studied.

Chapter 3 deals with the mechanosynthesis of new a cooperative SCO system, demonstrating that mechanosynthesis offers synthetic alternatives, allowing the obtention of materials that are not reachable via traditional solution-based methods

In chapter 4, the effect of mechanochemical recrystallization on the thermal hysteresis and structural properties will be studied in two 1D FeII–triazole SCO: $[Fe(trz)(Htrz)_2](BF_4)$ or $[Fe(trz–NH_2)_3](SO_4)$.

To conclude, in chapter 5 the mechanochemical processing of two highly conducting organic/inorganic composites exhibiting spin crossover-induced memory effect in their transport properties will be described. For this aim, $[Fe(trz)(Htrz)_2](BF_4)$ and $[Fe(trz–NH_2)_3](SO_4)$ will be mechanically processed with three different conductive polymer matrixes (PPY, PEDOT and PANI).

1.8. References

[1] O. Kahn, *Molecular Magnetism*, VCH publishers, **1993**.

[2] B. C. Guha, *Proc. R. Soc. Lond. A* **1952**, 206, 353.

[3] B. Bleaney, K. D. Bowers, *Proc. R. Soc. Lond. A* **1952**, 214, 451.

[4] M. B. Robin, *Inorg. Chem.* **1962**, 1, 337.

[5] T. Mallah, S. Thiébaut, M. Verdaguer, P. Veillet, *Science* **1993**, 262, 1554.

[6] S. M. Holmes, G. S. Girolami, *J. Am. Chem. Soc.* **1999**, 121, 5593.

[7] B. Sieklucka, D. Pinkowicz, *Molecular Magnetic Materials: Concepts and Applications*, Wiley-VCH, **2017**.

[8] L. Cambi, L. Szegö, *Ber. Dtsch. Chem. Ges.* **1933**, *66*, 656.

[9] L. E. Orgel, *Q. Rev. Chem. Soc.* **1957**, 4, 381.

[10] A. Caneschi, D. Gatteschi, R. Sessoli, *J. Am. Chem. Soc.* **1991**, 113, 5873.

[11] R. Sessoli, D. Gatteschi, A. Caneschi, M.A. Novak, *Nature* **1993** *365*, 141.

[12] R. Sessoli, H. L. Tsai, A. R. Schake, S. Wang, J. B. Vincent, K. Folting, D. Gatteschi, G. Christou, D. N. Hendrickson, *J. Am. Chem. Soc.* **1993**, 115, 1804.

[13] L. Thomas, F. Lionti, R. Ballou, D. Gatteschi, R. Sessoli, B. Barbara, *Nature* **1996**, 383, 145.

[14] J. R. Friedman, M. P. Sarachik, J. Tejada, J. Maciejewski, R. Ziolo, *J. Appl. Phys*. **1996**, 70, 6031.

[15] F.S. Guo, B.M. Day, Y.C. Chen, M.L. Tong, A. Mansikkamäki, R.A. Layfield, *Science* **2018**, *362*, 1400.

[16] P. Gütlich, Y. Garcia, H.A. Goodwin, *Chem. Soc. Rev*. **2000**, *29*, 419.

[17] F. Grandjean, G.J. Long, B.B. Hutchinson, L. Ohlhausen, P. Neill, J.D. Holcomb, *Inorg. Chem.* **1989**, *28*, 4406.

[18] S. Scheuermayer, F. Tuna, M. Bodensteiner, M. Scheer, R.A. Layfield, *Chem. Commun.* **2012**, *48*, 8087.

[19] D.M. Halepoto, D.G. Holt, L.F. Larkworthy, D.C. Povey, G.W. Smith, G.J. Leigh, *Polyhedron* **1989**, *8*, 1821.

[20] S. Hayami, K. Murata, D. Urakami, Y. Kojima, M. Akita, K. Inoue, *Chem. Comm.* **2008**, 48, 6510.

[21] H. R. Chang, J. K. McCusker, H. Toftlund, S. R. Wilson, A. X. Trautwein, H. Winkler, D. N. Hendrickson, *J. Am. Ceram. Soc*. **1990**, 112, 6814.

[22] E. König, G. Ritter, *Solid State Commun.* **1976**, 18, 279.

[23] E. König, G. Ritter, S. K. Kulshreshtha, S. M. Nelson, *Inorg. Chem.* **1982**, 21, 3022.

[24] J. J. McGravey, I. Lawthers, J. Chem. Soc., *Chem. Commun.* 1982, 16, 906.

[25] S. Decurtins, P. Gütlich, C.P. Köhler, H. Spiering, A. Hauser, *Chem. Phys. Lett.* **1984**, *105*, 1.

[26] A. Hauser, *Chem. Phys. Lett.* **1986**, *124*, 543.

[27] J.F. Létard, P. Guionneau, L. Goux-Capes, *Spin Crossover in Transition Metal Compounds III*, Springer, **2006**.

[28] P. Gütlich, H.A. Goodwin, *Spin Crossover in Transition Metal Compounds I*, springer, **2004**.

[29] T. M. Dunn, D. S. McClure, R. G. Pearson, *Some Aspects of Crystal Field Theory*, New York, Harper & Row, **1965**.

[30] R. Tsuchida, *Bull. Chem. Soc. Jpn.* **1938** *13*, 436.

[31] L. Catala, F. Volatron, D. Brinzei, T. Mallah, *Inorg. Chem*. **2009**, 48, 3360.

[32] A. Hauser, *Adv. Polym. Sci.* **2004**, 233, 49.

[33] Y. Tanabe, S. Sugano, *J. Phys. Soc. Jpn.* **1954**, 9, 766.

[34] J.M.D. Coey, *Magnetism and Magnetic Materials*, Cambridge University Press, **2010**.

[35] D. F. Evans, *J. Am. Chem. Soc*. **1959**, 2003-2005.

[36] W. Nicolazi, A. Bousseksou, *C. R. Chimie* **2018**, 21, 1060.

[37] N. Paradis, G. Chastanet, J. F. Létard, Eur. J. Inorg. Chem. 2012, 3618.

[38] G. Chastanet, C. Desplanches, C, Baldé, P. Rosa, M. Marchivie, P. Guionneau, *Chem. Sq*. **2018**, 2.

[39] G. Chastanet, M. Lorenc, R. Bertoni, C. Desplanches, *C. R. Chimie* **2018**, 21, 1075.

[40] D. Qiu, L. Gu, X.L. Sun, D.H. Ren, Z. Gu, Z. Li, *RSC adv.* **2014**, 4, 61313.

[41] A. Marino, P. Chakraborty, M. Servol, M. Lorenc, E. Collet, A. Hauser, *Angew. Chemie - Int. Ed.* **2014**, 53, 3863.

[42] A. Hauser, *J. Chem. Phys.* **1991**, 94, 2741.

[43] R. W. Hogue, S. Singh, S. Brooker, *Chem. Soc. Rev.* **2018**, 47, 7303.

[44] J.R. Galán-Mascarós, G. Aromí, M. Darawsheh, *C. R. Chim.* **2018**, 21, 1209.

[45] C. Janiak, *J. Chem. Soc., Chem. Commun.* **1994**, 545.

[46] A. F. Stassen, M. De Vos, P. J. Van Koningsbruggen, F. Renz, J. Ensling, H. Kooijman, A. L. Spek, J. G. Haasnoot, P. Gütlich, J. Reedijk, *Eur. J. Inorg. Chem.* **2000**, 2231.

[47] L.H. Sugiyarto, D. C.Craig, A. D. Rae, H. A. Goodwin, *Aust. J. Chem.* **1993**, 46, 1269.

[48] J. Saroja, V. Manivannan, P. Chakraborty, S. Pal, *Inorg. Chem.* **1995**, 34, 3099.

[49] M. H. Klingele, B. Moubaraki, J. D. Cashion, K. S. Murray, S. Brooker, *Chem. Comm.* **2005**, 987.

[50] C. J. Schneider, J. D. Cashion, B. Moubaraki, S. M. Neville, S. R. Batten, D. R. Turner, K. S. Murray, *Polyhedron* **2007**, 26, 1764.

[51] Y. Garcoa, F. Robert, A. D. Naik, G. Zhou, B. Tinant, K. Robeyns, S. Michotte, L. Piraux, *J. Am. Chem. Soc.* **2011**, 133, 15850.

[52] G. Vos, R. A. Le Febre, R. A. De Graaff, J. G. Haasnoot, J. Reedijk, *J. Am. Chem. Soc.* **1983**, 105, 1682.

[53] V. Gómez, J. Benet-Buchholz, E. Martin, J.R. Galán-Mascarós, *Chem. Eur. J.* **2014**, 20, 5369.

[54] Y. Garcia, P. J. Van Koningsbruggen, G. Bravic, D. Chasseau, O. Kahn, *Eur. J. Inorg. Chem.* **2003**, 2003, 356.

[55] K. Drabent, Z. Ciunik, *Chem. Commun.* **2001**, 1254.

[56] A. Urakawa, W. Van Beek, M. Monrabal-Capilla, J. R. Galán-Mascarós, L. Palin, M. Milanesio, *J. Phys. Chem. C **2011**, 115, 1323.*

[57] A. Michalowicz, J. Moscovici, B. Ducourant, D. Cracco, O. Kahn, *Chem. Mater*. **1995**, 7, 1833.

[58] A. Grosjean, N. Daro, B. Kauffmann, A. Kaiba, J.F. Létard, P. Guionneau, *Chem. Comm.* **2011**, 47, 12382.

[59] N. Pittala, F. Thétiot, C. Charles, S. Triki, K. Boukheddaden, G. Chastanet, M. Marchivie, *Chem. Comm.* **2017**, 53, 8356.

[60] V. Y. Sirenko, O. I. Kucheriv, A. Rotaru, I. O. Fritsky, I. Gural'skiy, *Eur. J. Inorg. Chem.* **2020**, 2, 4523.

[61] A. Grosjean, P. Négrier, P. Bordet, C. Etrillard, D. Mondieig, S. Pechev, E. Lebraud, J. F. Létard, P. Guionneau, *Eur. J. Inorg. Chem.* **2013**, 2013, 796.

[62] W. Vreugdenhil, J. H. V. Diemen, R. A. G. De Graaff, J. G. Haasnoot, J. Reedijk, A. M. Van Der Kraanm O. Kahn, J. Zarembowitch, *Polyhedron* **1990**, 9, 2971.

[63] E. Milin, V. Patinec, S. Triki, E. Bendeif, S. Pillet, M. Marchivie, G. Chastanet, K. Boukheddaden, *Inorg. Chem.* **2016**, 55, 11652.

[64] Y. Garcia, O. Kahn, L. Rabardel, B. Chansou, L. Salmon, J. P. Tuchagues, *Inorg. Chem*. **1999**, 38, 4663.

[65] K. S. Kumar, M. Ruben, *Coord. Chem. Rev.* **2017**, 346, 176.

[66] W. Liu, X. Bao, L. Mao, J. Tucek, R. Zboril, J. Liu, F. Guo, Z. Ni, M. Tong, *Chem. Commun*. **2014**, 50, 4059.

[67] O. Roubeau, *Chem. Eur. J*. **2012**, 18 15230.

[68] J. H. Askew, H. J. Shepherd, *Chem. Comm*. **2018**, 54, 180.

[69] E. Coronado, J. R. Galán-Mascarós, M. Monrabal-Capilla, J. García-Martínez, P. Pardo-ibáñez, *Adv. Mater*. **2007**, 19, 1359.

[70] M. Giménez-Marqués, M. L. G. S. de Larrea, E. Coronado, *J. Mater. Chem. C* **2015**, 3, 7946.

[71] J. R. Galán-Mascarós, E. Coronado, A. Forment-Aliaga, M. Monrabal-Capilla, E. Pinilla-Cienfuegos, M. Ceolin, *Inorg, Chem.* **2010**, 49, 5706.

[72] Y. Raza, F. Volatron, S. Moldovan, O. Ersen, V. Huc, C. Martini, F. Brisset, A. Gloter, O. Stéphan, A. Bousseksou, L. Catala, T. Mallah, *Chem. Comm.* **2011**, 47, 11501.

[73] O. Roubeau, J. M. A. Gómez, E. Balskus, J. J. A. Kolnaar, , J. G. Haasnoot, J. Reedijk, *New J. Chem.* **2001**, 25, 144.

[74] J. Krober, E. Codjovi, O. Kahn, F. Groliere, C. Jay, *J. Am. Chem. Soc*. **1993**, 115, 9810.

[75] O. Kahn, C. J. Martinez, *Science* **1998**, 279, 44.

[76] J. P. Martin, J. Zarembowitch, A Dworkin, J. G. Haasnoot, E. Codjovi, *Inorg. Chem.* **1994**, 33, 2617

[77] N.F. Sciortino, S. M. Neville, C. Desplanches, J. F. Létard, V. Martinez, J. A. Real, B. Moubaraki, K. S. Murray, C. J. Kepert, *Chem. Eur. J.* **2014**, 20, 7448.

[78] M. S. Sylla, C. Baldé, N. Daro, C. Desplanches, M. Marchivie, G. Chastanet, *Eur. J. Inorg. Chem.* **2018**, 2018, 297.

[79] C. Baldé, M. S. Sylla, C. Desplanches, G. Chastanet, *Polyhedron* **2019**, 159, 84.

[80] C. Lefter, S. Tricard, H. Peng, G. Molnár, L. Salmon, P. Demont, A. Rotaru, A. Bousseksou, *J. Phys. Chem. C* **2015**, 119, 8522.

[81] A. Enríquez-Cabrera, K. Ridier, L. Salmon, L. Routaboul, A. Bousseksou, *Eur. J. Inorg. Chem.* **2021**, 2000.

[82] C. F. Wang, G. Y. Yang, Z. S. Yao, J. Tao, *Chem. Eur. J.* **2018**, 24, 3218.

[83] C. F. Wang, R. F. Li, X. Y. Chen, R. J. Wei, L. S. Zheng, J. Tao, *Angew. Chem.* **2015**, 127, 1594.

[84] A. Enríquez-Cabrera, L. Routaboul, L. Salmon, A. Bousseksou, *Dalton Trans.* **2019**, 48, 16853.

[85] J. H. Askew, H. J. Shepherd, *Dalton Trans.* **2020**, 49, 2966.

[86] M. Sorai, R. Burriel, E. F. Westrum Jr., D. N. Hendrickson, *J. Phys. Chem. B* **2008**, 112, 4344.

[87] M. D. Timken, S. R. Wilson, D. N. Hendrickson, *Inorg. Chem.* **1985**, 24, 3450.

[88] M.S. Haddad, W. D. Federer, M. W. Lynch, D. N. Hendrickson, *J. Am. Chem. Soc.* **1980**, 102, 1468.

[89] M. S. Haddad, W. D. Federer, M. W. Lynch, D. N. Hendrickson, *Inorg. Chem.* **1981**, 20, 131.

[90] R. Torres-Cavanillas, R. Sanchis-Gual, J. Dugay, M. Coronado-Puchau, M. Giménez-Marqués, E. Coronado, *Adv. Mater.* **2019**, 31, 1900039.

[91] H. J. Shepherd, I. A. Gural'Skiy, C. M. Quintero, S. Tricard, L. Salmon, G. Molnár, A. Bousseksou, *Nat. Commun.* **2013**, 4, 1.

[92] S. Rat, M. Piedrahita-Bello, L. Salmon, G. Molnár, P. Demont, A. Bousseksou, *Adv. Mater.* **2018**, 1705275, 1.

[93] M. D. Manrique-Juárez, S. Rat, L. Salmon, G. Molnár, C. M. Quintero, L. Nicu, H. J. Shepherd, A. Bousseksou, *Coord. Chem. Rev.* **2016**, 308, 395.

[94] M. D. Manrique-Juárez, F. Mathieu, A. Laborde, S. Rat, V. Shalabaeva, P. Demont, O. Thomas, L. Salmon, T. Leichle, L. Nicu, G. Molnár, A. Bousseksou, *Adv. Funct. Mater.* **2018**, 28, 1801970.

[95] M. D. Manrique-Juárez, F. Mathieu, A. Laborde, S. Rat, V. Shalabaeva, P. Demont, O. Thomas, L. Salmon, T. Leichle, L. Nicu, G. Molnár, A. Bousseksou, *Adv. Funct. Mater.* **2018**, 28, 1801970.

[96] O. Kahn, J, Kröber, C. Jay, *Adv. Mater*. **1992**, 4, 718.

[97] J. L. Wang, Q. Liu, Y. S. Meng, X. Liu, H. Zheng, Q. Shi, C. Y. Duan, T. Liu, *Chem. Sci.* **2018**, 9, 2892.

[98] C. F. Wang, R. F. Li, X. Y. Chen, T. J. Wei, L. S. Zheng, J. Tao, *Angew. Chem.* **2015**, 54, 1574.

[99] I. Suleimanov, O. Kraieva, J. S. Costa, I. O. Fritsky, G. Molnár, L. Salmon, A. Bousseksou, *J. Mater. Chem. C* **2015**, 3, 5026.

[100] S. Titos-Padilla, J. M. Herrera, X. W. Chen, J. J. Delgado, E. Colacio, *Angew. Chem.* **2011**, 50, 3290.

[101] O. Kraieva, I. Suleimanov, G. Molnár, L. Salmon, *Magnetochemistry* **2016**, 2, 11.

[102] L. Salmon, G. Molnár, D. Zitouni, C. Quintero, C. Bergaud, J. C. Micheau, A. Bousseksou, *J. Mater. Chem.* **2010**, 20, 5499.

[103] F. Bigdeli, C. T. Lollar, A. Morsali, H. C. Zhou, *Angew. Chem.* **2020**, 59, 4652.

[104] M. Ohba, K. Yoneda, G. Agusti, M. C. Muñoz, A. B. Gaspar, J. A. Real, M. Yamasaki, H. Ando, Y. Nakao, S. Sakaki, S. Kitagawa, *Angew. Chem. - Int. Ed.* **2009**, 48, 4767.

[105] C. Lefter, I. A. Gural'skiy, H. Peng, G. Molnár, L. Salmon, A. Rotaru, A. Bousseksou, P. Demont, *Phys. Status Solidi - Rapid Res. Lett*. **2014**, 8, 191.

[106] I. Soroceanu, A. Graur, E. Coca, L. Salmon, G. Molnar, P. Demont, A. Bousseksou, A. Rotaru, *J. Phys. Chem. Lett.* **2019**, 10, 7391.

[107] F. Prins, M. Monrabal-Capilla, E. A. Osorio, E. Coronado, H. S. J. Van Der Zant, *Adv. Mater*. **2011**, 23, 1545.

[108] A. Rotaru, J. Dugay, R. P. Tan, I. A. Guralskiy, L. Salmon, P. Demont, J. Carrey, G. Molnár, M. Respaud, A. Bousseksou, *Adv. Mater.* **2013**, 25, 1745.

[109] J. Dugay, M. Giménez-Marqués, T. Kozlova, H. W. Zandbergen, E. Coronado, H. S. J. Van Der Zant, *Adv. Mater.* **2015**, 27, 1288.

[110] A. Holovchenko, J. Dugay, M. Giménez-Marqués, R. Torres-Cavanillas, E. Coronado, H. S. J. van der Zant, *Adv. Mater.* **2016**, 28, 7228.

[111] J. Dugay, M. Aarts, M. Gimenez-Marqués, T. Kozlova, H. W. Zandbergen, E. Coronado, H. S. J. Van Der Zant, *Nano Lett.* **2017**, 17, 186.

[112] J. Villalva, A. Develioglu, N. Montenegro-Pohlhammer, R. Sánchez-de-Armas, A. Gamonal, E. Rial, M. García-Hernández, L. Ruiz-Gonzalez, J. S. Costa, C. J. Calzado, E. M. Pérez, E. Burzurí, *Nat. Commun.* **2021**, 12, 1.

[113] Z. H. Li, Y. X. Wang, W. K. Han, W. Zhu, T. Li, Z. Li, X. Ren, Z. G. Gu, *New J. Chem.* **2017**, 41, 10062.

[114] M. Nihei, N. Takahashi, H. Nishikawa, H. Oshio, *Dalt. Trans.* 2011, 40, 2154.

[115] Ö. Üngör, E. S. Choi, M. Shatruk, *Chem. Sci.* **2021**, 12, 10765.

[116] G. Prunet, F. Pawula, G. Fleury, E. Cloutet, A. J. Robinson, G. Hadziioannou, A. Pakdel, *Mater. Today Phys.* **2021**, 18, 100402.

[117] Y. S. Koo, J. R. Galán-Mascarós, *Adv. Mater.* **2014**, 26, 6785.

Chapter 2. Mixed-Ligand Triazole-Based SCO Chains: Tuning Temperature and Thermal Hysteresis

Abstract

Two triazole-based ligand, 4–(1,2,4–triazol–4–yl)ethanedisulfonate (L) and 4NH_2–1,2,4–triazole (NH_2–trz), were mixed with different proportions with the $Fe(ClO_4)_2$ salt, leading to the formation of a new SCO compound with formula $[Fe(L)(NH_2–trz)_2]$. The magnetic and structure properties of this new compound were completely different than those from the pure $[(Fe_3(L)_6(H_2O)_6](Me_2NH_2)_6$ and $[Fe(NH_2–trz)_3]_n(ClO_4)_n$, as confirmed by several techniques, including PXRD, XAFS, IR, SQUID and DSC. The different NH_2–trz:L ratios (80:20, 60:40, 50:50 and 40:60) did not produce large modifications in the structure and composition of $[Fe(L)(NH_2–trz)_2]$. This new compound showed abrupt spin transitions, accompanied by a wide hysteresis at room temperature and displayed temperature-induced excited spin-state trapping (TIESST) phenomenon with a characteristic temperature of 240 K.

Introduction

The production of novel SCO polynuclear complexes has remained a very prolific activity during the last few years. New ligand structures and synthetic and post-synthetic strategies have been developed in order to obtain SCO complexes with bistability close to room temperature. Among all the SCO materials, one of the most studied in the last decades is the 1D SCO coordination polymer $[Fe(Htrz)_2(trz)]_n$ (Htrz = 4H–1,2,4–triazole and trz = 1,2,4–triazolate) due to its large hysteresis (≈ 40 K) that is maintained up to 4 nm nanoparticles.[1] These kind of polymeric complexes offer the possibility of tuning the magnetic properties (hysteresis and transition temperatures) upon slight modifications via ligand or cation exchange or processing protocols, maintaining the paternal polymeric structure. Different approaches have been developed to downshift the transition temperatures of this compound, such as size-control techniques,[2,3] hydrostatic pressure,[4,5] chemical pressure,[6] exfoliation,[7] or modifications of the synthetic procedure.[8] Regarding the latter case, Kahn et al. observed that doping $[Fe(Htrz)_3]_n(ClO_4)_{2n}$ complex with the 4NH_2–1,2,4–triazole (NH_2–trz) ligand resulted in a SCO alloy with $[Fe(Htrz)_{3x}(NH_2–trz)_{3–3x}]_n(ClO_4)_{2n}$ formula. Depending on the ratio

between the ligands the transition temperatures could be tuned and, in the case of $[Fe(Htrz)_{0.85}(NH_2{-}trz)_{0.15}]_n(ClO_4)_{2n}{\cdot}nH_2O$, bistability was achieved at room temperature, with transitions of $T_{1/2}(\uparrow)$ = 304 K and $T_{1/2}(\downarrow)$ = 288 K.[8] This trend was extended to nanoparticles of the same alloy and of $[Fe(Htrz)_{3-3x}(NH_2{-}trz)_{3x}]_n(BF_4)_{2n}$, observing in both cases abrupt transitions with hysteresis above room temperature, that was retained in the nanoparticles up to 11 nm.[1,9] Although, the simplicity and effectiveness of this method, there are few reports that study the ligand substitution effect in the structural and magnetic properties. In 2014, a similar study was performed for the 1D $[Fe(btzx)_{3-3x}(btix)_{3x}]_n(ClO_4)_{2n}$, where btzx = 1,4–bis(tetrazol–1–ylmethyl)benzene and btix = 1,4–bis(triazol–1–ylmethyl)benzene. The SCO alloys showed a different spin transition than the obtained for x = 0 and x = 1, which was attributed to the different chemical environment of the iron centres.[10] Recently, alloys of the mononuclear $[Fe(Mebpp)_{2-2x}(Me2bpp)_{2x}](ClO_4)_2$ (Mebpp and Me2bpp = methyl– and bis–methyl–substituted bis–pyrazolylpyridine ligands, respectively) compound, could be synthesized with a maximum substitution of x = 0.5. The gradual doping produced an increase in the transition temperatures.[11] However, all these studies involve the mixture of ligands with the same charge and that individually promote the formation of SCO complexes with the same dimension.

In this chapter, we study the use of the 4–(1,2,4–triazol–4–yl)ethanedisulfonate ligand (L) as cationic dopant in the 1D SCO $[Fe(NH_2{-}trz)_3]_n(ClO_4)_{2n}$. The ligand L, in solution with perchlorate iron salts, leads to the formation of a trinuclear compound that exhibits SCO behaviour with one of the widest hysteresis above room temperature in comparison with common discrete SCO polynuclear complexes.[12] In contrast, the 1D polymeric $[Fe(NH_2{-}trz)_3]_n(ClO_4)_{2n}$, obtained by mixing NH_2–trz and $Fe(ClO_4)_2$, exhibits a very narrow and abrupt hysteresis loop at very low temperatures (250 K). [13,14]

Experimental section

Note! Perchlorate compounds are very explosive under mechanical stress. The amino radicals in the structure produce instability, leading to bigger explosions.[15,16]

$[Fe(NH_2–trz)_3]_n(ClO_4)_n$ (**1**). 0.2 g of $(FeClO_4)_2$ (0.8 mmol) and 0.2 g of 4–Amino–4H–1,2,4–triazole (NH_2–trz) (2.4 mmol) were dissolved in 10 mL Milli–Q water with a small amount of ascorbic acid to avoid the oxidation of Fe(II). A white solid precipitated quickly appeared and the solution was stirred for 2 hours. The precipitated was centrifuged and washed with ethanol and diethyl ether and dried under vacuum.

$[Fe_3(L)_6(H_2O)_6](Me_2NH_2)_6$ (**2**, L = 4–(1,2,4–triazol–4–yl)ethanedisulfonate). The ligand L was obtained as the dimethlammonium salt $(Me_2NH_2)_2L$ following the literature procedure.[12] 0.1 g of $Fe(ClO_4)_2 \cdot 6H_2O$ (0.3 mmol) was dissolved in 2.5 mL of Milli–Q water with a small amount of ascorbic acid. 0.3 g of $(Me_2NH_2)_2L$ (0.9 mmol) were dissolved in 2.5 mL of Milli–Q water. Both solutions were mixed together and stirred during 30 min. The addition of ethanol led to the precipitation of a pink solid that was centrifuged and washed with ethanol and diethyl ether and dried under vacuum.

$[Fe(L)(NH_2–trz)_2]$ alloys (3A–3D). Different amounts of NH_2–trz and L (NH_2–trz:L = 80:20, 60:40, 50:50, 40:60, 20:80; total molar weight = 2.4 mmol; Table 1) were mixed in 10 mL of Milli–Q water with a small amount of ascorbic acid. 0.2 g of $(FeClO_4)_2$ (0.8 mmol) were added to the previous solution. For all the NH_2–trz:L ratios except to the 20:80 a fast precipitation of a pink solid occurred. After 2 hours of stirring, all the solids were centrifuged and washed with ethanol and diethyl ether and dried under vacuum. In the case of 20:80 (NH_2–trz:L) ratio, ethanol was added to promote the precipitation of a pink solid which was centrifuged, washed and dried under vacuum.

As perchlorate salts of metal ion complexes like **1** are potential explosives under mechanical impact and the some of the analysis involves pressure application, we tested the explosiveness of **1**, **3A**, **3B**, **3C** and **3D** via hammer impact. A strong hammer impact on **1** produced a percussive noise, concluding that this compound is highly sensitive to mechanical stress. In the case of **3A**, **3B**, **3C** and **3D**, the impact did not produce any noise. To completely check the non-explosiveness of **3** compounds we applied pressures up to 0,4 GPa for 5 minutes, producing no physical changes in the samples. With these

tests, we conclude that the **3** compounds are not explosive under standard pressure conditions.

Table 1. label of **3** compounds and explosiveness test.

NH_2–trz:L Ratio	Label	Precipitation	Explosive
100:0	**1**	White	Yes
80:20	**3A**	Pink	No
60:40	**3B**	Pink	No
50:50	**3C**	Pink	No
40:60	**3D**	Pink	No
20:80	--	No	--

See Annex I for the physical methods used in this chapter: Inductively coupled plasma mass spectrometry (ICP-MS), Elemental analysis, Thermogravimetric analysis (TGA), Differential scanning calorimetry (DSC), Infrared spectroscopy (IR), Energy dispersive X-ray (EDX) / Field Emission scanning electron microscopy (FESEM), Single crystal X-ray diffraction (SCXRD), Powder X-ray diffraction (PXRD), Extended X-ray absorption fine structure (EXAFS), Magnetic susceptibility measurements (SQUID).

Results and discussion

Four powders have been obtained by direct synthesis in aqueous solution using four different NH_2–trz:L (L = 4–(1,2,4–triazol–4–yl)ethanedisulfonate; NH_2–trz = 4NH_2–1,2,4–triazole) ratios (**3A**: 80:20; **3B**: 60:40, **3C**: 50:50 and **3D**: 40:60). The fast precipitation of the salts difficulted the isolation of crystals. For this reason, other techniques were used to determine the structure of these new compounds and its magnetic behaviour.

Stoichiometry

Inductively coupled plasma mass spectrometry (ICP–MS), elemental analysis and Energy dispersive X-ray Analysis (EDX) were carried out for all the alloys to identify the most probable stoichiometry. As observed in Table 2, the four alloys showed very

similar values for C, N, H and S, suggesting that the NH_2–trz:L ratio is the same one independently than the ratio used during the synthesis.

Table 2. ICP–MS and elemental analysis of **3A**, **3B**, **3C** and **3D**.

Sample	N	C	H	S	Fe
3A	11.74	8.76	16.97	2.17	1
3B	10.56	8.12	16.04	2.13	1
3C	9.91	7.89	16.76	2.08	1
3D	9.59	7.73	15.97	2.10	1

The 2:1 ratio between S and Fe, also supported by EDX analysis (Figure S2.1 and Table S2.1), suggested that there is one L ligand per Fe(II) atom. With these results, we supposed that the most probable stoichiometry of this new compound is $[Fe(L)(NH_2–trz)_2]$ (M_w = 478 g/mol), where the irons are linked to two NH_2–trz and to one 4–(1,2,4–triazol–4–yl)ethanedisulfonate. In addition, given the low solubility of all the compounds and the absence of cations (chlorine was not found by EDX), the most plausible hypothesis is that we have obtained a neutral polymeric chain (Figure 1).

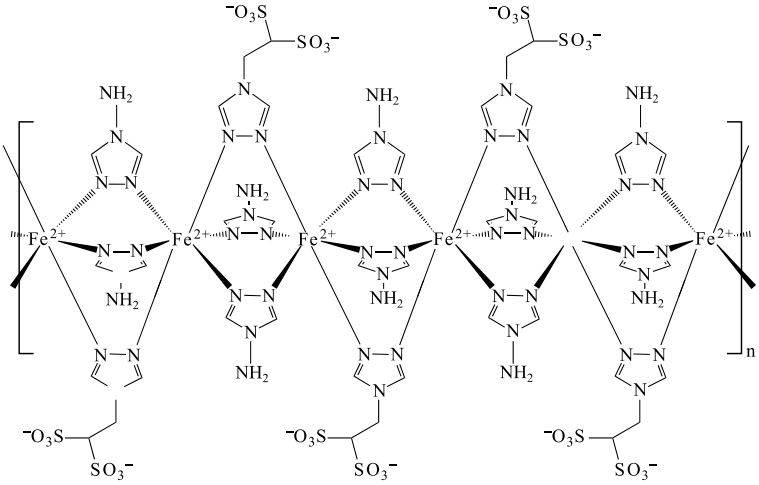

Figure 1. Scheme of general expected structure of **3**.

TGA analysis was also performed to **3** samples to determine the amount of water molecules in the structure. As observed in Figure S2.2 and Table S2.2, the structure was

hydrated with four water molecules in all the cases. As a result, we assumed that this new compound has a molecular formula of $[Fe(L)(NH_2–trz)_2]\cdot 4H_2O$ with a molecular weight of M_w = 542 g/mol.

Morphology

Field emission scanning electron microscopy (FESEM) was carried out for **3** samples in order to obtain more details about the differences between this set of samples. As observed in Figure 2 and Figure S2.3, all the samples were made of agglomerated needles that form hollow spheres. In samples **3A**, **3B** and **3C** we were able to find complete and incomplete spheres. Instead, in sample with a 40:60 NH_2–trz:L ratio (**3D**) we observed exclusively complete spheres. Notably, as observed in samples **3C** and **3D**, the size of the needles decreased for ratios far from the ideal 66:33 NH_2–trz:L, being hard to distinguish the shape in the extreme 40:60 ratio.

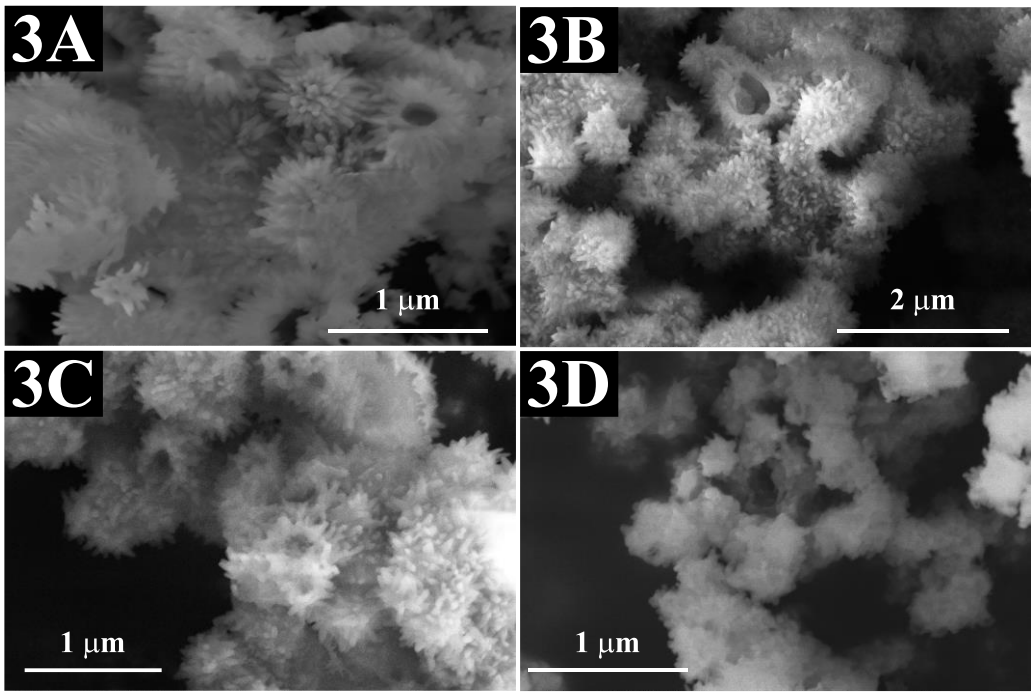

Figure 2. FESEM images of **3A**, **3B**, **3C** and **3D**.

Structural analysis

X-ray diffraction

Powder X-ray diffractograms (PXRD) in the 5–40º *2θ* range were obtained for **3A**, **3B**, **3C** and **3D** (Figure S2.4). All these samples showed PXRD patterns that perfectly overlapped. However, the PXRD diffractogram for samples **3C** and **3D** presented higher noise and lower crystallinity. This difference in crystallinity could be related with the loss of the shape and crystallite preferential domains when using high amounts of L in the NH_2–trz:L ratio, as previously observed in FESEM images.

Compound **3A**, as the most crystalline structure obtained, will be used for the rest of the analysis. Due to the fast precipitation of **1** and **3** compounds, we were not able to grow crystals to determine the atomic arrangement by single crystal X-ray diffraction (SCXRD). The diffraction patterns of $[Fe(NH_2–trz)_3]_n(ClO_4)_n$ (**1**), the Fe (II) trimer $[Fe_3(L)_6(H_2O)_6]$ $(Me_2NH_2)_6$ (**2**) and **3A** are shown in Figure 3, top. In the case of **1**, it has been well stablished its polymeric structure by different studies using other counteranions. In particular, crystals of $[Fe(NH_2–trz)_3]_n(NO_3)_{2n}$ could be obtained by slow diffusion method and its polymeric structure in a triclinic space group $P\bar{1}$ was determined.[17] Recently, Sirenko et al. obtained powders of $[Fe(NH_2–trz)_3]_n(SO_4)_n$ with a high degree of crystallinity, suitable for Rietveld refinement, concluding that, with this counteranion, the polymer crystallizes in a hexagonal $P6_3/m$ space group.[17]

Single crystals of compound **2** were isolated by layering the reaction mixture with ethanol. The SCXRD pattern revealed a trinuclear polyanionic structure formed by a linear array of octahedral Fe(II) ions connected by two triple μ–triazole bridges. The terminal iron positions complete its N_3O_3 hexacoordination with three H_2O molecules in *fac* conformation (Figure S2.5).[12] On the other hand, the diffraction patterns of **3** with different NH_2–trz:L ratios revealed a completely different structure than **1** and **2**.

Unfortunately, the lack of diffraction peaks humpers the resolution of the unit cell of this compound via Rietveld refinement.

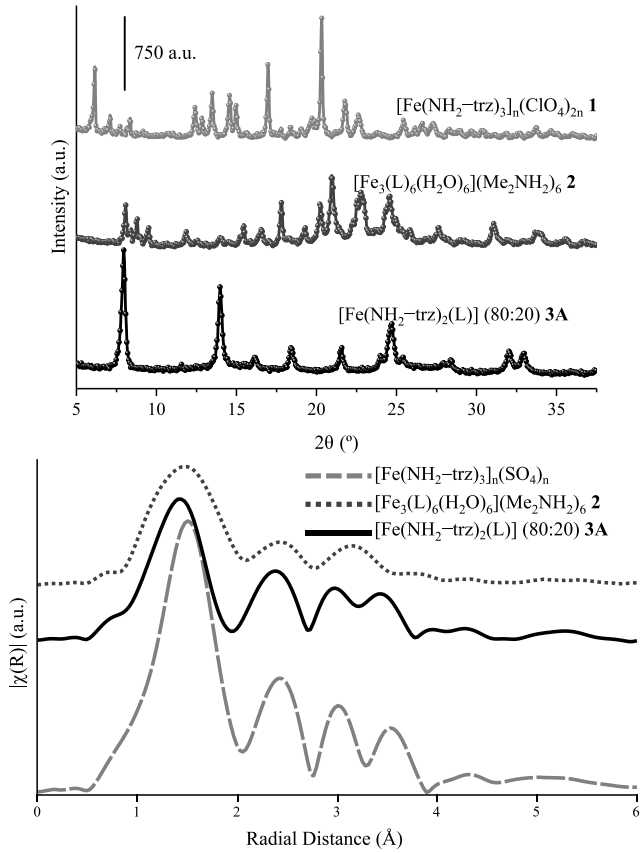

Figure 3. PXRD pattern of **1**, **3** and **3A** (top) and XAFS analysis of $[Fe(NH_2–trz)_3]_n(SO_4)_n$, **2** and **3A** (bottom).

For this reason, X-ray absorption fine structure (XAFS) was performed at ALBA Synchrotron, Beamline 22–CLÆSS (Figure 3, bottom). As the analysis in this beamline requires the use of pressed-made pellets, compound **1** was discard due to its sensitive explosiveness and substituted by the well characterized $[Fe(NH_2–trz)_3]_n(SO_4)_n$ compound (See supporting information for synthesis and Figure S2.6 for characterization).[15,18] EXAFS measurements of the trimer (**2**) showed only three broad peaks at 1.47, 2.43 and 3.20 Å. In contrast, the polymer chain $[Fe(NH_2–trz)_3]_n(SO_4)_n$ showed four well defined peaks in the same range of distances (1.52, 2.41, 3,02 and 3,57 Å) and less intense peaks at higher distances (4.22 and 5,41 Å). In the case of **3A**, it also

showed four peaks (1.42, 2.37, 2,96 and 3,42 Å) and some less intense peaks at higher distances, suggesting that **3A** has a polymeric structure more similar to the polymer $[Fe(NH_2–trz)_3]_n(SO_4)_n$ than to the trimer **2**.

Infrared Spectroscopy

Infrarred (IR) spectroscopy has been used to identify the structural features of 1,2,4–triazole/triazolate-based transition metal complexes.[19,20] As observed in Figure S2.7, **1** and **2** showed a similar IR spectra than its respective isolated ligand with additional metal–ligand vibrational signals. The IR spectra of **1**, **2** and **3A** in the 400–1700 cm^{-1} wavenumber range is represented in Figure 4. The full spectrum (400–4000 cm^{-1}) are included in Figure S2.7 in which the signals observed at 3000–3500 cm^{-1} were assigned to N–H and C–H stretching from the ligands. In the 850–1700 cm^{-1} range, the signals are attributed to vibrations of the triazole ligands (C=C, C=N, –N=N, etc.). It is completely clear that **1** and **2** are made of different ligands. However, **3A** shows similarities with both spectra. The signals observed at 598, 626 and 650 cm^{-1} in **3A**, attributed to the ring torsion vibrations, suggest that the structure of **3A** contains both ligands, as they overlap to 590 and 636 cm^{-1} from **2** and to 616 cm^{-1} from **1**.

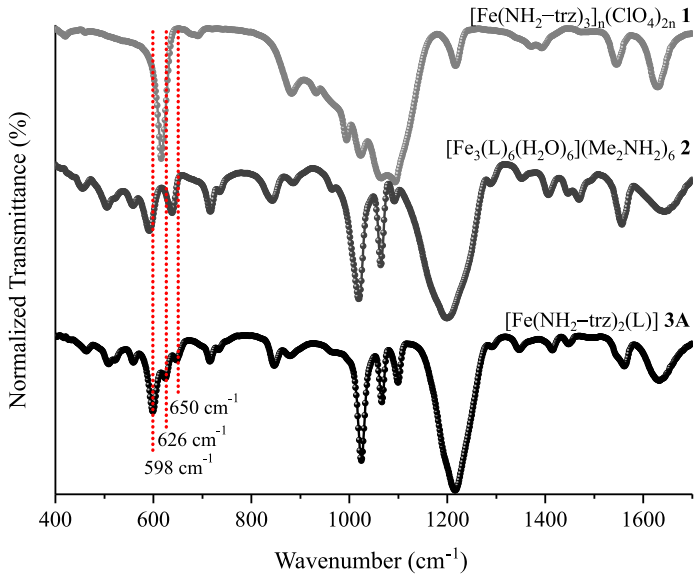

Figure 4. Infrared spectra of **1**, **2** and **3A** in the 400–1700 cm^{-1} range.

SCO behaviour

The thermal dependence of the spin state in **1**, **2** and **3A** was evaluated by measuring their magnetic susceptibility (χ_m) in the 160–260 K range for **1** and in the 200–400 K range for **2** and **3A** (Figure 5). A magnetic hysteresis cycle was observed for all the compounds. **1** presents a thermal hysteresis with $T_{1/2}(\uparrow)$ = 218 K and $T_{1/2}(\downarrow)$ = 212 K (ΔT = 6 K), as previously reported.[14] As observed in Figure 5b, the trimer **2** showed a HS–LS–HS configuration at room temperature ($\chi_m T$ (300 K) = 5.92 emu·K/mol) and a smooth transition to a HS–HS–HS configuration is observed above 360 K, reaching a maximum after 4 hours at 400 K ($\chi_m T$ (400 K, 4 hours) = 8.23 emu·K/mol). The thermal loop in **2** was of 80 K ($T_{1/2}(\uparrow)$ = 400 K and $T_{1/2}(\downarrow)$ = 320 K, similar to the reported ones). Moreover, **2** performed TIESST phenomena, in which 88% of the HS–HS–HS state could be trapped with a cooling down of 10 K/min, with a T(TIESST) of 240 K. The magnetic measurements of **3A** revealed a different SCO behaviour. **3A** presented a magnetic hysteresis cycle with abrupt transitions where $T_{1/2}(\uparrow)$ = 328 K and $T_{1/2}(\downarrow)$ = 284 K defined a hysteresis loop of ΔT = 44 K (Figure 5c). The abruptness of the transitions, wide hysteresis and $\chi_m T$ value in the HS state ($\chi_m T$ = 3.23 emu·K/mol) also suggests that we are dealing with a polymeric compound. We also observed that all the scan rates produced a HS trapping of the compound (TIESST), with a T(TIESST) of 240 K. When cooling down with a 5 K/min scan rate, 43% of the Fe(II) centres were trapped in the HS state and less trapping was produced for slower scan rates (36% for 2 K/min, 29% for 1 K/min and 20% for 0.3%). This trapping behaviour is similar than the observed in compound **2** and is attributed to the activation energy barrier that arises from the electrostatic repulsion between sulfonate groups on adjacent triazole ligands which get closer upon the LS to HS transition.[12]

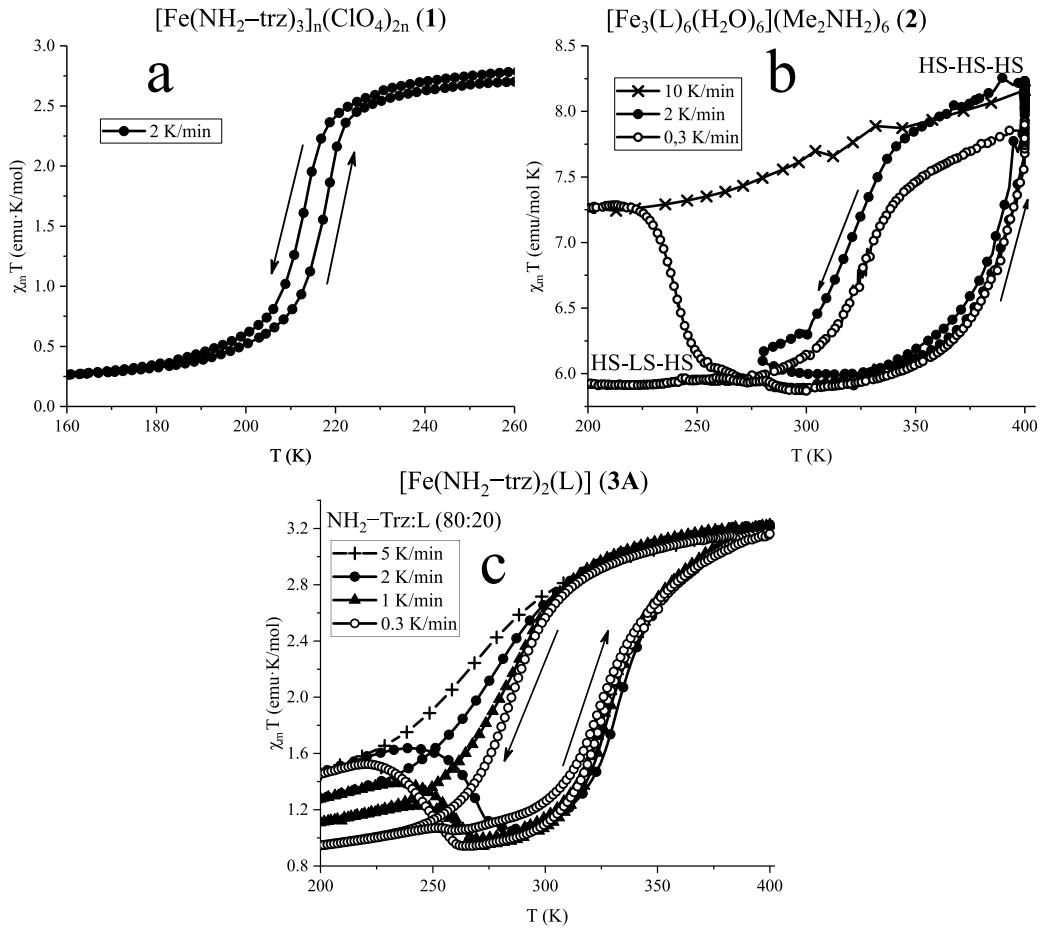

Figure 5. Magnetic susceptibility analysis vs temperature in the 160–260 K for **1** and in the 200–400 K range for **2** and **3A**.

Crystallographic phase transitions

The spin transitions in SCO cooperative systems are usually accompanied by a crystallographic phase transition that can be followed by powder X-ray diffraction (PXRD) and differential canning calorimetry (DSC) techniques. We performed Powder PXRD to all our samples at the temperatures at which the compounds are in LS and HS (Figure 6 and Figure S2.8). The initial PXRD of **1** pattern at 300 K (HS) showed a high degree of crystallinity in the 7.5–35º 2θ range (Figure 6a). Upon cooling down to 113 K (LS) slight changes were observed in the lattice parameters, as some of the peaks (8.6,

18.5, 20.6 and 22.1º) subtle shifted towards higher 2θ values, meanwhile others remained in the same position. Upon warming back to 300 K, these peaks recovered the initial position. Moreover, the doublets observed at 9º evolved into a singlet with a shoulder and the peak at 19º almost disappear upon the HS→LS transition, suggesting that the spin transition might accompanied by a crystallographic phase transition. Unfortunately, we were not able to perform DSC analysis of **1** since the available equipment cannot reach the temperatures at which the transition occurs.

Compound **2** showed a much more complex PXRD pattern with differences in the diffractograms at 300 K and 400 K (Figure 6b): the two peaks observed at 8º and 17º in the LS state disappeared in the HS state; in the 12–15º region, the triplet (12.38º, 12.86º, 13.4º), doublet (14.57º, 14.99º) turned into a singlet (12.68º), doublet (13.37º, 13.67º), doublet (14.6º, 14.84º); and, finally, a peak at 10º appeared in the HS state. These changes may be associated to a normal breathing of the unit cell upon heating since the DSC analysis did not detect any phase transition.[12]

In the case of **3** (Figure 6c), a reversible change to a more amorphous phase was produced when heating the sample at 400 K. Most of the peaks disappeared upon the LS→HS transition and, surprisingly, the remaining ones shifted to higher 2θ values, suggesting that the unit cell can suffer contractions in some orientations. The cell contraction is unusual in Fe(II) SCO complexes during LS→HS transition since the population of the e_g orbitals produces larger metal to ligand distances and an expansion of the total volume of the molecule (5–15%). Thus, this transition can induce a reorganization of the molecules in some directions into a more compact packing. The absence of peaks in the DSC measurements of **3** revealed that the contraction of the unit cell is not associated to a crystallographic phase transition. This fascinating behaviour can be attributed to the charged SO_3^- groups of the L bridging ligands. The increase in the Fe–N distances upon the spin transition produces an elongation in the chain direction, leading to a less stable structure in which the hydrogen bond interactions among the sulfonate anions and the protons from the 4–amino radical in the NH_2–trz are weaker.

To overcome this situation, a contraction in the other crystallographic directions of the lattice is produced, shifting the peaks in the diffractogram to higher *2θ*.

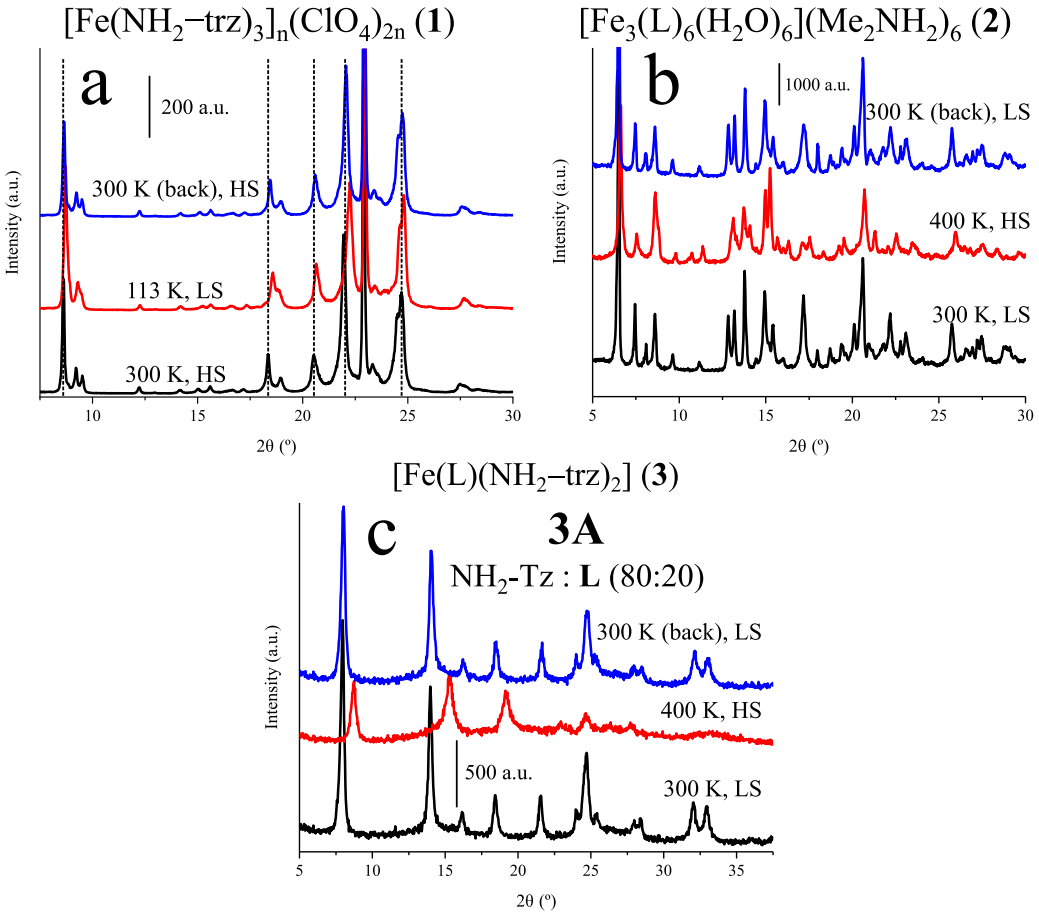

Figure 6. PXRD diffractograms of **1** (a), **2** (b) and **3A** (c) in the temperatures at which the SCO is in LS, HS and back in LS state.

Conclusions

In this chapter, we have used a mixing ligand approach to synthetize a neutral SCO chain made of two different triazole-based ligands (anionic ligand, L and neutral ligand, NH_2–trz) which, individually mixed with Fe(II) salts, lead to completely different structures (trimeric and 1D polymeric structure, respectively). Elemental analysis, EDX and PXRD results were used to conclude

that, instead of changing only the chemical environment of the pattern structure, as in the previous reports, a completely new compound was obtained with constant formula of $[Fe(L)(NH_2–Trz)_2]$ (**3**) with different structure and properties than the pattern **1** and **2**. The magnetic properties of **3** showed abrupt transitions at 328 and 284 K in the warming and cooling branches, respectively (ΔT = 44 K). Bistability was achieved at room temperature with TIESST effect for cooling scan rates higher than 1 K/min with a *T(LIESST)* at 240 K. We are currently trying to obtain more crystalline samples towards a better understanding of its structural properties.

References

[1] J. R. Galán-Mascarós, E. Coronado, A. Forment-Aliaga, M. Monrabal-Capilla, E. Pinilla-Cienfuegos, M. Ceolin, *Inorg. Chem.* **2010**, 49, 5706.

[2] T. Forestier, S. Mornet, N. Daro, T. Nishihara, S. I. Mouri, K. Tanaka, O. Fouché, E. Freysz, J. F. Létard, *Chem. Commun.* **2008**, 4327.

[3] I. Boldog, A. B. Gaspar, V. Martínez, P. Pardo-Ibañez, V. Ksenofontov, A. Bhattacharjee, P. Gütlich, J. A. Real, *Angew. Chem.* **2008**, 120, 6533.

[4] P. Gütlich, V. Ksenofontov, A. B. Gaspar, *Coord. Chem. Rev.* **2005**, 249, 1811.

[5] J. Linares, E. Codjovi, Y. Garcia, *Sensors* **2012**, 12, 4479.

[6] C. Faulmann, J. Chahine, I. Malfant, D. De Caro, B. Cormary, L. Valade, *Dalt. Trans.* **2011**, 40, 2480.

[7] Y. H. Luo, C. Chen, G. W. Lu, D. L. Hong, X. T. He, C. Wang, J. Y. Wang, B. W. Sun, *J. Phys. Chem. Lett.* **2018**, *9*, 7052.

[8] J. Kröber, E- Codjovi, O. Kahn, F. Grolière, C. Jay, *J. Am. Chem. Soc.* **1993**, 115, 9810.

[9] I. Suleimanov, J. S. Costa, G. Molnár, L. Salmon, I. Fritsky, A. Bousseksou, *Fr. Ukr. J. Chem.* **2015**, 3, 66.

[10] N. Calvo Galve, E. Coronado, M. Giménez-Marqués, G. Mínguez Espallargas, *Inorg. Chem.* **2014**, 53, 4482.

[11] C. Bartual-Murgui, C. Pérez-Padilla, S. J. Teat, O. Roubeau, G. Aromí, *Inorg. Chem.* **2020**, 59, 12132.

[12] V. Gómez, C. Sáenz De Pipaón, P. Maldonado-Illescas, J. C. Waerenborgh, E. Martin, J. Benet-Buchholz, J. R. Galán-Mascarós, *J. Am. Chem. Soc.* **2015**, 137, 11924.

[13] A. Lapresta-Fernández, M. P. Cuéllar, J. M. Herrera, A. Salinas-Castillo, M. D. C. Pegalajar, S. Titos-Padilla, E. Colacio, L. F. Capitán-Vallvey, J. *Mater. Chem. C* **2014**, 2, 7292.

[14] E. Smit, M. Bouchaib, D. Waal, *J. Raman Spectrosc.* **2001**, 32, 339.

[15] T. A. D. Nguyen, J. M. Veauthier, G. F. Angles-Tamayo, D. E. Chavez, E. Lapsheva, T. W. Myers, T. R. Nelson, E. J. Schelter, *J. Am. Chem. Soc.* **2020**, 142, 4842.

[16] W. R. Robinson, *J. Chem. Educ.* **1985**, 62, 1001.

[17] M. M. Dîrtu, C. Neuhausen, A. D. Naik, A. Rotaru, L. Spinu, Y. Garcia, *Inorg. Chem.* **2010**, 49, 5723.

[18] V. Y. Sirenko, O. I. Kucheriv, A. Rotaru, I. O. Fritsky, I. A. Gural'skiy, *Eur. J. Inorg. Chem.* **2020**, 2020, 4523.

[19] J. G. Haasnoot, W. L. Groeneveld, *Z. Naturforsch. B* **1977**, 32b, 533.

[20] J. G. Haasnoot, G. Vos, W. L. Groeneveld, *Z. Naturforsch. B* **1977**, 32b, 1421

Supporting Information of Chapter 2.

Mixed-Ligand Triazole-Based SCO Chains: Tuning Temperature and Thermal Hysteresis

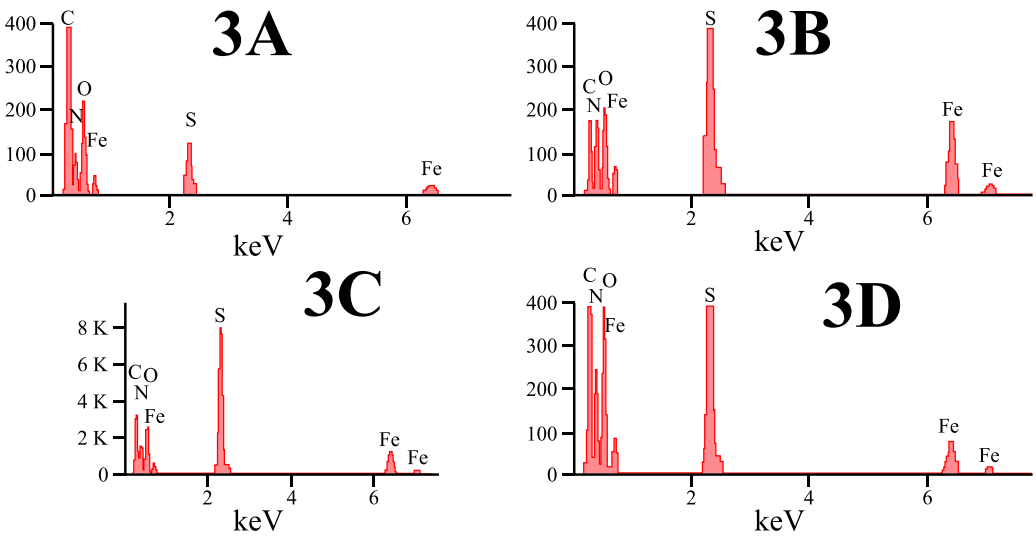

Figure S2.1. EDX analysis of **3A**, **3B**, **3C** and **3D**.

Table S2.1. Atomic composition from EDX analysis of **3A**, **3B**, **3C** and **3D**.

	Atom %				
Sample	C	N	O	S	Fe
3A	35.30	36.23	25.15	2.09	1.23
3B	22.88	33.43	32.78	7.53	3.38
3C	30.65	27.77	30.34	7.67	3.59
3D	30.58	26.15	17.60	10.58	5.08

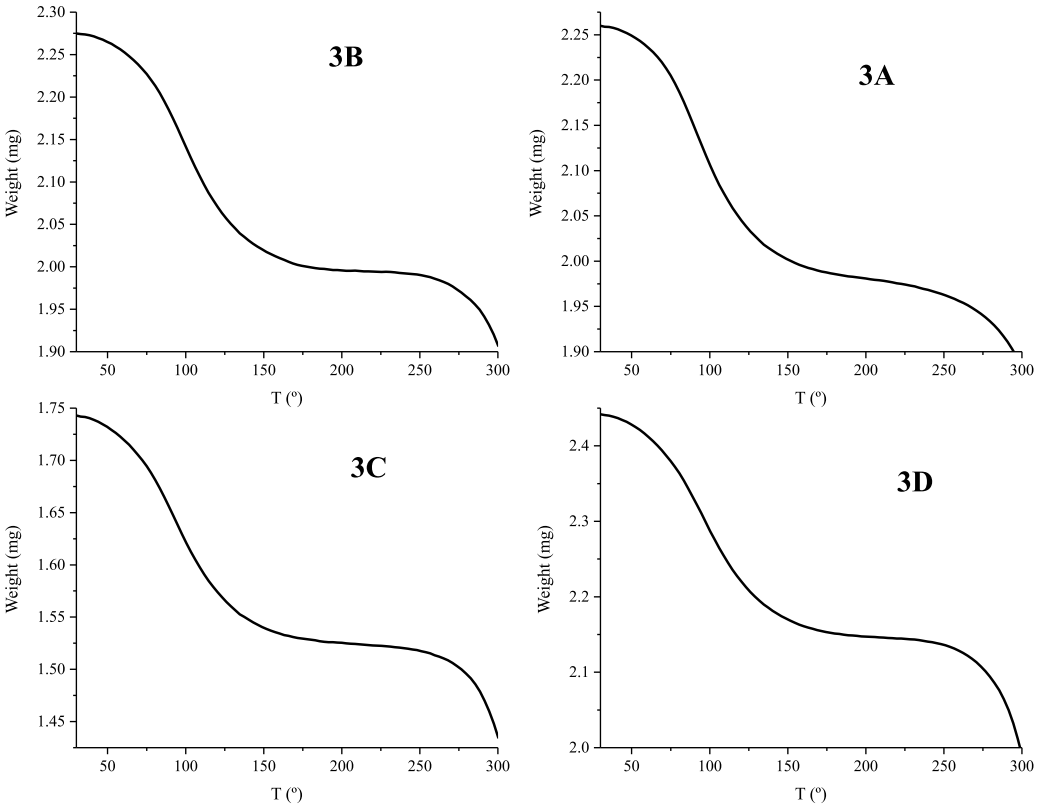

Figure S2.2. TGA analysis of **3A**, **3B**, **3C** and **3D**.

TableS2.2. Water molecules calculation from TGA anális.

Sample	[Fe(L)(NH_2-trz)$_2$] Weight (mg)	[Fe(L)(NH_2-trz)$_2$] mol	H_2O Weight (mg)	H_2O mol	n·H_2O
3A	1.98	$4.15E^{-6}$	0.28	$1.73E^{-5}$	4.18
3B	1.99	$4.18E^{-6}$	0.27	$1.72E^{-5}$	4.13
3C	1.53	$3.19E^{-6}$	0.21	$1.33E^{-5}$	4.18
3D	2.15	$4.50E^{-6}$	0.29	$1.80E^{-5}$	4.01

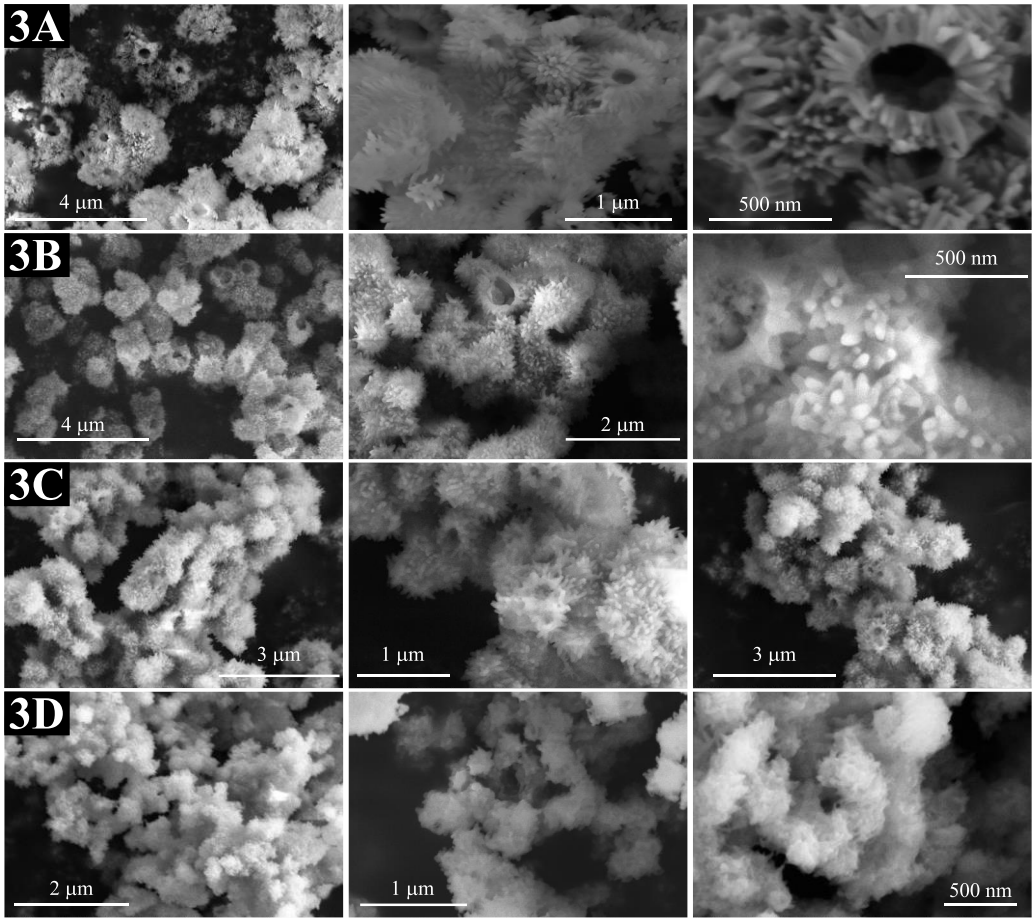

Figure S2.3. FESEM figures of **3A**, **3B**, **3C** and **3D**.

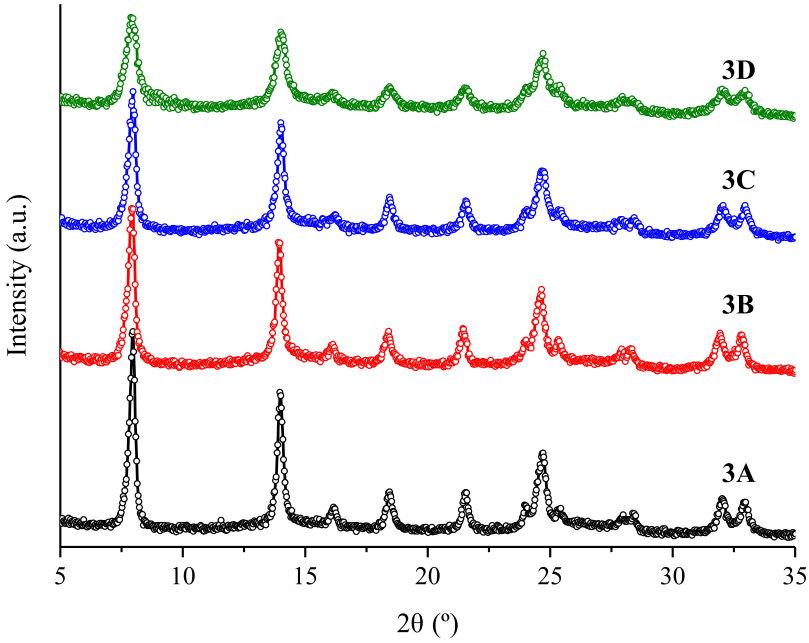

Figure S2.4. PXRD patterns of **3A**, **3B**, **3C** and **3D** in the 5–35º range at 300 K.

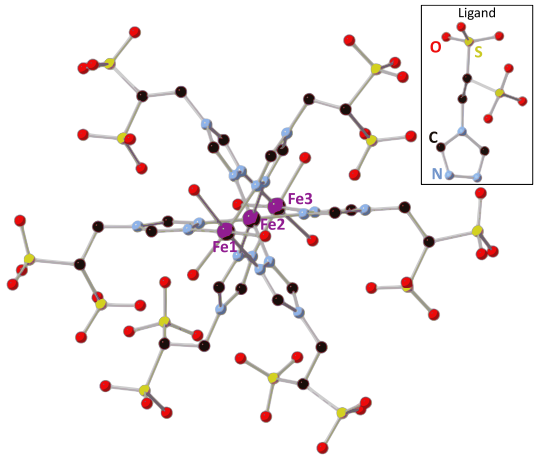

FigureS2.5. Molecular structure of the polyanionic Fe(II) $[Fe_3(\mu\text{-}L)_6(H_2O)_6]^{6-}$ complex (L = 4-(1,2,4-triazol-4-yl)ethanedisulfonate). Structure from CCDC, Deposition number: 1016539.

Synthesis and Characterization of $[Fe(NH_2–trz)_3]_n(SO_4)_n$

$[Fe(NH_2–trz)_3]_n[SO_4]_n$ (8). 4.5 g of $FeSO_4$ (16.19 mol) and 0.70 g of ascorbic acid (3.9 mmol) were dissolved in 30 mL of water and a solution of 3.9 g of NH_2–trz (46.41 mmol) in 30 mL of water was added dropwise. After 12 h, the pink solution was centrifuged and washed with water and ethanol several times. The obtained precipitate was dried under vacuum for 5 hours and the powder was homogenized by pestle and mortar, resulting 5.45 g (yield = 83%).

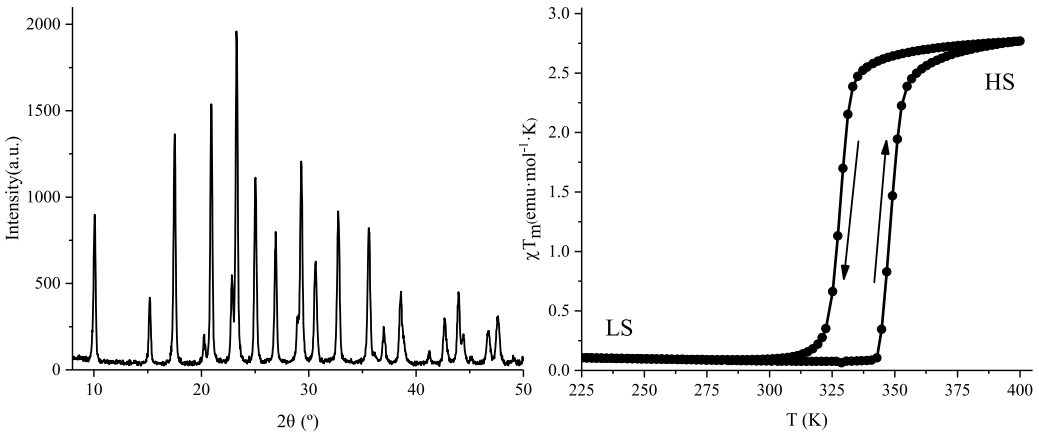

Figure S2.6. PXRD (left) and SQUID (right) measurements of $[Fe(NH_2–trz)_3]_n(SO_4)_n$.

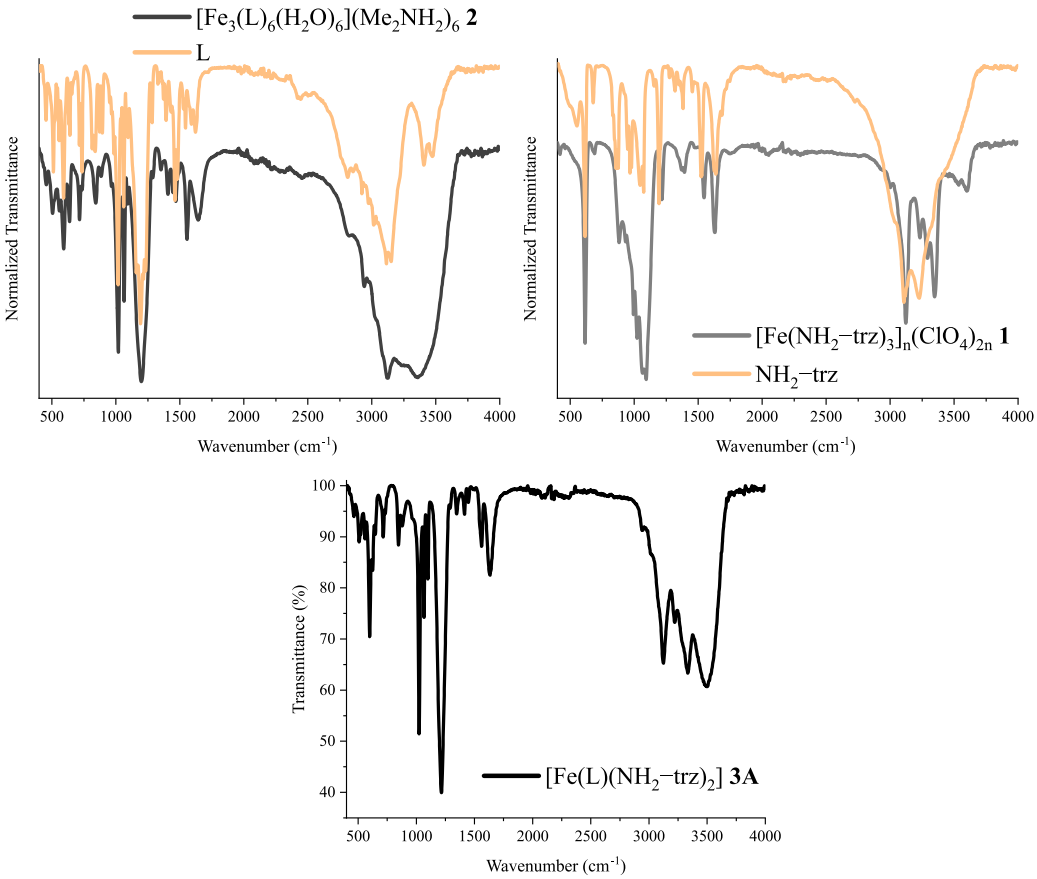

Figure S2.7. IR analysis in the 400-400 cm-1 range for **1** and NH_2−trz (a), **2**, and L (b) and **3A** (c).

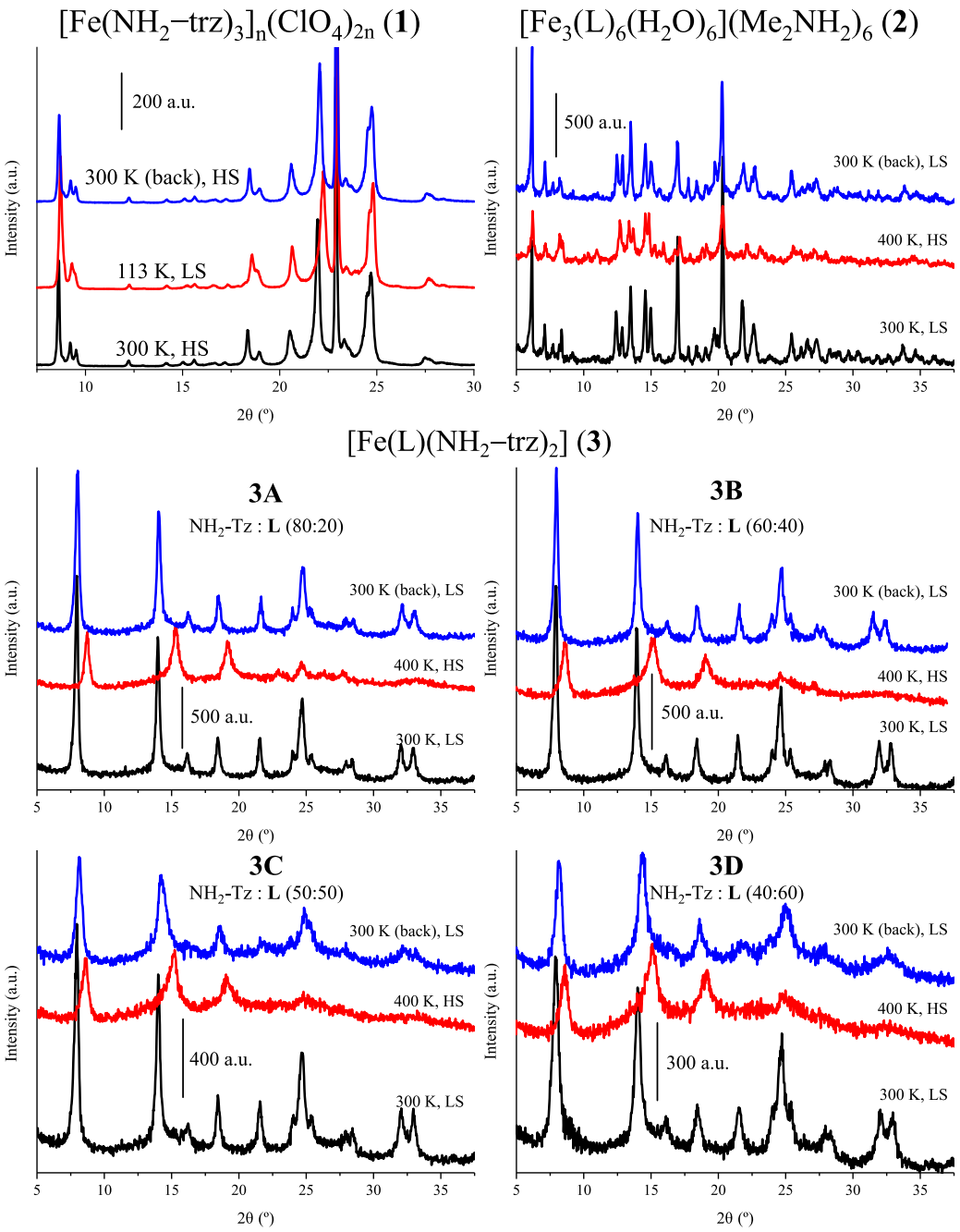

Figure S2.8. PXRD diffractograms of **1**, **2**, **3A**, **3B**, **3C** and **3D** at the temperatures at which the SCO is in LS, HS and back in LS state.

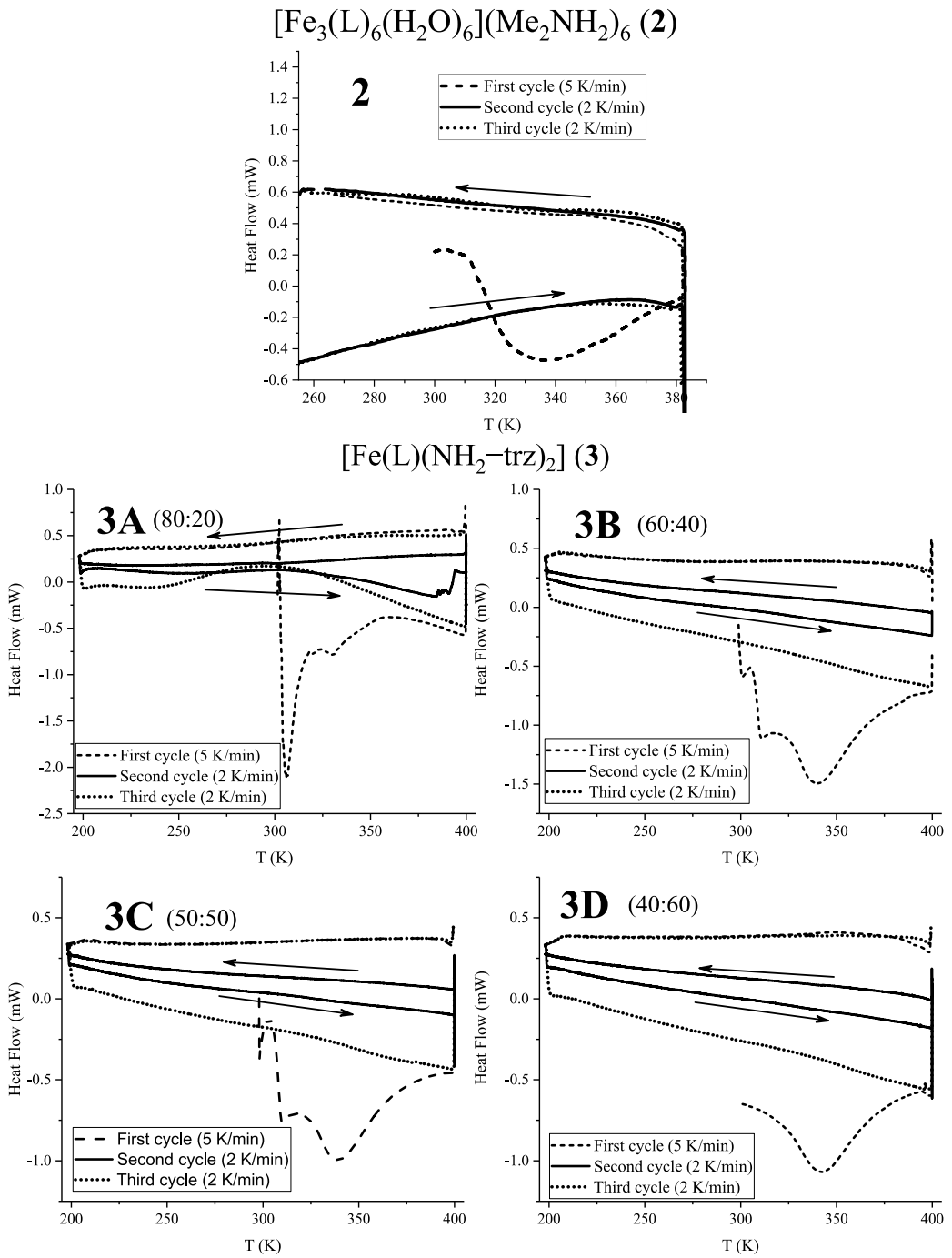

Figure S2.9. DSC analysis of **2**, **3A**, **3B**, **3C**, and **3D**.

Chapter 3. Mechanosynthesis of a Novel Cooperative SCO complex

Abstract

In this chapter, a mechanosynthesis approach will be used for the obtention of a new SCO compound with different structure and magnetic properties than the observed in the solution-synthetized complex. Mechanosynthesis is a solventless approach that can offer several advantages over solution synthesis such as rapidity and selectivity. For this reason, we decided to use this strategy to synthesize a SCO compound with the anionic 4−(1,2,4−triazol−4−yl)ethanedisulfonate ligand (L) that, in solution with iron salts, results in a trimeric complex. Polymer chains of this compound would be interesting to synthesize, as they usually exhibit more abrupt transitions and wider hysteresis due to long-range interactions. The mechanosynthesized compound, obtained after grinding L with solvated $Fe(ClO_4)_2$, exhibited abrupt transitions and a narrow hysteresis, completely different than the SCO behaviour in the trimeric complex obtained in solution.

Introduction

Mechanochemistry refers to those reactions, usually in the solid-state, induced by mechanical forces, such as grinding in a ball milling reactor. Grinding applications were firstly based in the physical side reduction of materials, such as minerals, paints and medicines.[1] In 1919, mechanochemistry was accepted as a branch of chemistry when Ostwald included it as one of the sub-disciplines of chemistry, together with thermochemistry, electrochemistry and photochemistry.[2] Synthesis via mechanochemistry, known as mechanosynthesis, is a promising green solution to avoid the increasing waste of fossil-derived solvents involved in many industrial processes.[3] Moreover, it presents several advantages over solution-based methods such as rapidity, no side products, less energy needed, less time consuming, high selectivity and high product yields.[4] For all these reasons, mehcanosynthesis has gained attention for the synthesis of pharmaceutical materials,[5] coordination compounds,[6] co-crystals,[7] supramolecular compounds,[8] metal-organic frameworks,[9] nanoparticles,[10] or alloys.[11]

First approaches of mechanochemistry in SCO compounds were performed in 1980, when Hendrickson et al. studied the effects in the magnetic properties of post-synthethic grinding.[12–15] However, mechanosynthesis of SCO compounds has not been reported until 2018 when Askew and Shepherd synthesized, for the first time, the 1D SCO $[Fe(NH_2–trz)_3]_n(SO_4)_n$ (NH_2–trz = 4–amino–1,2,4–triazole) grounding $[Fe(SO_4)_2](NH_4)_2·6H_2O$ and NH_2–trz in a pestle and mortar without solvent for 5 minutes.[16] After 30 seconds, they observed a change in colour, from white (as the reagents) to purple (common in triazole based Fe(II) SCO compounds in the LS state). The magnetic properties of the grinded compound were virtually indistinguishable from the solution-synthesized one. However, the PXRD patterns showed additional peaks for the mechanosynthesized compound, attributed to water loss from the lattice.

In this chapter, we summarized the results obtained using the mechanosythesis for the obtention of a Fe(II) SCO compound. The ligand 4–(1,2,4–triazol–4–yl)ethanedisulfonate (L) and $Fe(ClO_4)_2$, which coprecipitate in solution as a trimer (described in Chapter 2), have been grinded in a ball milling reactor. Notably, the mechanosynthesized solid exhibits different structure and SCO behaviour than the solution-synthesized trimer, as observed via different techniques.

Experimental section

Caution! Perchlorate compounds are very explosive under mechanical stress. The amino radicals in the structure can induce instability, producing bigger explosions. Mechanochemical techniques should not be used for the synthesis of cationic SCO complexes with perchlorate as counteranion.[17,18] 0.1 g of $Fe(ClO_4)_2·xH_2O$ was left open for 1 day in the fume hood, to be as hydrated as possible.

$[Fe_3(L)_6(H_2O)_6](Me_2NH_2)_6$ (**2**, L = 4–(1,2,4–triazol–4–yl)ethanedisulfonate). The ligand L was obtained as the dimethlammonium salt $(Me_2NH_2)_2L$ following a literature procedure.[19] 0.1 g of $Fe(ClO_4)_2·6H_2O$ (0.3 mmol) was dissolved in 2.5 mL of Milli–Q water a small amount of ascorbic acid, 0.3 g of $(Me_2NH_2)_2L$ (0.9 mmol) were dissolved in 2.5 mL of Milli–Q water and both solutions were mixed together and stirred during

30 min. The addition of ethanol led the precipitation of a pink solid that was centrifuged and washed with ethanol and diethyl ether and dried under vacuum.

[FeL_x] (**4**). 5 mg of L (0.15 mmol) and 12 mg of $Fe(ClO_4)_2 \cdot xH_2O$ (0.05 mmol) were mixed in a Mixer MM 200 (Retsch) in a 25 mL stainless-steel reactor with two stainless-steel balls (6.9 g each ball) for 10 minutes. The product obtained was a purple wax sticked to the steel balls. The product was scratched from the balls using a spatula, stored and labelled as **4**. The same synthesis was performed washing the solid obtained with ethanol and diethyl ether and dried under vacuum; this powder was labelled as **4**–washed.

See Annex I for the physical methods used in this chapter: Differential scanning calorimetry (DSC), Energy dispersive X-ray (EDX) / Field Emission scanning electron microscopy (FESEM), Single crystal X-ray diffraction (SCXRD), Powder X-ray diffraction (PXRD), Magnetic susceptibility measurements (SQUID), Nuclear magnetic resonance (NMR).

Results and discussion

As reported by our group, the mixture in solution of the anionic ligand 4–(1,2,4–triazol–4–yl)ethanedisulfonate (L) and Fe(II) ions leads to the formation of a linear trinuclear SCO complex (**2**). In order to go towards a green synthetic protocol and observe the differences in the product, we mixed these reagents in solid state in a ball milling reactor. After 10 minutes of milling, a deep pink waxy solid was obtained (**4**). Since the waxy solid was soluble in water, a batch of it was washed with organic solvents to remove the impurities from the excess of the starting materials or impurities from the ball milling reactor (**4**–washed). Mechanosynthesis and post-synthetical grinding can induce changes in the magnetic properties of the SCO compounds, introducing defects in the structure, structural and magnetic characterization of this powder is necessary.[12–16]

The trimeric structure of the solution-synthesized **2** was described in detail in Chapter 2. The powder X-ray diffraction (PXRD) pattern of the mechanosynthesized compound **4**

revealed a different structure than the solution-synthesized compound (**2**), as none of the peaks observed in **4**, at 5º and in the 12.5º and 27.5º *2θ* range, matched with any of the diffraction peaks of the pattern of **2** (Figure 1a and 1b). After the washing step (**4**–washed), the peaks became better defined due to the removal of an amorphous phases (Figure S3.1). However, the few peaks observed, and the low crystallinity of the powder precludes the structural determination.

The washing step also induced changes in the morphology of the sample, since the waxy pink solid evolved into a fine powder (Figure S3.1, inset). Moreover, via environmental scanning electron microscope (ESEM), it could be noted that the large size of the agglomerated particles in **4** (bigger than 500 μm) were decreased into finer particles upon washing (Figure S3.2, left).

As previously commented and in contrast to polymeric 1D SCO structures known to date, compound **4** was soluble in water, allowing the obtention of crystals via vapor diffusion with ethanol. The preliminary structure of the crystals, analysed by single-crystal X-ray diffraction (SCXRD), contained the same trinuclear polyanion, $[Fe_3(L)_6(H_2O)_6]^{6-}$, than compound **2** (Figure S3.3 and Table S3.2), indicating that compound **4** cannot be obtained from solution synthesis since the trimer arrangement is more insoluble and crystallizes first.

In order to obtain details about the stoichiometry of this new compound, energy-dispersive X-ray spectroscopy (EDX) was performed to **4** and **4**–washed (Figure S3.2, right and Table S3.1). As the dianionic ligand L contains 2 sulfonate groups, the Fe:S ratio can give us information about the amount of L in the Fe(II) sphere. The Fe:S ratio in the as-prepared compound **4** is 1:8.4, suggesting that there are 4 ligands per atom of Fe(II). A high amount of Cl was also found (1,7 per Fe(II) atom), indicating presence of the starting materials (perchlorate, dimethylammonium, etc.). After several washing steps, part of the starting materials were partially removed, (Cl per Fe(II) was reduced from 1,7 to 0,7). However, simple washing cannot reach a total removal of these impurities that are maybe trapped or co-crystallized with the Fe(II) containing material.

Stoichiometry cannot be deduced with these results, thus ICP is being carried out to acquire more information about the composition of 4.

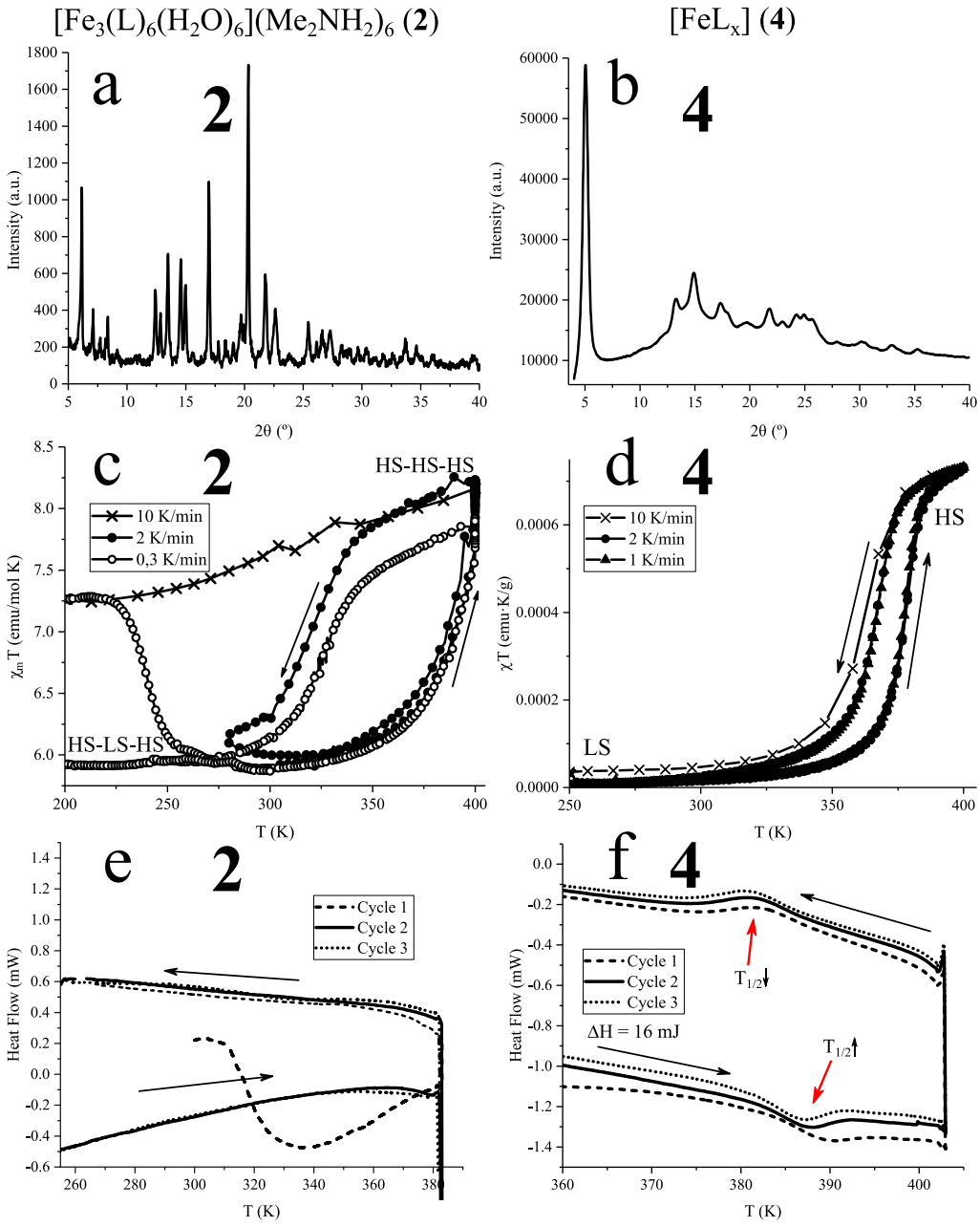

Figure 1. PXRD patterns of **2** and **4** in the 2–40º range (a and b). $\chi_m T$ vs T analysis for **2** and **4** in the 200–400 and 250–400 K temperature ranges, respectively (c and d). DSC measurements in the temperature ranges of the spin transitions of **2** and **4** (e and f).

The magnetic behaviour of this new compound (**4**) was evaluated in the 200−400 K range and compared with the solution-synthesized one (**2**) (Figures 1d and 1c, respectively). As described in Chapter 2, the trinuclear complex **2** showed a wide hysteresis of 90 K, defined by the HS−LS−HS to HS−HS−HS transitions ($T_{1/2}(\uparrow)$ = 400 K and $T_{1/2}(\downarrow)$ = 310 K) and TIESST with $T(TIESST)$ = 240 K. A completely different SCO behaviour was observed in compound **4** (Figure S3.4 for corrections), which performed a reproducible 10 K hysteresis at different scan rates (1, 2 or 10 K/min) with abrupt transitions at $T_{1/2}(\uparrow)$ = 377 K and $T_{1/2}(\downarrow)$ = 367 K. Moreover, in this case, fast cooling downs (10 K/min) did not trap the HS state in the metastable state (TIESST). Magnetic susceptibility data can also give information about the purity of the SCO active compound. Since there is only one complete spin transition in the magnetic response, we can affirm that in the 250−400 K range there is only one compound performing SCO and that the rest of paramagnetic or diamagnetic impurities do not participate in the spin transition.

Another difference with the solution-synthesized sample was observed via differential scanning calorimetry (DSC) analysis (Figure 1e and 1f). As previously reported and discussed in Chapter 2, the spin transition in **2** did not occur with endothermic and exothermic processes. Whereas, in **4** the spin transition could be followed by DSC since two low intense peaks with an enthalpy of 16 mJ were observed in successive cycles, one endothermic at 387 K (LS→HS) and an exothermic one at 380 K (HS→LS), in good agreement with the magnetic data, indicating the existence of a phase transition in **4**. This phase transition can also be followed by variable temperature PXRD. As observed in figure 2a, there is a change in the PXRD diffractogram at 400 K where the peaks at 15º and in the range of 21.5º and 25.7º in 2θ are shifted. Figure 2b shows the PXRD patterns in the 250−400 K range with a scan rate of 5 ºC/min. An abrupt and reversible change in the previously mentioned peaks is observed with transition temperatures in good agreement with SQUID and DSC analysis ($T_{1/2}(\uparrow) \approx 375$ K and $T_{1/2}(\downarrow) \approx 370$ K).

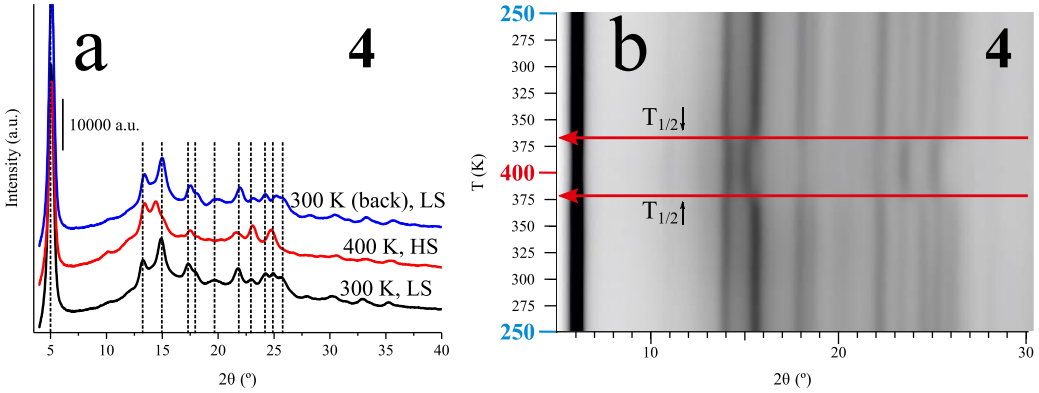

Figure 2. PXRD diffractograms of **4** at 300 K, 400 K (HS) and 300 K (back to LS) (a). PXRD mapping during spin crossover transition between 250 and 400 K for **4** (b).

Finally, To be sure that all these differences in the structural and magnetic properties are not caused by modifications of the 4–(1,2,4–triazol–4–yl)ethanedisulfonate (L) ligand upon grinding, we performed nuclear magnetic resonance (NMR) to the fresh ligand and to the ligand grinded during 15 min at 25 Hz. The NMR spectrum of both compounds matched showing only differences in the width of the signals (Figure S3.5).

Conclusions

In this chapter we have demonstrated that mechanosynthesis offers synthetic alternatives, allowing the obtention of new materials that are not reachable via traditional solution-based methods. Using same reagents with a different synthetic procedure have led to a new compound with different structure and magnetic properties than the solution-synthesized one. The hysteresis of the mechano-synthetized **4** was more abrupt, narrower and without LIESST phenomenon than the solution-synthesized material (**2**). Further investigations about this new complex and an optimization of the method are required in order to obtain reliable structural information.

References

[1] L. Takacs, *Chem. Soc. Rev.* **2013**, 42, 7649

[2] Wilhelm Ostwald, *Lehrbuch der allgemeinen Chemie*, Wilhelm Engelmann, **1891**.

[3] S. L. James, C. J. Adams, C. Bolm, D. Braga, P. Collier, T. Friščić, F. Grepioni, K. D. M. Harris, G. Hyett, W. Jones, A. Krebs, J. Mack, L. Maini, A. G. Orpen, I. P. Parkin, W. C. Shearouse, J. W. Steed and D. C. Waddell, *Chem. Soc. Rev.* **2012**, 41, 413.

[4] W. Jones, M. D. Eddleston, *Faraday Discuss.* **2014**, 170, 9.

[5] T. Rajbongshi, K. Sarmah, R. Ganduri, *Chemistry-Methods* **2021**, 1, 408

[6] V. Cabras, M. C. Aragoni, S. J. Coles, R. Lai, M. Pilloni, E. Podda, A. Scano, G. Ennas, *Supramol. Chem.* **2017**, *29*, 865.

[7] A. Quashie, R. Kingsford-Adaboh, V. P. Y. Gadzekpo, *Science and Development*, **2017**, 1, 1.

[8] R. Cerón-Camacho, R. Cisneros-Dévora, E. Soto-Castruita, M. Pons.Jiménez, H. I. Beltrán, J. M. Martínez-Magadán, L. S. Zamudio-Rivera, *Arab. J. Chem.* **2019**, 12, 4664.

[9] M. Y. Masoomi, S. Beheshti, A. Morsali, J. Mater. Chem. A **2014**, 2, 16863.

[10] K. L. Da Silva, D. Menzel, A. Feldhoff, C. Kübel, M Bruns, A. Paesano, A. Düvel, M. Wilkening, M. Ghafari, H. Hahn, F. J. Litterst, P. Heitjands, K. D. Becker, V. Sepelák, J. Phys. Chem. 2011, 115, 7209.

[11] E. Jartych, *J. Magn. Magn. Mater.* **2011**, *323*, 209

[12] M. S. Haddad, W. D. Federer, M. W. Lynch, D. N. Hendrickson, *Inorg. Chem.* **1980**, 20, 131.

[13] M. Sorai, R. Burriel, E. F. Westrum, D. N. Hendrickson, *J. Phys, Chem. B* **2008**, 112, 4344.

[14] M. D. Timken, S. R. Wilson, D. N. Hendrickson, *Inorg. Chem.* 1985, 24, 3450.

[15] M. S. Haddad, W. D. Federer, M. W. Lynch, D. N. Hendrickson, *J. Am. Chem. Soc.* **1980**, 102, 1468

[16] J. H. Askew, H. J. Shepherd, *Chem. Commun.* **2018**, 54, 180.

[17] T. A. D. Nguyen, J. M. Veauthier, G. F. Angles-Tamayo, D. E. Chavez, E. Lapsheva, T. W. Myers, T. R. Nelson, E. J. Schelter, *J. Am. Chem. Soc.* **2020**, 142, 4842.

[18] W. R. Robinson, *J. Chem. Educ.* **1985**, 62, 1001.

[19] V. Gómez, C. Saenz de Pipaón, P. Maldonado-Illescas, J. C. Waerenborgh, E. Martin, J. Benet-buchholz, J. R. Galán-Mascarós, *J. Am. Chem. Soc.* **2015**, 137, 11924.

Supporting Information of Chapter 3.

Mechanosynthesis of a Novel Cooperative SCO complex

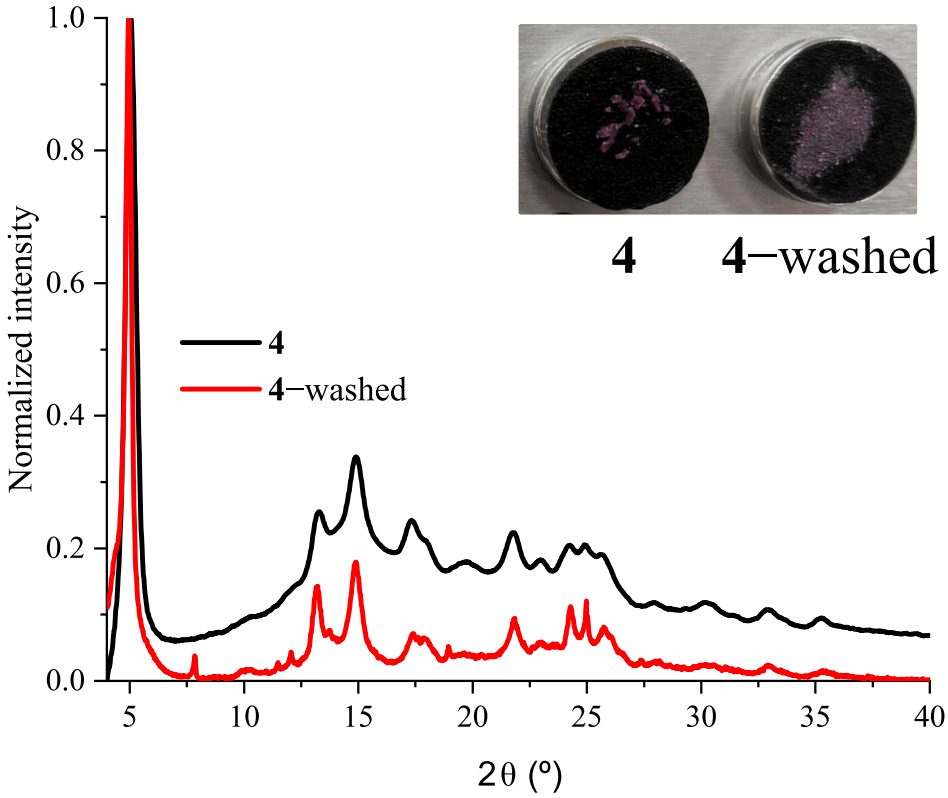

Figure S3.1. PXRD patterns of **4** and **4**–washed in the 4–40º 2θ range. The inset includes the evolution of **4** after being washed (**4**–whased).

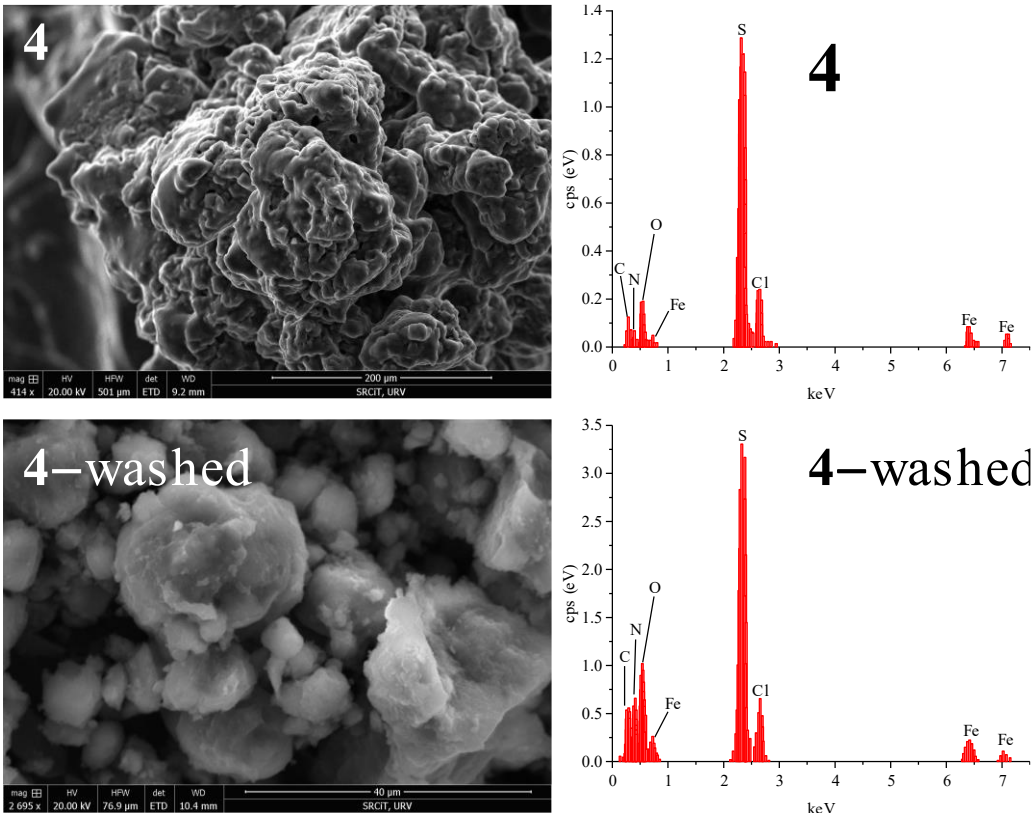

Figure S3.2. ESEM images (left) and EDX analysis (right) of **4** and **4**–washed.

Table S3.1. Atomic composition from EDX analysis of **4** and **4**–washed.

	Atom %					
Sample	C	N	O	S	Cl	Fe
	26.25	22.59	32.63	14.07	2.79	1.67
4	Atom/Fe atom					
	15,7	13,5	19,5	8,4	1,7	1,0
	38.85	22.97	30.39	6.07	0.74	0.99
4–washed	Atom/Fe atom					
	39,2	23,2	30,5	6,1	0,7	1

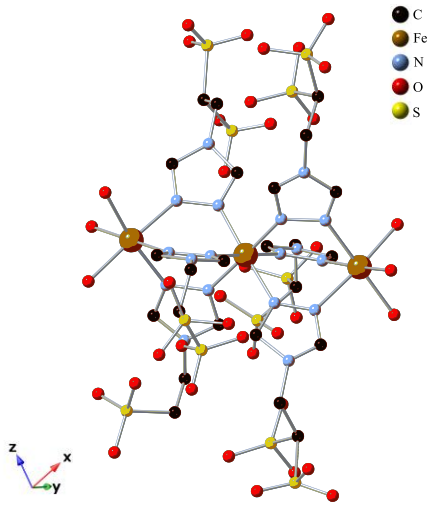

Figure S3.3. Preliminary structure of crystals after dissolving **4**.

Table S3.2. Preliminary crystallographic data of crystals obtained after dissolving **4**.

Formula	$C_{24}H_{54}Fe_3N_{18}O_{42}S_{12}$
Formula weigh	1818.315
T (K)	100(2)
Crystal system	Triclinic
Space group	P –1
a (Å)	14.238(2)
b (Å)	15.006(3)
c (Å)	21.087(3)
α (°)	81.489(4)
β (°)	80.690(5)
γ (°)	81.139(5)
V (Å^3)	4357.7(12)
Z	4
ρ_{calcd} (g cm^{-3})	1.139
μ (mm^{-1})	1.125
F (000)	1508
Refl. collected	23493
Ind.reflections	11675
θ range (º)	2.26–28.07
Index ranges	$-16 \leq h \leq 14$ $-16 \leq k \leq 11$ $-23 \leq l \leq 21$
Goodnesss-of-fit	2.622
R1 (I>2σ(I))	0.1783
wR2 (I>2σ(I))	0.4370

Temperature-independent residual paramagnetism corrections

The residual paramagnetism corrections were performed with the Curie-Weiss law (See Annex I).

$[Fe(\mu\text{–}L)_3]_n(MeNH_2)_{4n}$ (**4**)

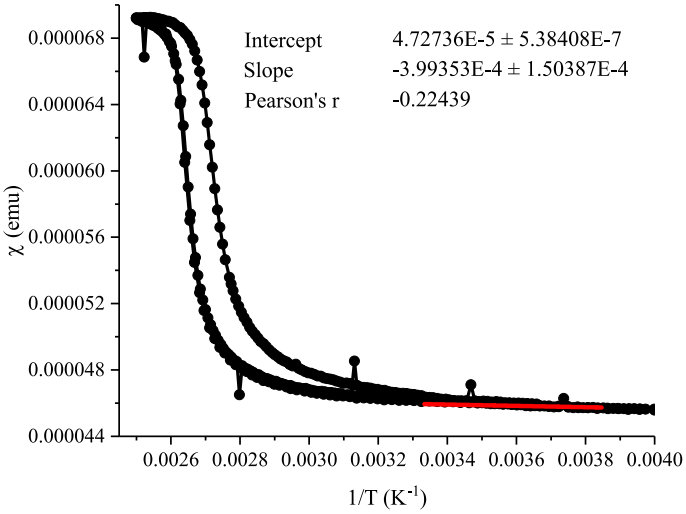

Figure S3.4. χ vs *1/T* of the last cycle and the residual temperature-independent paramagnetism correction (red line) of **4**.

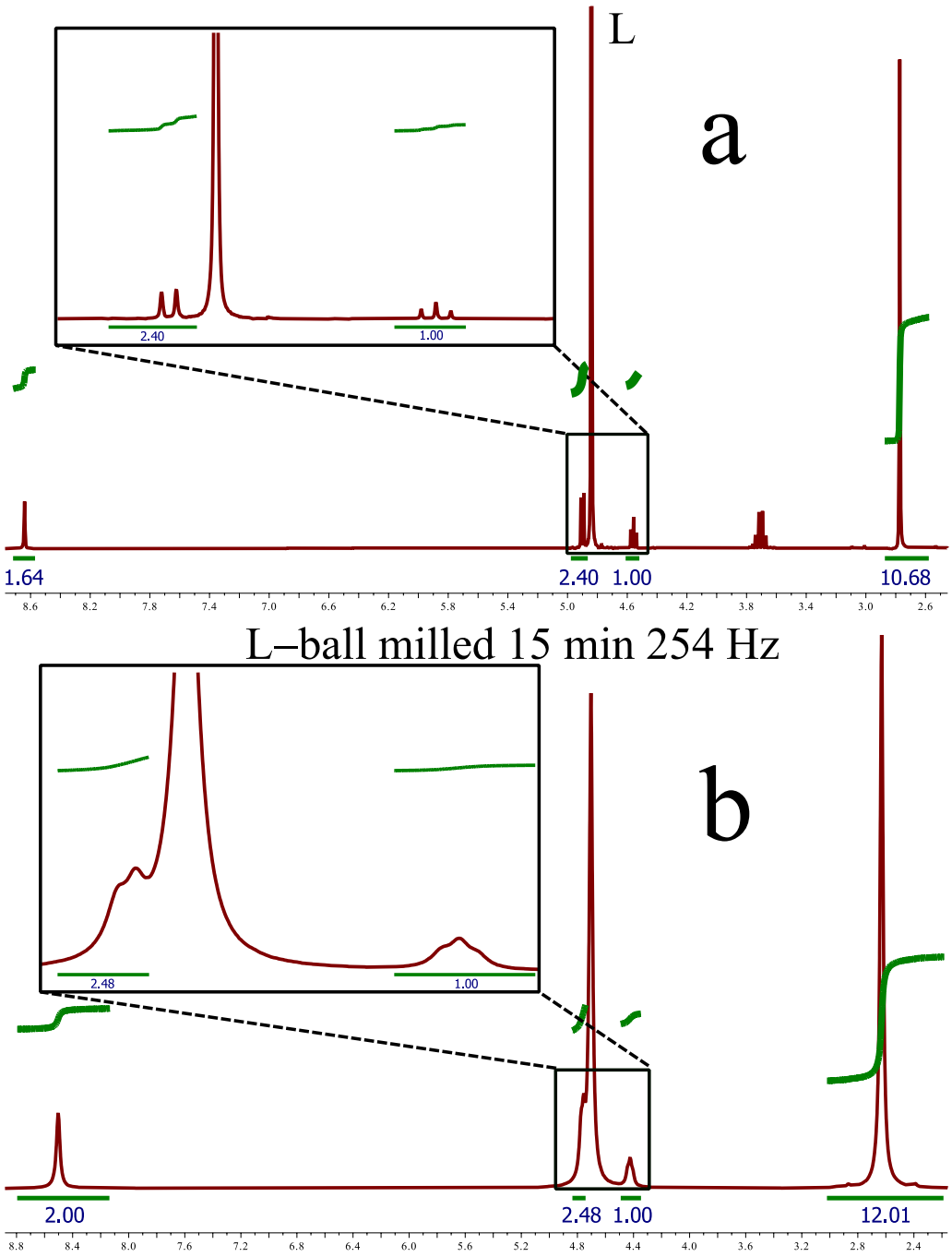

Figure S3.5. NMR of fresh 4–(1,2,4–triazol–4–yl)ethanedisulfonate (L) ligand (a) and L milled in a ball milling for 15 min at 25 Hz (b).

Chapter 4. Effect of Mechanochemical Recrystallization on the Thermal Hysteresis of 1D Fe(II)–triazole Spin Crossover Polymers

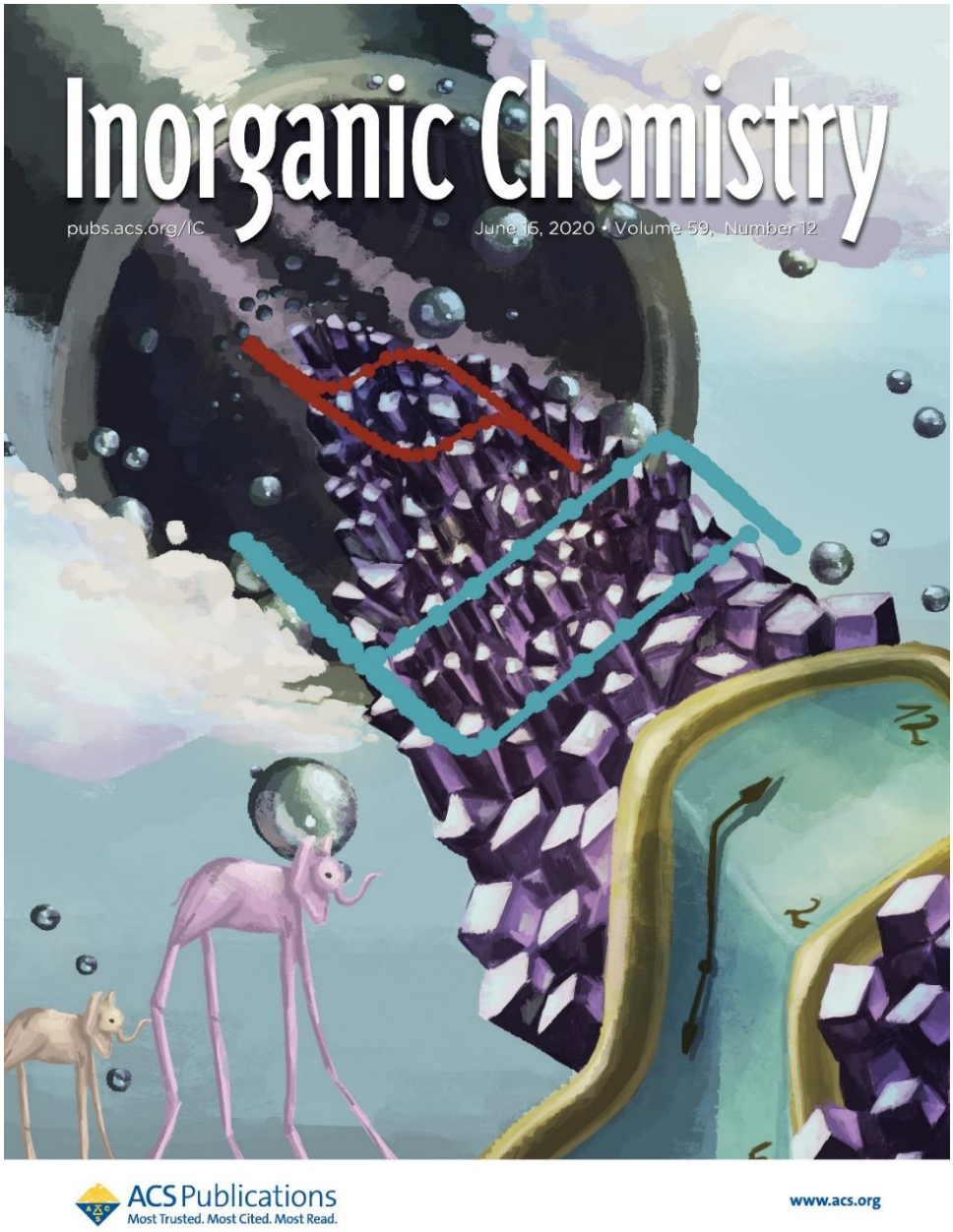

D. Nieto-Castro, F. A. Garcés-Pineda, A. Moneo-Corcuera, B. Pato-Doldan, F. Gispert-Guirado, J. Benet-Buchholz, J. R. Galán-Mascarós, *Inorg. Chem.* **2020**, 59, 7953.

Abstract

The thermal hysteresis in the cooperative spin crossover (SCO) polymers $[Fe(trz)(Htrz)_2]_n(BF_4)_n$ (**5**) and $[Fe(NH_2{-}trz)_3]_n(SO_4)_n$ (**6**) have been tuned by a simple ball milling grinding process. A change in the size and morphology of the crystallite domains due to the grinding protocol has been confirmed by complementary techniques, including ESEM and PXRD data. Upon milling, the regular cubic shape particles recrystallize with slightly different unit cell parameters and preferential orientations. This macroscopic change significantly modifies the thermally induced SCO behaviour, studied by temperature-dependent magnetic susceptibility, X-ray diffraction, and DSC analysis. Transition temperatures downshift closer to room temperature, while hysteresis widens, when particle sizes are actually decreasing. We relate this counterintuitive observation to subtle modifications in the unit cell, offering new alternatives to tune and enhance SCO properties in this class of 1D cooperative polymers.

Introduction

Different approaches have been used to modify the Spin crossover (SCO) behavior and bistability of Fe(II) compounds such as solid-state dilutions, which produce more gradual transitions and decrease the width of the hysteresis loop.[1–5] Size-control techniques, including reverse micelles, have allowed for the stabilization of nanoparticles,[6–10] whose nanometric size affects cooperativity and reduces the bistability regime,[11–14] decreasing the transition temperatures, and hysteresis width, down to disappearance of the memory effect.[8] Other strategies to modify the SCO transition include hydrostatic pressure[15–18] or chemical pressure (embedding into a polymeric matrix),[19,20] but there are just a few of reports focused in grinding effects on the SCO behaviour.[21–24] In these reports, the grinding effect in different Fe(III) salts, such as $[Fe(X\text{-}SalEen)_2]Y$ (SalEen = 2–(ethylamino)ethylimino)methyl) and [Fe(Hthpu)(thpu)] (thpu = pyruvic acid thiosemicarbazone), was studied, observing that grinding leads to incomplete and more gradual transitions and to a decrease of $T_{1/2}$. These changes were associated to the generation of defects caused by the grinding.

Mechanochemical synthesis is a quick and easy solventless preparation method.[25] It was reported as a viable method to prepare SCO compounds such as $[Fe(trz{-}NH_2)_3](SO_4)$, $[Fe(phen)_3](NCS)_2$, or $[Fe(pz)\{Au(CN)_2\}_2]$ from their molecular precursors. In these previous studies,[26] mechanochemical treatment produced materials with similar physical properties to those obtained from solution with just minimum side-effects in roughness. Recently, mechanochemistry has been used as a postsynthetic anion exchange procedure in $[Fe(NH_2{-}trz)_3]Cl_2$, obtaining a slightly decrease in the $T_{1/2}(\uparrow)$ and $T_{1/2}(\downarrow)$ values and a reduction in the abruptness of the transitions.[27] Furthermore, the mechanochemical synthesis and grinding effects have been studied in several minerals (illites, kaolinite, talc, etc.), clays,[28,29] and other materials (ZnO, SnO2 and ferrites) where physical solid-state properties are affected by this technique.[30–32]

We decided to study the effect of mechanochemical treatment of SCO compounds, obtained from solution, as a means to decrease the size and homogenize the as-prepared materials,[26,33,34] finding a potential effect on magnetic properties. Here, we report significant changes in the physical properties of $[Fe(trz)(Htrz)_2]_n(BF_4)_n$ and $[Fe(NH_2{-}trz)_3]_n(SO_4)_n$ after a ball milling protocol. The thermal hysteresis downshifts in temperature while becoming wider as a function of milling time. These findings open interesting opportunities to further tune and enhance the memory effect of SCO materials.

Experimental section

$[Fe(trz)(Htrz)_2]_n(BF_4)_n$ (**5**). First, 6.9 g of $Fe(BF_4)_2$ (20 mmol) and 0.7 g of ascorbic acid (4 mmol) were dissolved in 30 mL of water and a solution of 4.6 g of 1,2,4–triazole (66 mmol) in 3 mL of water was added dropwise. After 12 h, the pink solution was centrifuged and washed with water several times. The obtained precipitate was dried under vacuum for 5 hours and the powder was homogenized by pestle and mortar, resulting in 6.9 g of 1 (yield = 89%).

$[Fe(NH_2–trz)_3]_n(SO_4)_n$ (**6**). 4.5 g of $FeSO_4$ (16.2 mol) and 0.7 g of ascorbic acid (3.9 mmol) were dissolved in 30 mL of water and a solution of 3.9 g of NH_2–trz (46.4 mmol)

in 30 mL of water was added dropwise. After 12 h, the pink solution was centrifuged and washed with water and ethanol several times. The obtained precipitate was dried under vacuum for 5 hours and the powder was homogenized by pestle and mortar, resulting 5.4 g (yield = 83%).

Samples of **5** and **6** (≈ 0.35 g each) were treated under ball milling with a Mixer MM 200 (Retsch) in a 25 mL stainless-steel reactor with two stainless-steel balls (6.9 g each ball) at a frequency of 25 Hz at different times of 15, 30, 90 and 500 min (each sample was labelled by the total milling time: **5**−**15**, **5**−**30**, **5**−**90** and **5**−**500** for **5**; **6**−**15**, **6**−**30**, **6**−**90** and **6**−**500** for **6**).

See Annex I for the physical methods used in this chapter: Differential scanning calorimetry (DSC), Environmental scanning electron microscope (ESEM), Powder X-ray diffraction (PXRD), Magnetic susceptibility measurements (SQUID).

Results and discussion

Synthesis, particle size and morphology

$[Fe(trz)(Htrz)_2]_n(BF_4)_n$ (**5**) and $[Fe(NH_2–trz)_3]_n(SO_4)_n$ (**6**), as obtained from literature methods,[35,36] were treated by ball milling at different times between 15 and 500 min. We checked the evolution of particle sizes by ESEM (Figure S1). In ESEM images, as a function of milling time, we found that the particles became less agglomerated upon milling. These images indicated an additional change upon milling, related to their morphology. The cubic shapes in **5** and the regular needles found in **6** evolved with time into more irregular platelet-like crystallites (Figure 1), suggesting changes in their crystallinity.

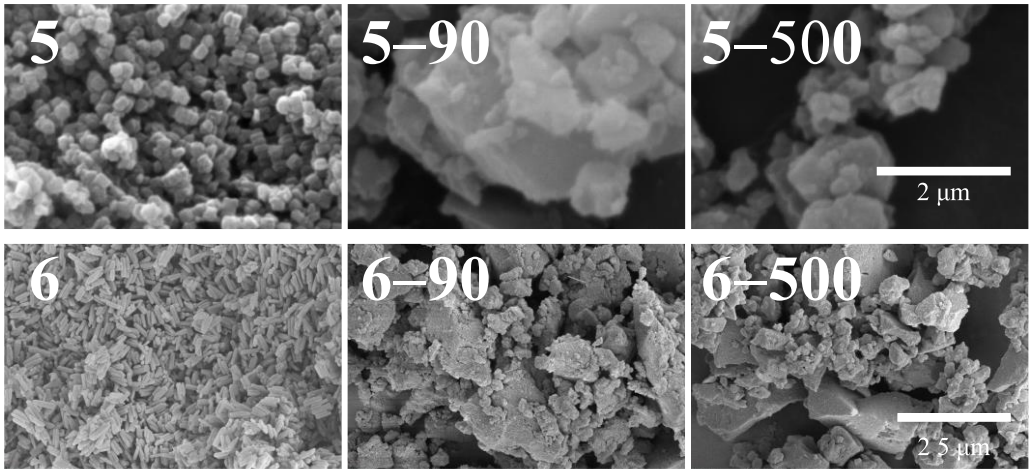

Figure 1. ESEM images of the **5**, **5–90** and **5–500** (top) and **6**, **6–90**, and **6–500** (bottom) to appreciate the disaggregation of the particles (the white bar corresponds to 2 μm for all top images and 2.5 μm for all bottom images).

Powder X-ray diffraction

The crystal structures of **5** in the LS and HS states and of **6** in the LS state have been already reported.[35,37,38] In the case of **6**, due to limitations of the setup, powder diffractogram in the HS state could not be performed. We were able to obtain the diffractogram of **6** at 400 K (Figure S4.2), showing high degree of crystallinity, which was suitable for Rietveld refinement using TOPAS 6.0.[39,40] The crystal structure obtained was similar than the previous reported in the LS state with only differences in the cell parameters due to the increase in the Fe–N distances and a bending in the angle of the amino radical in the triazole ligand (See Supporting Information, Figures S4.2 and S4.3 and Table S4.1).

We studied all samples by PXRD (Figure 2, top). A Pawley refinement was carried out, where we obtained the expected unit cell for $[Fe(trz)(Htrz)_2]_n(BF_4)_n$ (**5**), with space group *Pnma*, a = 17.051 ± 0.010 Å, b = 7.262 ± 0.004 Å, c = 9.240 ± 0.006 Å, in accordance with those reported in the literature; and a space group $P6_3/m$, $a = b$ = 10.071 ± 0.006 Å and c = 7.382 ± 0.004 Å, for $[Fe(NH_2–trz)_2]_n(SO_4)_n$ (**6**).[35,38] No additional peaks were present in the PXRD patterns, indicating the absence of additional crystalline phases.

The powder patterns for all samples are consistent with the same unit cell and space group (Figure S4.4–S4.7). A more accurate fitting was obtained for **6** due to its higher degree in crystallinity. The cell expansion upon the spin transition for **6** was of 33 Å^3, much smaller than the found for **5** (141 Å^3).

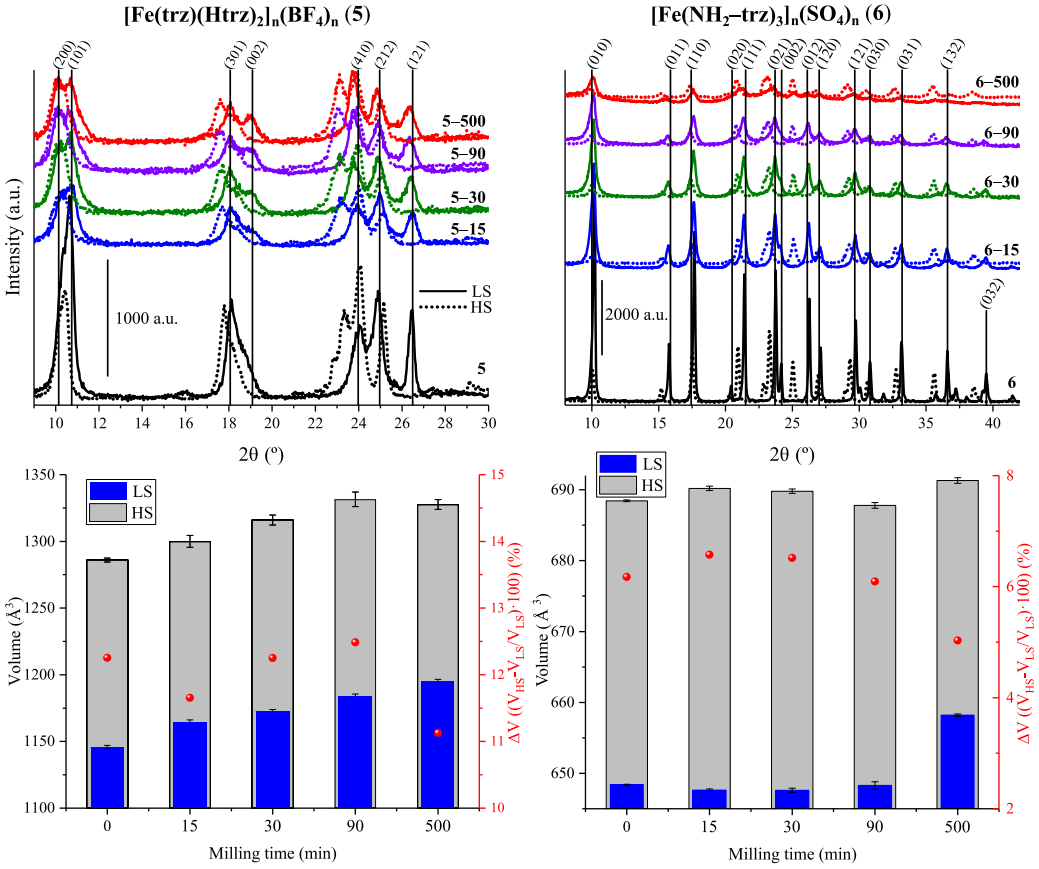

Figure 2. Comparison of the powder X-ray diffraction patterns (λ = 1.5405 Å) for **5**, **6** and their milled samples in LS and HS (top) and evolution of unit cell volumes in LS and HS as a function of milling time (bottom).

As observed in Figure 3, bottom, unit cell volume increases upon long milling time for both HS and LS phases and compounds. In the case of **5**, The HS volume remains essentially constant beyond 90 min milling, while the LS volume keeps increasing. This fact decreases ΔV upon the spin transition, indicating a lesser crystallographic change. The expansion, for the LS samples, accounts for ≈ 4% in cell volume (from 1144 ± 2 to

1194 ± 2 Å^3). Beyond the peak shifts due to the volume changes, their relative intensities are also affected. For instance, the relative intensity for the (002) peak increases with respect to the close-by (301) peak. This suggests that the milling process is actually promoting a chemical reaction through a recrystallization process, modifying their shape and preferential growth directions. Regarding **6**, LS volume was similar for samples milled up to 90 minutes (≈ 647 Å^3) and it raised to 658 Å^3 for **6–500**, whereas the HS volume remained constant (≈ 690 Å^3) in all the samples, meaning a decrease in the relative volume change (ΔV) for long milled samples. During the milling protocol in **6**, a high decrease in crystallinity was observed and some peaks were impossible to detect in the 500 milled sample. However, the relative intensity of the peaks and the 2θ were similar in all the samples, indicating that the crystal structure of **6** presents a higher resistance to mechanical stress than **5**.

Magnetic measurements

Magnetic susceptibility data were collected in the 200−400 K range and corrected (See supporting information and Figure S4.8 and S4.9). Multiple temperature cycles were measured to confirm repeatability. The first two cycles were slightly different, due to initial solvent loss (Figure S4.10 and S4.11). After the third cycle, magnetic data became consistent, confirming a stable phase. For further discussion, we will use data from the fourth cycle in both cases. **5** and **6** showed a spin transition with thermal hysteresis, in good agreement with previous literature results,[35,41] where $T_{1/2}(\uparrow)$ = 380 K and $T_{1/2}(\downarrow)$ = 345 K define a hysteresis loop of ΔT = 35 K for **5** and $T_{1/2}(\uparrow)$ = 349 K and a $T_{1/2}(\downarrow)$ = 329 K a loop of ΔT = 20 K for **6**. Table 1 summarizes the magnetic properties of all the samples.

In the case of **5** (Figure 4, left), after 15 min ball milling, the hysteresis moved to lower temperatures, $T_{1/2}(\uparrow)$ = 368 K and $T_{1/2}(\downarrow)$ = 329 K, becoming slightly wider, ΔT = 39 K. The same trend follows prolonged milling times (Table 2), reaching what appears the limiting case for this method at very long times (≈ 500 min), $T_{1/2}(\uparrow)$ = 350 K and $T_{1/2}(\downarrow)$ = 305 K, ΔT = 45 K. In contrast, 15 and 30 min ball millings of **6** (Figure 3, right) produced a shift of $T_{1/2}(\uparrow)$ to higher temperatures (352 K in the both cases) and a decrease

of $T_{1/2}(\downarrow)$ to 315 and 310 K, respectively, producing a hysteresis loop of approximately 40 K, doubly higher than the original one. Higher millings (90 and 500 minutes) caused a substantial decrease in the transition temperatures, achieving bistability at room temperature.

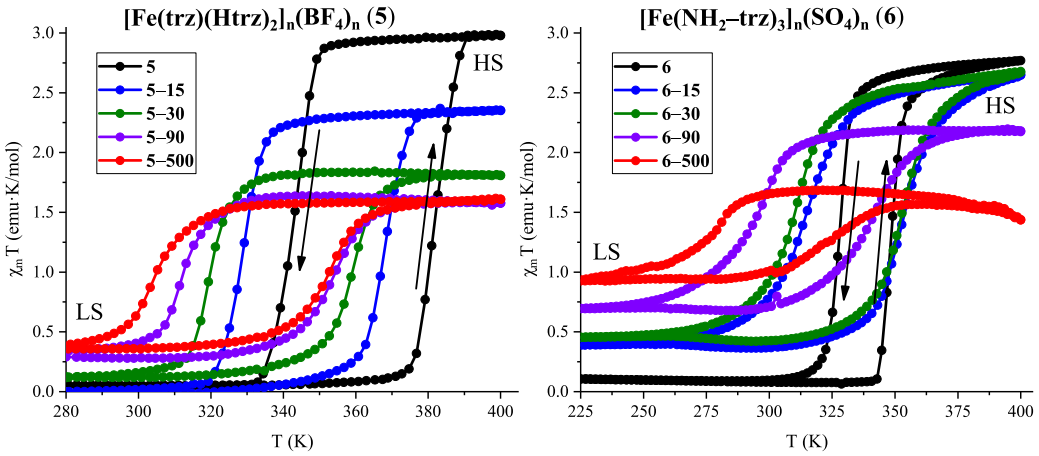

Figure 3. $\chi_m T$ vs T plot of **5** and all its milled samples (left) and **6** and all its milled samples (right) at a scan rate of 2 K/min in the 280−400 K region.

Lower transition temperatures might be related to the unit cell expansion, since larger volumes stabilize the HS excited state. The increment in hysteresis width is typically associated to bulk cooperativity, suggesting increased cooperativity upon milling. However, the smoothness of the transition, given from the difference in temperatures for which 80% and 20% of the spin centres lay in the HS state, increased from 5 to 17 K in **5** and **5–500** respectively, and from 8 to 33 K in **6** and **6–500**,[26,42] what suggests a decrease in cooperativity, making these two observations counterintuitive. The Slichter-Drickmaker model (see Supporting Information),[43,44] was employed to model the hysteretic behaviour and to estimate cooperativity (Γ) from the HS fraction (γ_{HS}) and the corresponding DSC data (Figure S4.12 and S4.13 and Table S4.2 and S4.3). With this model, Γ decreases upon milling time (Figure S4.11 and S4.12) from 8.8 ± 0.9 (**5**) to 6.9 ± 0.3 kJ/mol (**5–500**) and from 6.9 ± 0.5 (**6**) to 6.1 ± 0.3 kJ/mol (**6–500**).

Another important effect upon milling comes from the fraction of the material involved in the SCO process, determined by the $\chi_m T$ values. From a quantitative transition for **5**

($\chi_m T$ (280 K) = 0.05 emu·K/mol and $\chi_m T$ (400 K) = 2.98 emu·K/mol), the $\chi_m T$ at 280 K increases monotonically up to 0.39 emu·K/mol and decreases down to 1.61 emu·K/mol at 400 K in **5–500**. The same trend is observed in **6**, $\chi_m T$ changes from 0.11 to 0.93 emu·K/mol at 280 K and from 2.77 to 1.45 emu·K/mol at 400 K for **6** and **6–500**, respectively. This can be assigned to the recrystallization process that also provokes a partial decomposition of the product to a non-SCO amorphous phase (nondetectable by PXRD).

Table 1. Physical characterization of the terminal spin transition **5**, **6** and its batches obtained as a function of milling time.

$[Fe(trz)(Htrz)_2]_n(BF_4)_n$ (**5**)

	$T_{1/2}(\uparrow)$ [K]	$T_{1/2}(\downarrow)$ [K]	ΔT [K]	χT_m(280 K) [K]	χT_m(400 K) [K]	Smoothness [K]	Γ [kJ·mol^{-1}]
5	380	345	35	0.05	2.98	5	8.8 ± 0.9
5–15	368	329	39	0.01	2.35	9	7.9 ± 0.8
5–30	359	320	39	0.12	1.81	11	7.5 ± 0.8
5–90	354	312	42	0.34	1.58	15	7.3 ± 0.4
5–500	352	305	47	0.39	1.61	16	6.9 ± 0.3

$[Fe(NH_2\text{–}trz)_2]_n(SO_4)_n$ (**6**)

	$T_{1/2}(\uparrow)$ [K]	$T_{1/2}(\downarrow)$ [K]	ΔT [K]	χT_m(225 K) [K]	χT_m(400 K) [K]	Smoothness [K]	Γ [kJ·mol^{-1}]
6	349	329	20	0.11	2.77	6	6.9 ± 0.5
6–15	352	315	37	0.9	2.65	21	6.7 ± 0.4
6–30	352	310	42	0.45	2.67	19	6.6 ± 0.3
6–90	340	295	45	0.69	2.18	27	6.3 ± 0.4
6–500	326	279	47	0.93	1.45	34	6.1 ± 0.3

Crystallographic Phase Transitions

We studied the temperature dependence of the powder X-ray diffraction patterns. Figures 4, top and S4.14 show the PXRD patterns in the 300−400 K range of **5**, with a scan rate of 5 K min^{-1}. An abrupt, reversible change in the position of all the diffraction peaks toward lower angles was detected, indicating an abrupt expansion in the unit cell. This process also shows thermal hysteresis. The faster scan rate in these measurements makes the hysteresis cycles to appear slightly wider, but in good agreement with the thermal magnetic hysteresis (Table 1).

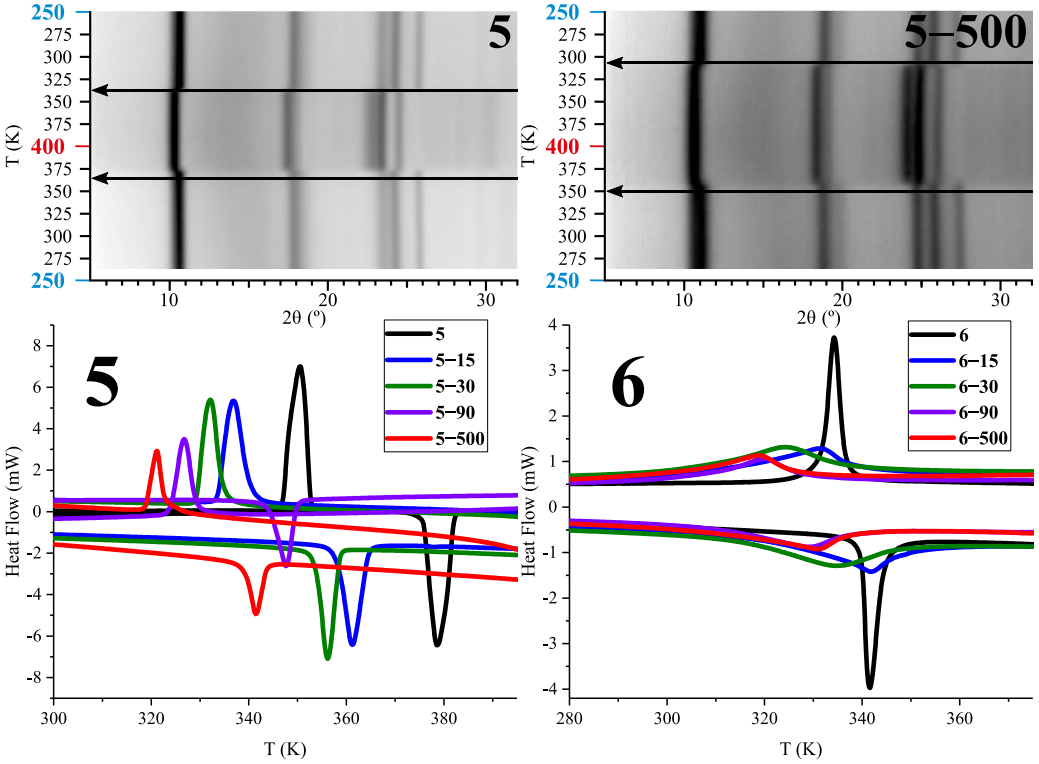

Figure 4. PXRD patterns during spin crossover transition between 300 and 400 for samples **5** and **5–500** (top) and DSC cycles in the range from 280 to 400 K (Scan rate 2 K/min) for **5**, **6** and all the milled samples (bottom).

We also performed calorimetry measurements in the two compounds to further investigate the nature of these crystallographic transitions (Figure 4, bottom). Well-defined DSC peaks appear in the thermal cycles, endothermic for the LS→HS transition, during the heating branch, and exothermic for the HS→LS transition, during the cooling branch, confirming the appearance of a true crystallographic phase transition associated to the SCO phenomena. Again, transition temperatures are in good agreement with magnetic and crystallographic measurements. The estimated enthalpy contributions, ΔH (Table S4.2 and S4.3), decreased for longer milling times, more abruptly in sample **8**, which is in good agreement with the lesser volume change as described previously.

Conclusions

We have found that spin crossover phenomena of the 1D $[Fe(trz)(Htrz)_2]_n(BF_4)_n$ (**5**) and $[Fe(NH_2{-}trz)_3]_n(SO_4)_n$ (**6**) can be modified by grinding the compounds via ball milling. The milling decreases particle size and generate defects in the structure, but more importantly, it induces a recrystallization process that yields a slightly expanded unit cell, as monitored by PXRD. This recrystallization may follow a solid-to-solid transformation or a dissolution/recrystallization process with the help of crystallographic solvent molecules. Beyond its origin, it modifies the SCO thermal hysteresis, lowering the transition temperatures, while widening the hysteresis width. The latter is unprecedented when decreasing the particle size. Indeed, these results differ from nanoparticles of the same material obtained in liquid phase and with the help of surfactants, which showed no distinct magnetic behaviour from bulk down to 10 nm. This supports again that the magnetic behaviour we observe after grinding is due to a recrystallization process, and not just to particle size differences. Furthermore, the bistability parameters can be tuned by ball milling time, while maintaining bulk-like properties, as confirmed by the crystallographic transition monitored by PXRD and DSC. This simple processing technique has allowed us to bring close to room temperature the memory effect in $[Fe(trz)(Htrz)_2]_n(BF_4)_n$ and $[Fe(NH_2{-}trz)_3]_n(SO_4)_n$, as representative materials. Our finding adds additional tools to fine-tune the properties of these materials toward applications.

References

[1] J. P. martin, J. Zarembowitch, A. Bousseksou, A. Dworkin, J. G. Haasnoot, F. Varret, *Inorg. Chem.* **1994**, 33, 6325

[2] T. Tayagaki, A. Galet, G. Molnár, M. C. Muñoz, A. Zwick, K. Tanaka, J. A. Real, A. Bousseksou, J. Phys. Chem. B **2005**, 109, 14859.

[3] S. Zheng, M. A, Siegler, J. S. Costa, W. T. Fu, S. Bonnet, *Eur. J. Inorg. Chem.* **2013**, 1033

[4] I. Krivokapic, P. Chakraborty, C. Enachescu, R. Bronisz, A. Hauser, *Inorg. Chem.* **2011**, 50, 1856

[5] M. Sorai, J. Ensling, P. Gütlich, *Chem. Phys.* **1976**, 18, 199

[6] J. R. Galán-Mascarós, E. Coronado, A. Forment-Aliaga, M. Monrabal-Capilla, E. Pinilla-Cienfuegos, M. Ceolin, *Inorg. Chem.* **2010**, 49, 5706.

[7] I. A. Gural'Skiy, G. Molnár, I. O. Fritsky, L. Salmon, A. Bousseksou, *Polyhedron* **2012**, 38, 245

[8] F. J. Valverde-Muñoz, A. B. Gaspar, S. I. Shylin, V. Ksenofontov, J. A. Real, *Inorg Chem.* **2015**, 54, 7906.

[9] L. Salmon, L. Catala, *C. R. Chim.* **2018**, 21, 1230.

[10] C. Bartual-Murgui, E. Natividad, O. Roubeau, *J. Mater. Chem. C* **2015**, 3, 7916.

[11] M. Giménez-Marqués, M. L. García-Sanz De Larrea, E. Coronado, *J. Mater. Chem. C* **2015**, 3, 7946.

[12] T. Delgado, C. Enachescu, A. Tissot, A. Hauser, L. Guénée, C. Besnard, *J. Mater. Chem. C* **2018**, 6, 12698.

[13] C. Enachescu, M. Nishino, S. Miyashita, A. Hauser, A. Stancu, L. Stoleriu, *EPL* **2010**, 91, 27003.

[14] L. Moulet, N. Daro, C. Etrillard, J. F. Létard, A. Grosjean, P. Guionneau, *Magnetochemistry* **2016**, 2, 10.

[15] A. B. Gaspar, G. Molnár, A. Rotaru, H. J. Shepherd, Comptes Rendus Chim. 2018, 21, 1095.

[16] Y. Garcia, V. Ksenofontov, P. Gütlich, *Hyperfine Interact.* **2002**, 139, 543.

[17] P. Gütlich, V. Ksenofontov, A. B. Gaspar, *Coord. Chem. Rev.* **2005**, 249, 1811.

[18] J. Linares, E. Codjovi, Y. Garcia, *Sensors* **2012**, 12, 4479.

[19] A. Suzuki, M. Fujiwara, M. Nishijima, *Colloid Polym. Sci.* **2008**, 286, 525.

[20] C. Faulmann, J. Chahine, I. Malfant, D. de Caro, B. Cormary, L. Valade, *Dalt. Trans.* **2011**, 40, 2480.

[21] M. S. Haddad, W. D. Federer, M. W. Lynch, D. N. Hendrickson, *J. Am. Chem. Soc.* **1980**, 102, 1468.

[22] M. Sorai, R. Burriel, E. F. Westrum, D. N. Hendrickson, *J. Phys. Chem. B* **2008**, 112, 4344.

[23] M. S. Haddad, W. D. Federer, M. W. Lynch, D. N. Hendrickson, *Inorg. Chem.* **1981**, 20, 131.

[24] W. D. Federer, D. N. Hendrickson, *Inorg. Chem.* **1984**, 23, 3870.

[25] T. F. Grigorieva, A. P. Barinova, N. Z. Lyakhov, *J. Nanoparticle Res.* **2003**, 5, 439.

[26] J. H. Askew, H. J. Shepherd, *Chem. Commun.* **2017**, 54, 180.

[27] J. H. Askew, H. J. Shepherd, *Dalt. Trans.* **2020**, 49, 2966.

[28] A. Nasser, U. Mingelgrin, *Appl. Clay Sci.* **2012**, 67–68, 141.

[29] G. E. Christidis, P. Makri, V. Perdikatsis, *Clay Miner.* **2004**, 39, 163

[30] A. Moballegh, H. R. Shahverdi, R. Aghababazadeh, A. R. Mirhabibi, *Surf. Sci.* **2007**, 601, 2850.

[31] N. S. Sabri, M. S. M. Deni, A. Zakaria, M. K. Talari, *Phys. Procedia* **2012**, 25, 233.

[32] A. A. Al-Ghamdi, F. S. Al-Hazmi, L. S. Memesh, F. S. Shokr, L. M. Bronstein, *Ceram. Int.* **2017**, 43, 6192.

[33] T. Friščić, *Chem. Soc. Rev.* **2012**, 41, 3493.

[34] S. L. James, C. J. Adams, C. Bolm, D. Braga, P. Collier, T. Friščić, F. Grepioni, K. D. M. Harris, G. Hyett, W. Jones, A. Krebs, J. Mack, L. Maini, A. G. Orpen, I. P. Parkin, W. C. Shearouse, J. W. Steed, D. C. Waddell, *Chem. Soc. Rev.* **2012**, 41, 413.

[35] V. Y. Sirenko, O. I. Kucheriv, A. Rotaru, I. O. Fritsky, I. A. Gural'skiy, *Eur. J. Inorg. Chem.* **2020**, 48, 4523.

[36] J. Kroeber, J. P. Audiere, R. Claude, E. Codjovi, O. Kahn, J. G. Haasnoot, F. Groliere, C. Jay, A. Bousseksou, *Chem. Mater.* **1994**, 6, 1404.

[37] A. Urakawa, W. Van Beek, M. Monrabal-Capilla, J. R. Galán-Mascarós, L. Palin, M. Milanesio, *J. Phys. Chem. C* **2011**, 115, 1323.

[38] A. Grosjean, P. Négrier, P. Bordet, C. Etrillard, D. Mondieig, S. Péchev, E. Lebraud, J. F. Létard, P. Guionneau, *Eur. J. Inorg. Chem.* **2013**, 2, 796.

[39] H. M. Rietveld, *Acta Cryst.* **1967**, 22, 151.

[40] P. Scardi, L. A. Ricardo, C. Perez-Demydenko, A. A. Coelho, *J. Appl. Cryst.* **2018**, 51.

[41] K. Sugiyarto, H. Goodwin, *Aust. J. Chem.* **1994**, 47, 263.

[42] P. Gütlich, H. A. Goodwin, *Spin Crossover in Transition Metal Compounds II*, Springer-Verlag Berlin Heidelberg, **2004**.

[43] C. P. Slighter, H. G. Drickamer, *J. Chem. Phys.* **1972**, 56, 2142.

[44] R. Kulmaczewski, J. Olguín, J. A. Kitchen, H. L. C. Feltham, G. N. L. Jameson, J. L. Tallon, S. Brooker, *J. Am. Chem. Soc.* **2014**, 136, 878

Supporting Information of Chapter 4.

Effect of Mechanochemical Recrystallization on the Thermal Hysteresis of 1D Fe(II)–triazole Spin Crossover Polymers

Morphology studies

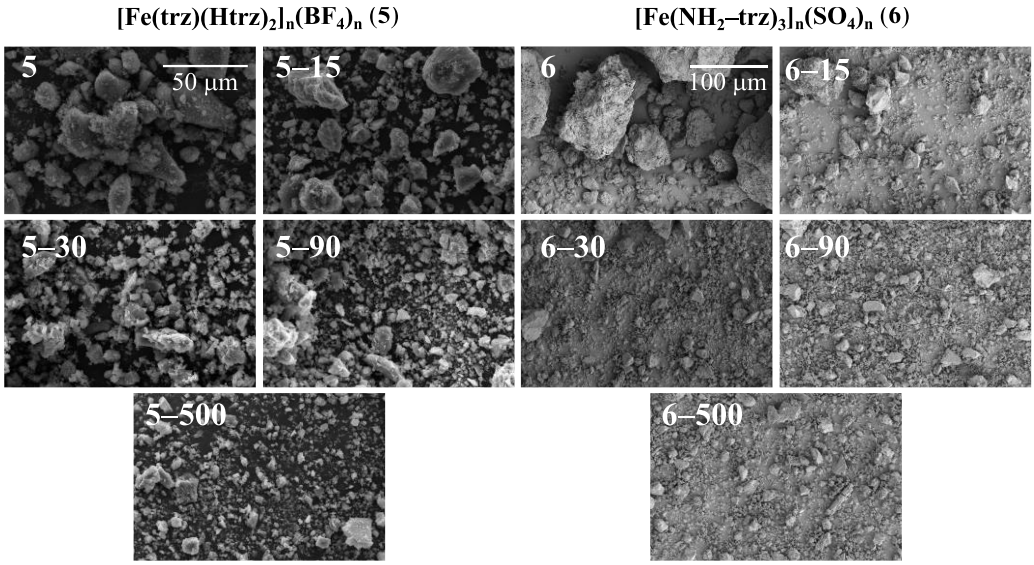

Figure S4.1. ESEM images of all the samples.

Crystal Structure of [Fe(NH$_2$trz–trz)$_3$]$_n$(SO$_4$)$_n$ in HS

The crystal structure of [Fe(NH$_2$–trz)$_3$]$_n$(SO$_4$)$_n$ (**6**) in the LS state was reported with a *P6$_3$/m* space group with two formula units per cell. We were able to obtain the PXRD diffractogram of **6** at 400 K (HS state). The PXRD analysis was performed from 8 to 72º *2θ* with a step size of 0.03º with different acquisition times (for 8–70º at 12s, for 40–52º at 24s and for 52–72º at 30s) in order to enhance the peak/noise ratio. The three patterns were refined simultaneously, TOPAS 6.0 based on the Rietveld method,[38,39] with the *P6$_3$/m* space group. Figure S4.3 shows the coordination network where Fe(II) centers are connected by 4–NH$_2$–1,2,4–triazole molecules, creating a polymer chain. The sulfate counteranions are disordered between two positions in the interspace among the polymer chains. The main differences with the structure in the LS state are a higher cell volume due to the population of the Fe(II) e_g orbitals that have an antibonding character and interact with nitrogen orbitals, and a bending in the angle of the 4–NH$_2$–1,2,4–triazole amino radical.

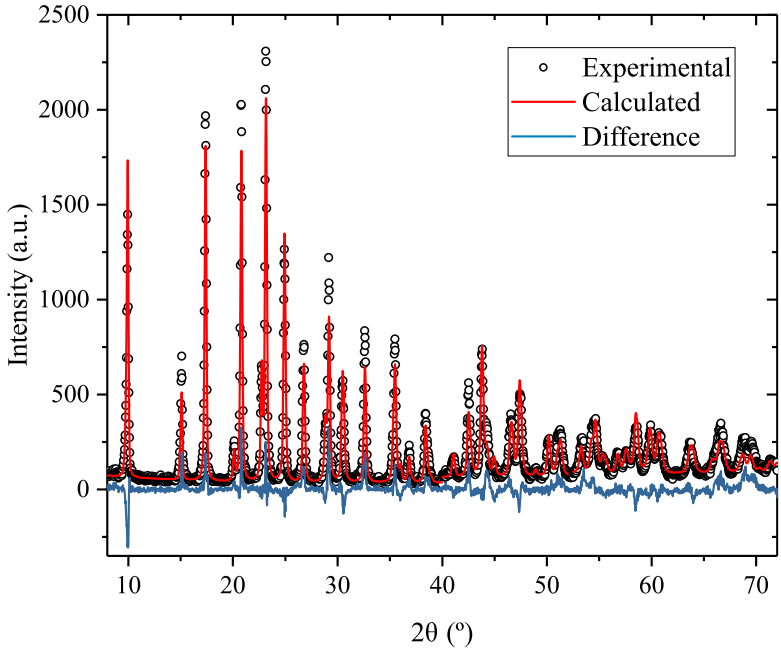

Figure S4.2. Experimental (black circles) and calculated (red line) diffraction patterns of **6** in the HS state. The difference pattern divided by signal to noise ratio is shown as a blue line.

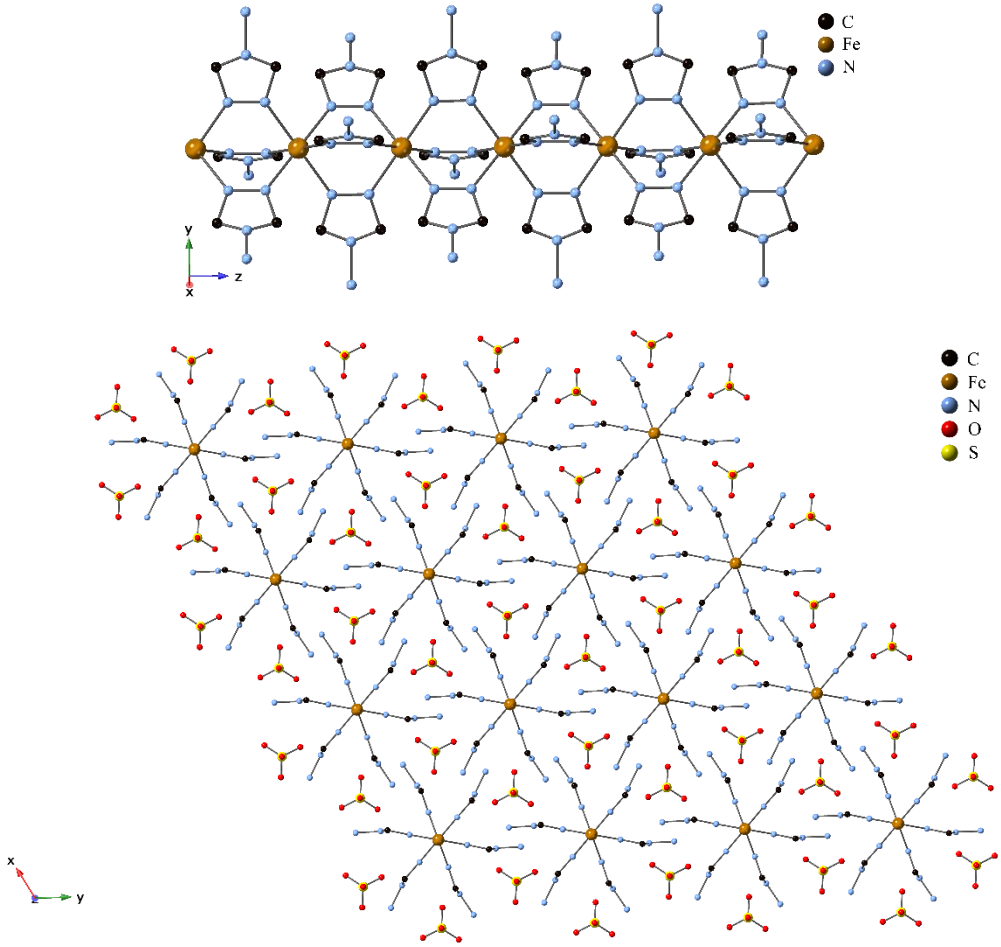

Figure S4.3. Crystal structure of $[Fe(NH_2{-}trz)_3]_n(SO_4)_n$ (**6**) in the HS state along the z axis (top) and crystal packing of the polymer chains along the y axis (bottom).

Table S4.1. Crystal unit cell and Rietveld refinement data obtained for **6** in HS.

Temperature	400 K	*Z*	2
Crystal system	Hexagonal	2θ Angular range [º]	8–72
Space group	*P6₃/m*	R_{wp}	15.68
Cell parameters	$a = b$ = 10.1196(6) c = 7.7716(6) $\alpha = \beta$ = 90º γ =120 º	R_p	12.68
		Density (calculated) [g/cm^3]	
		Volume [Å^3]	689.23(10)

Pawley refinements

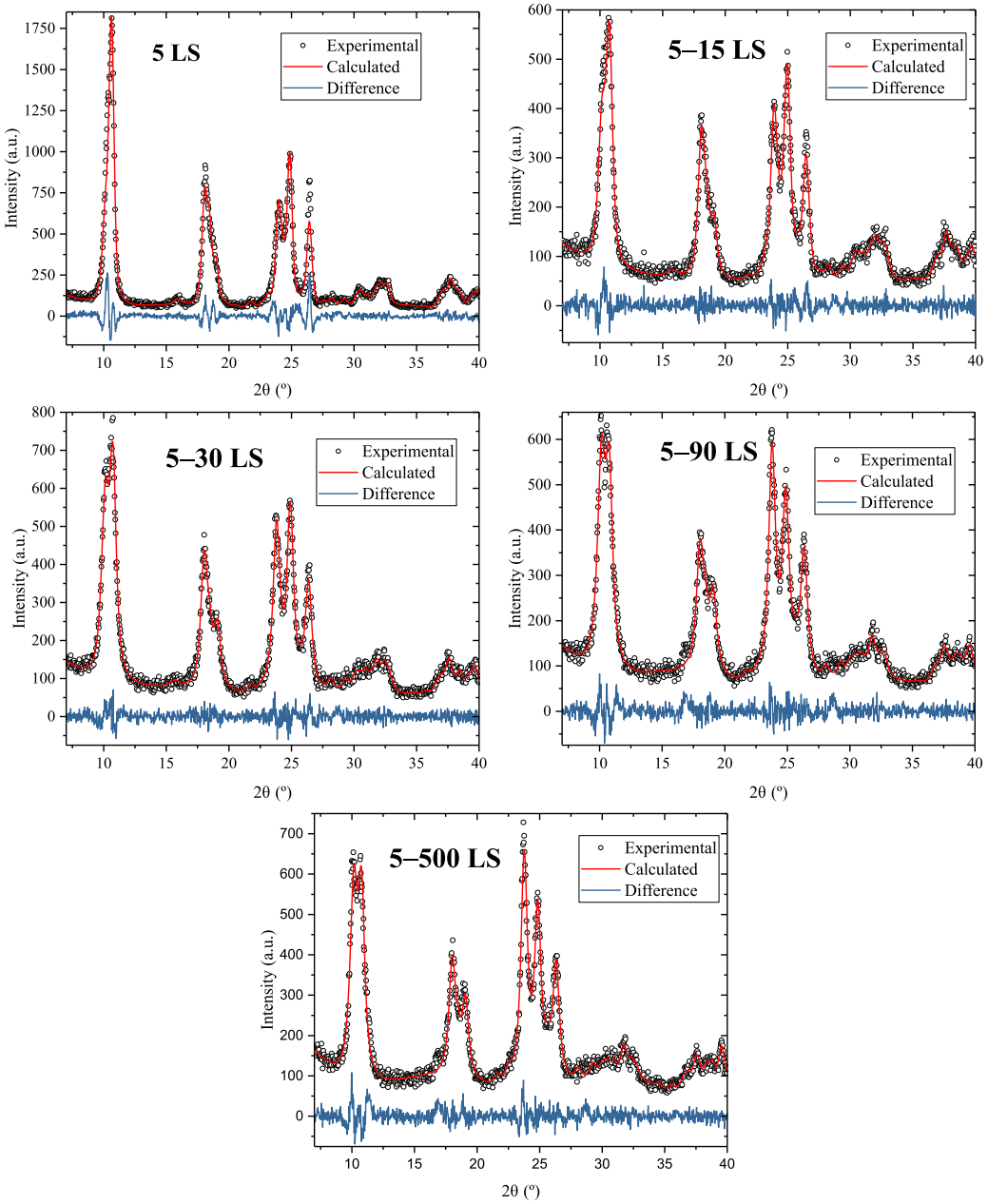

Figure S4.4. Pawley refinement plot of X-ray Diffraction data of **5** and its milled samples in LS.

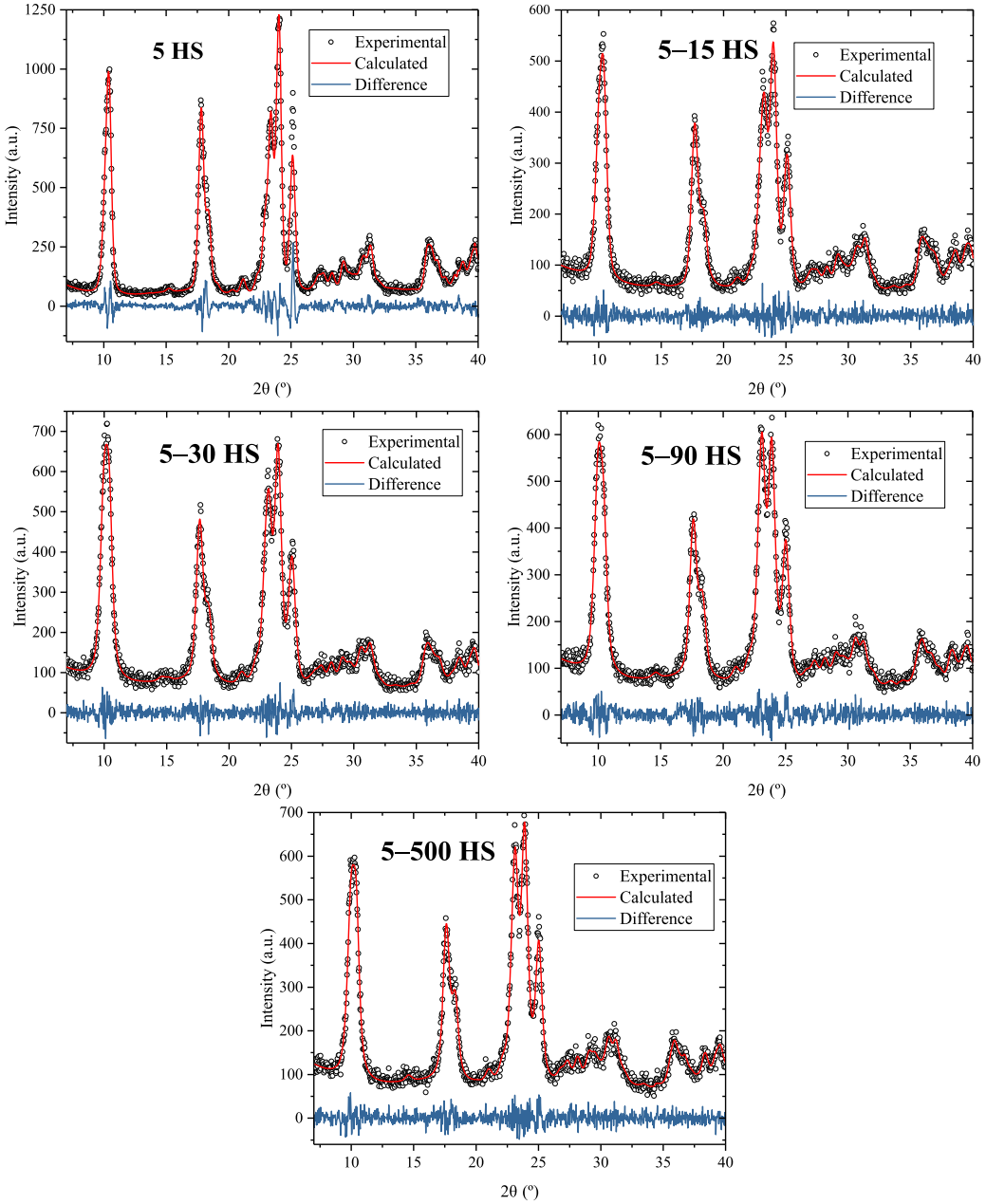

Figure S4.5. Pawley refinement plot of X-ray Diffraction data of **5** and its milled samples in HS.

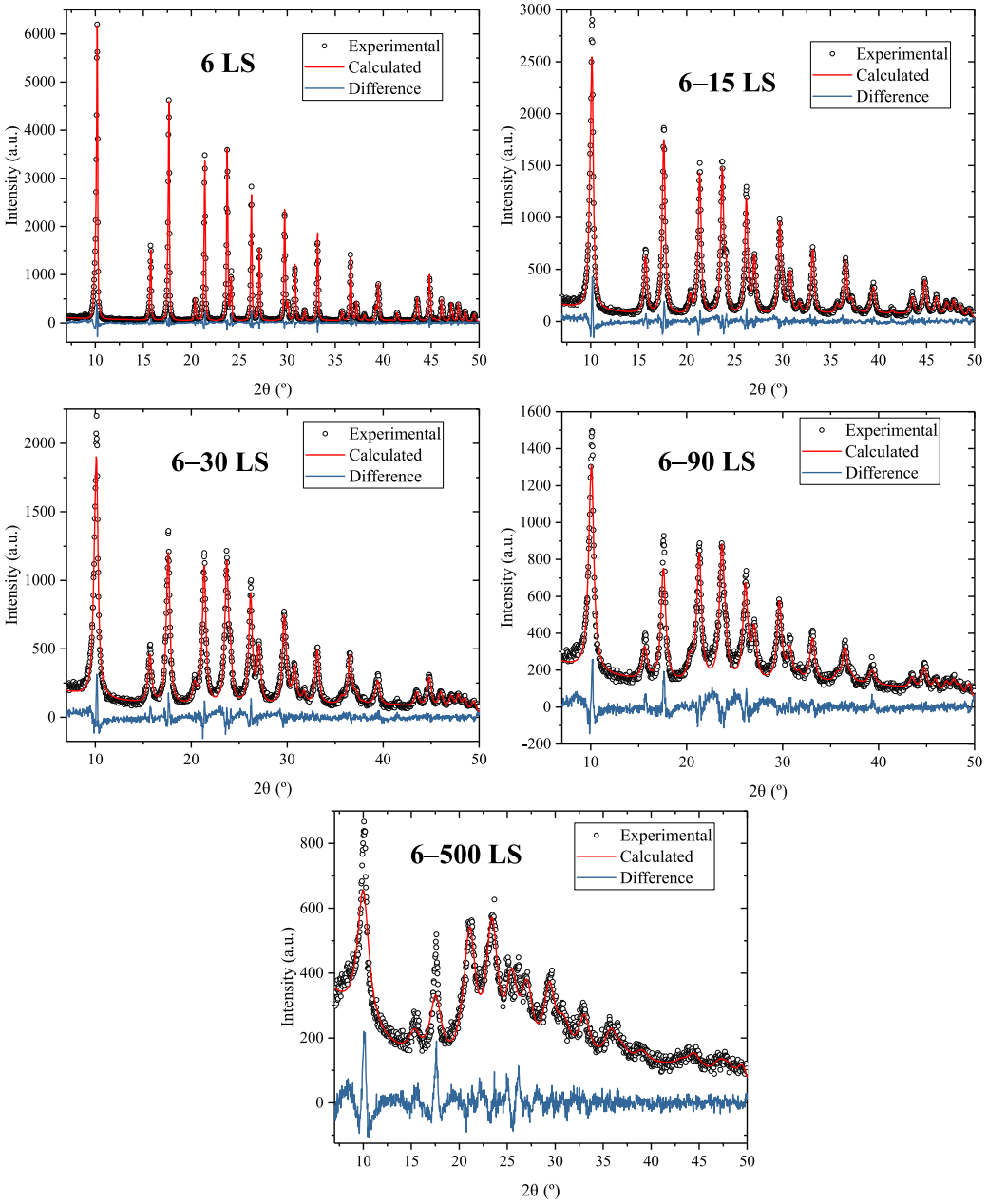

Figure S4.6. Pawley refinement plot of X-ray Diffraction data of **6** and its milled samples in LS.

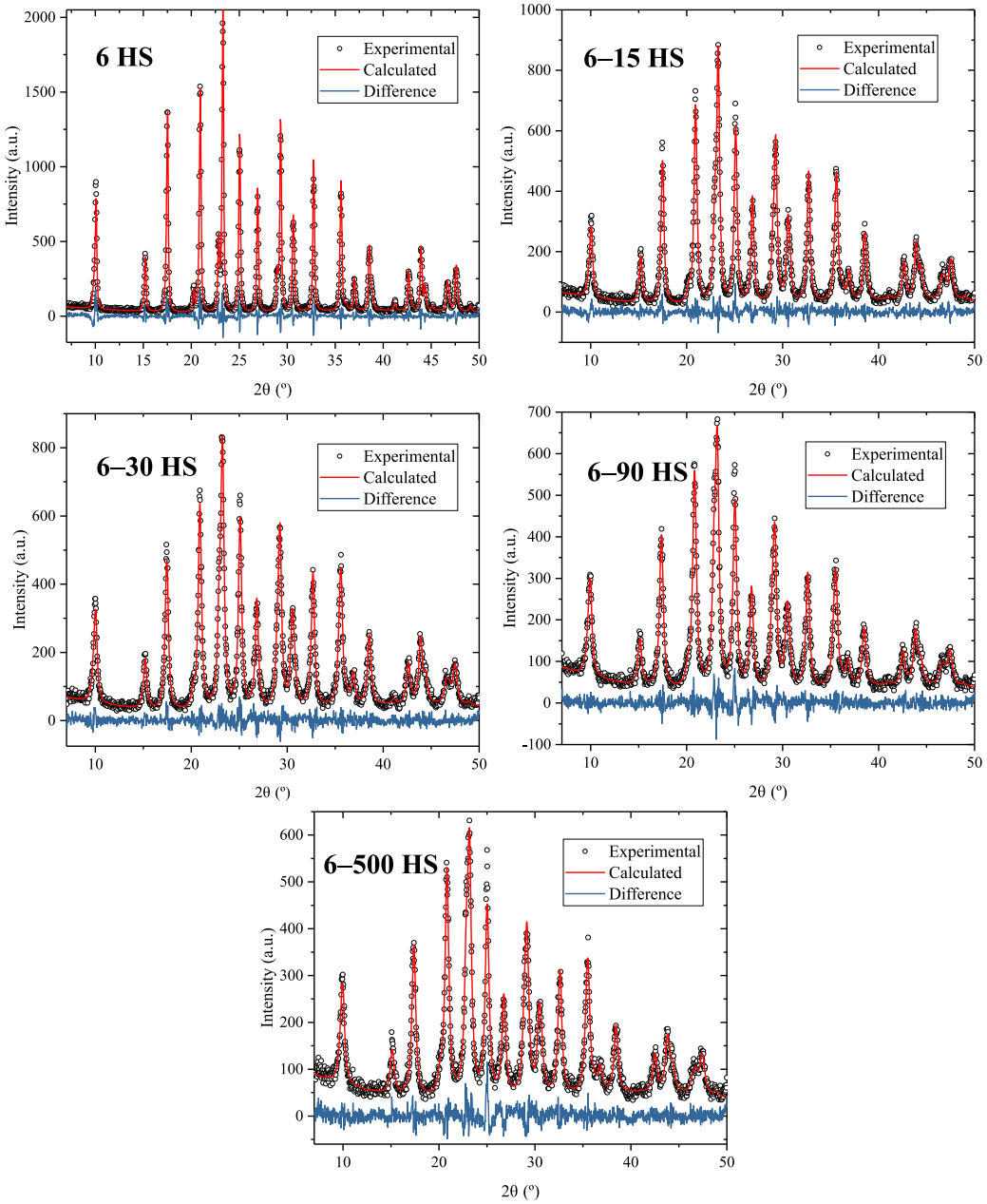

Figure S4.7. Pawley refinement plot of X-ray Diffraction data of **6** and its milled samples in HS.

Temperature-independent residual paramagnetism corrections

The residual paramagnetism correcitons were performed with the Curie-Weiss law (See Annex I).

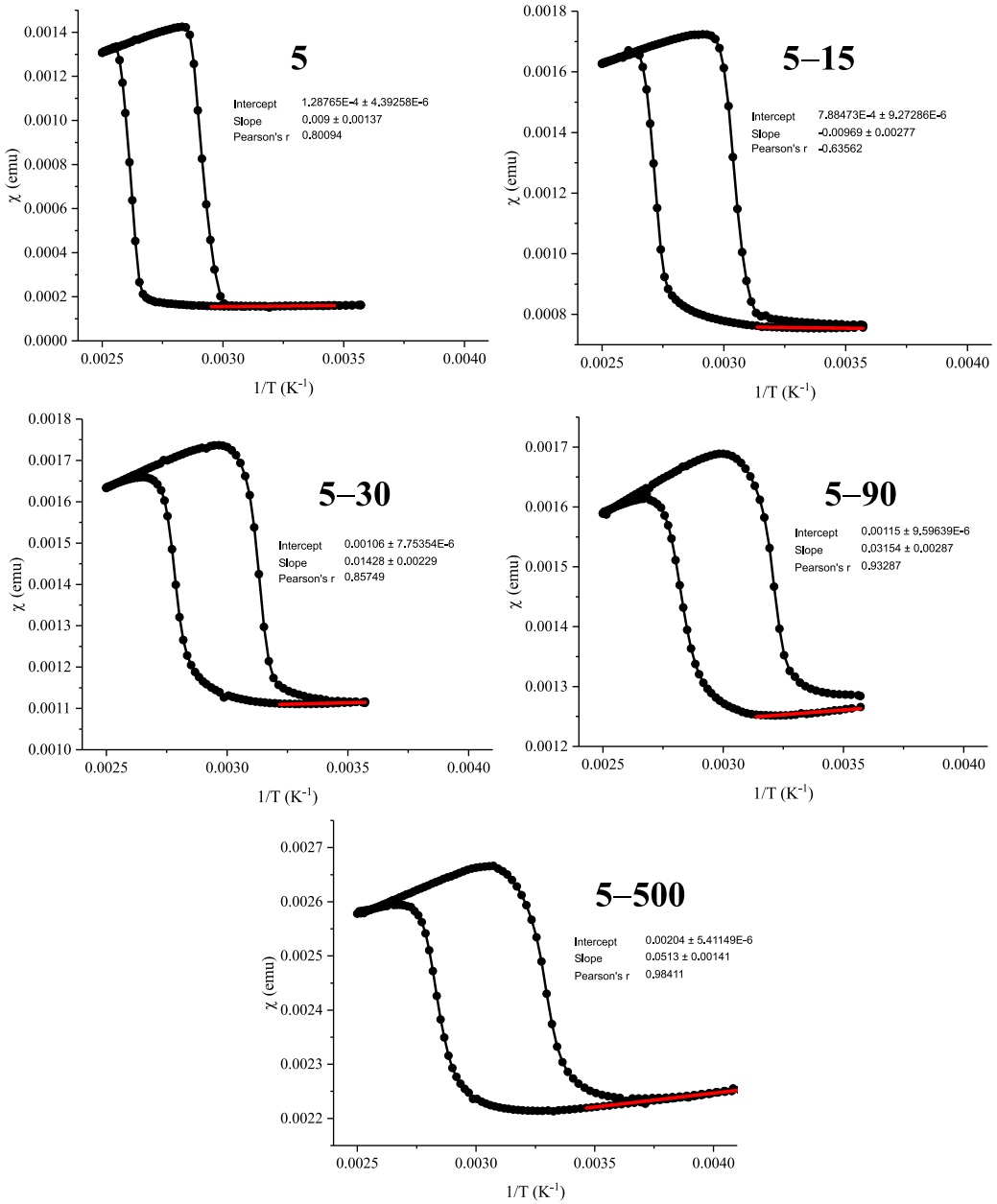

Figure S4.8. χ vs *1/T* of the last cycle and the residual temperature-independent paramagnetism correction (red line) of **5** and its milled samples.

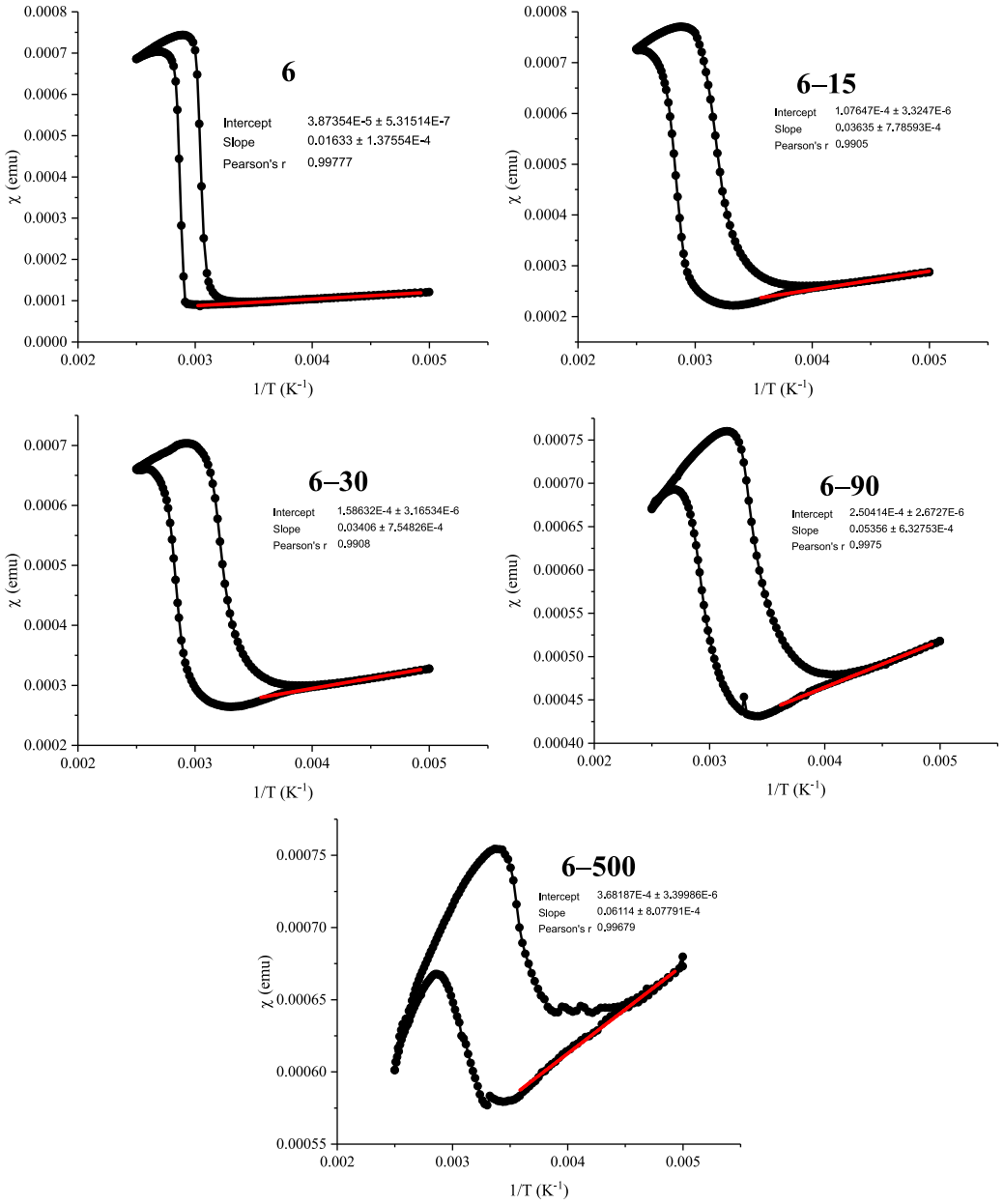

Figure S4.9. χ vs *1/T* of the last cycle and the residual temperature-independent paramagnetism correction (red line) of **6** and its milled samples.

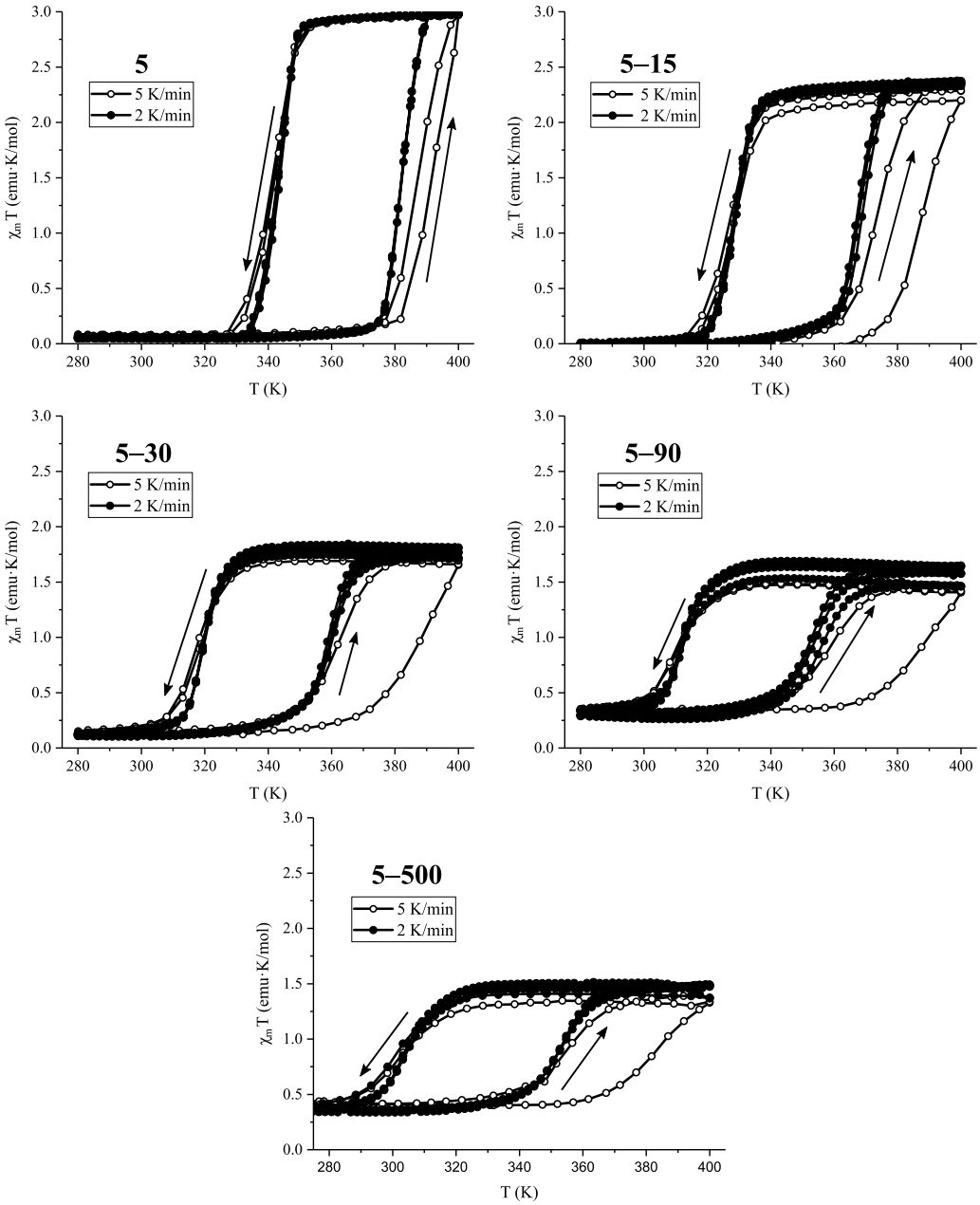

Figure S4.10. $\chi_m T$ vs T cycles of **5** and its milled samples in the 275–400 K region (first two cycles were performed at 5 K/min and the rest at 2 K/min).

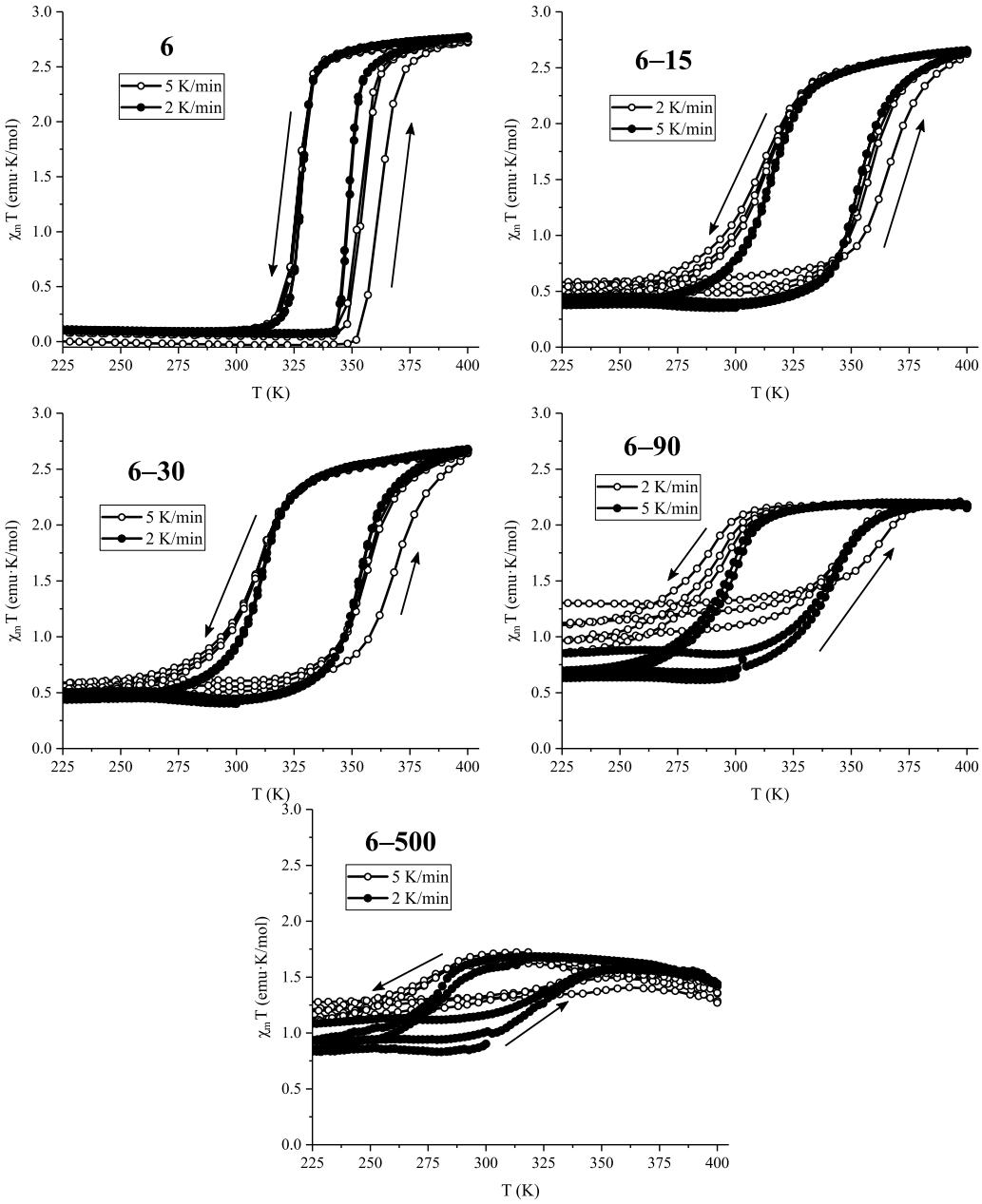

Figure S4.11. $\chi_m T$ vs T cycles of **6** and its milled samples in the 225–400 K region (first two cycles were performed at 5 K/min and the rest at 2 K/min).

Slichter and Drickamer model

This model is based on the assumption that HS and LS states are statistically distributed and form regular solutions. At equilibrium, this model leads to the equation S4.1:

$$ln\left(\frac{1-\gamma_{HS}}{\gamma_{HS}}\right)=\frac{\Delta H+\Gamma(1-2\gamma_{HS})}{RT}-\frac{\Delta S}{R} \qquad \text{Equation S4.1}$$

Where:

$$\boldsymbol{\gamma_{HS}}=\frac{\chi T-\chi T_{LS}}{\chi T_{HS}-\chi T_{LS}} \qquad \boldsymbol{\Delta H}=\frac{|\Delta H\uparrow|+|\Delta H\downarrow|}{2} \qquad \boldsymbol{\Delta S}=\frac{\Delta H}{T_c};\ T_c=\frac{T_{1/2}\uparrow+T_{1/2}\downarrow}{2}$$

Γ, is the mean field interaction parameter that measures the cooperatitivy. If $\Gamma>2RT_c$, the transition occurs with hysteresis, when $\Gamma<2RT_c$, the transition is gradual and if $\Gamma=2RT_c$, the transition is abrupt without hysteresis.

Equation S4.1 was converted into equation S4.2 for an effective fitting.

$$T=\frac{\Delta H+(1-2\gamma_{HS})\Gamma}{S+Rln(\frac{1-\gamma_{HS}}{\gamma_{HS}})} \qquad \text{Equation S4.2}$$

Γ was determined with equation S4.2 and with the experimental values of γ_{HS} vs T (figure S4.12 and S4.13).

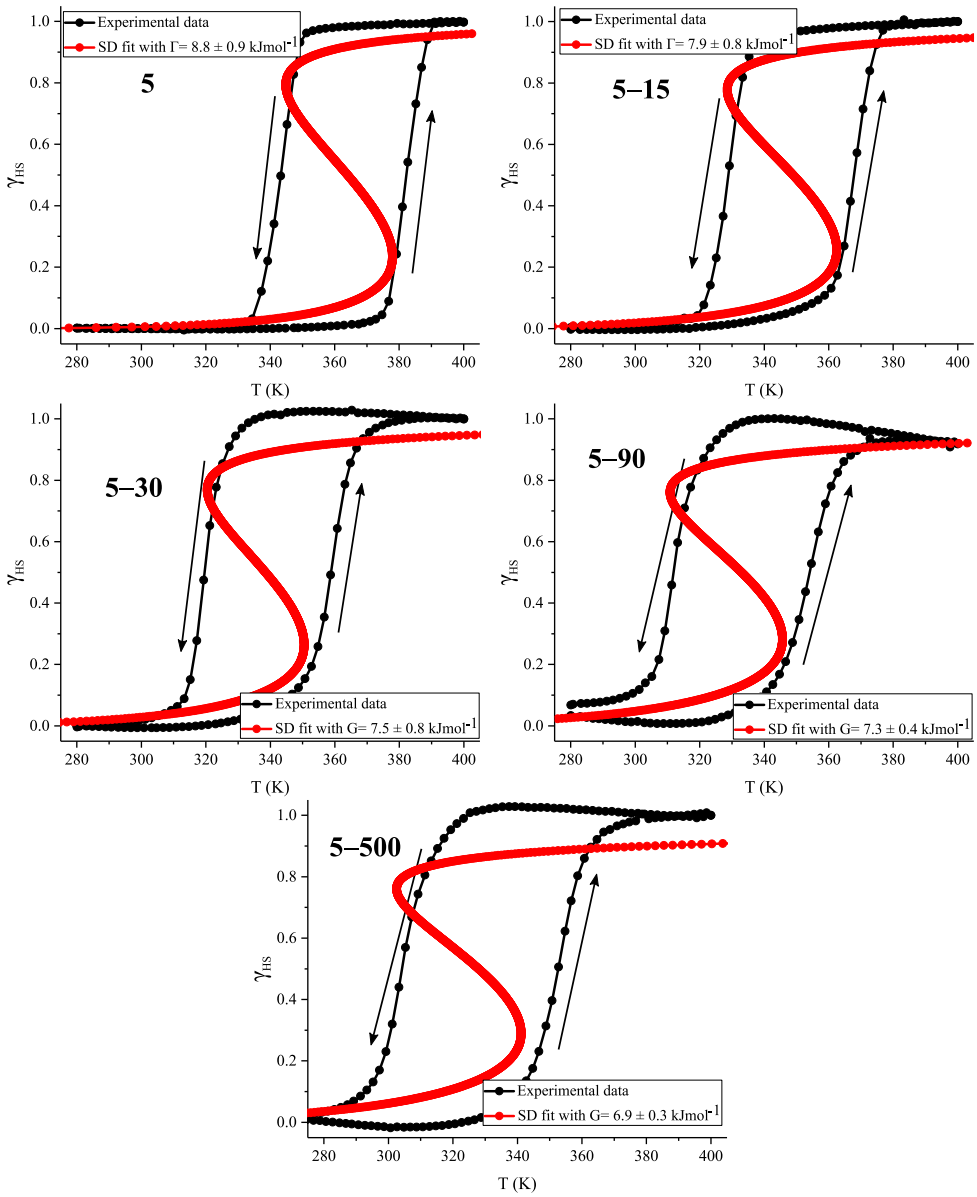

Figure S4.12. Slichter Drickamer fittings of **5** and its milled samples.

Table S4.2 parameters for the Slichter and Drickamer modelling of **5**.

Sample	$T_{1/2}(\uparrow)$ [K]	$T_{1/2}(\downarrow)$ [K]	T_c [K]	ΔH[kJ mol^{-1}]	ΔS [kJ K^{-1} mol^{-1}]	Γ [kJ mol^{-1}]
5	380	345	362.5	24.1	0.066	8.8 ± 0.9
5–15	368	329	348.5	16.5	0.047	7.9 ± 0.8
5–30	359	320	339.5	15.5	0.046	7.5 ± 0.8
5–90	354	312	333	10.7	0.032	7.3 ± 0.4
5–500	352	305	328.5	8.9	0.027	6.9 ± 0.3

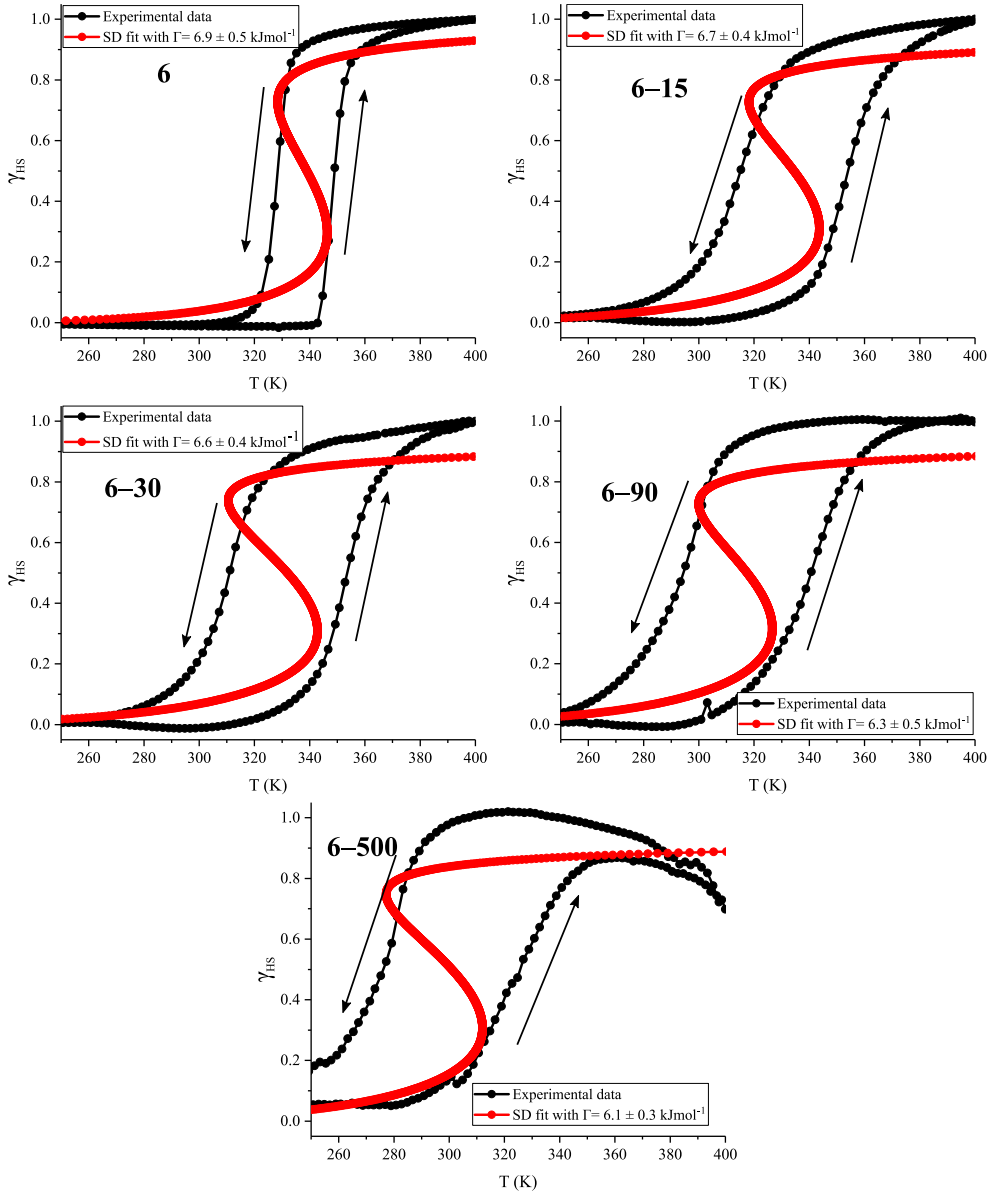

Figure S4.13. Slichter Drickamer fittings of **6** and its milled samples.

Table S4.3 parameters for the Slichter and Drickamer modelling of **6**.

Sample	$T_{1/2}(\uparrow)$ [K]	$T_{1/2}(\downarrow)$ [K]	T_c [K]	ΔH[kJ mol^{-1}]	ΔS [kJ K^{-1} mol^{-1}]	Γ [kJ mol^{-1}]
6	349	329	339	14.70	0.044	6.9 ± 0.5
6–15	352	315	334.5	8.99	0.027	6.7 ± 0.4
6–30	352	310	331	7.84	0.024	6.6 ± 0.4
6–90	340	295	317.5	7.41	0.023	6.3 ± 0.5
6–500	326	279	301	6.56	0.022	6.1 ± 0.3

Crystallographic Phase Transitions

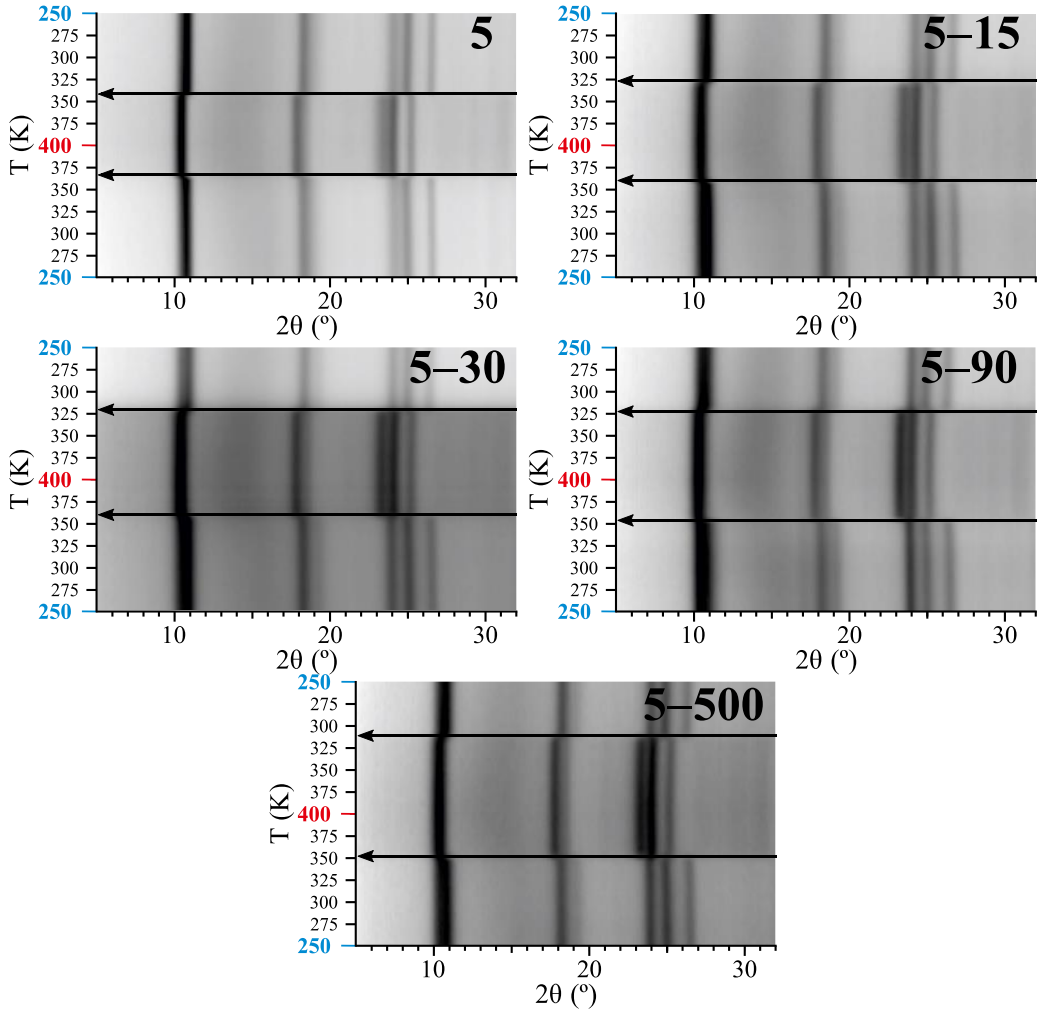

Figure S4.14. PXRD patterns during spin crossover transition between 300 and 400 K for **5** and its milled samples.

Chapter 5. Mechanochemical Processing of Highly Conducting Organic/Inorganic Composites Exhibiting Spin Crossover–Induced Memory Effect in Their Transport Properties

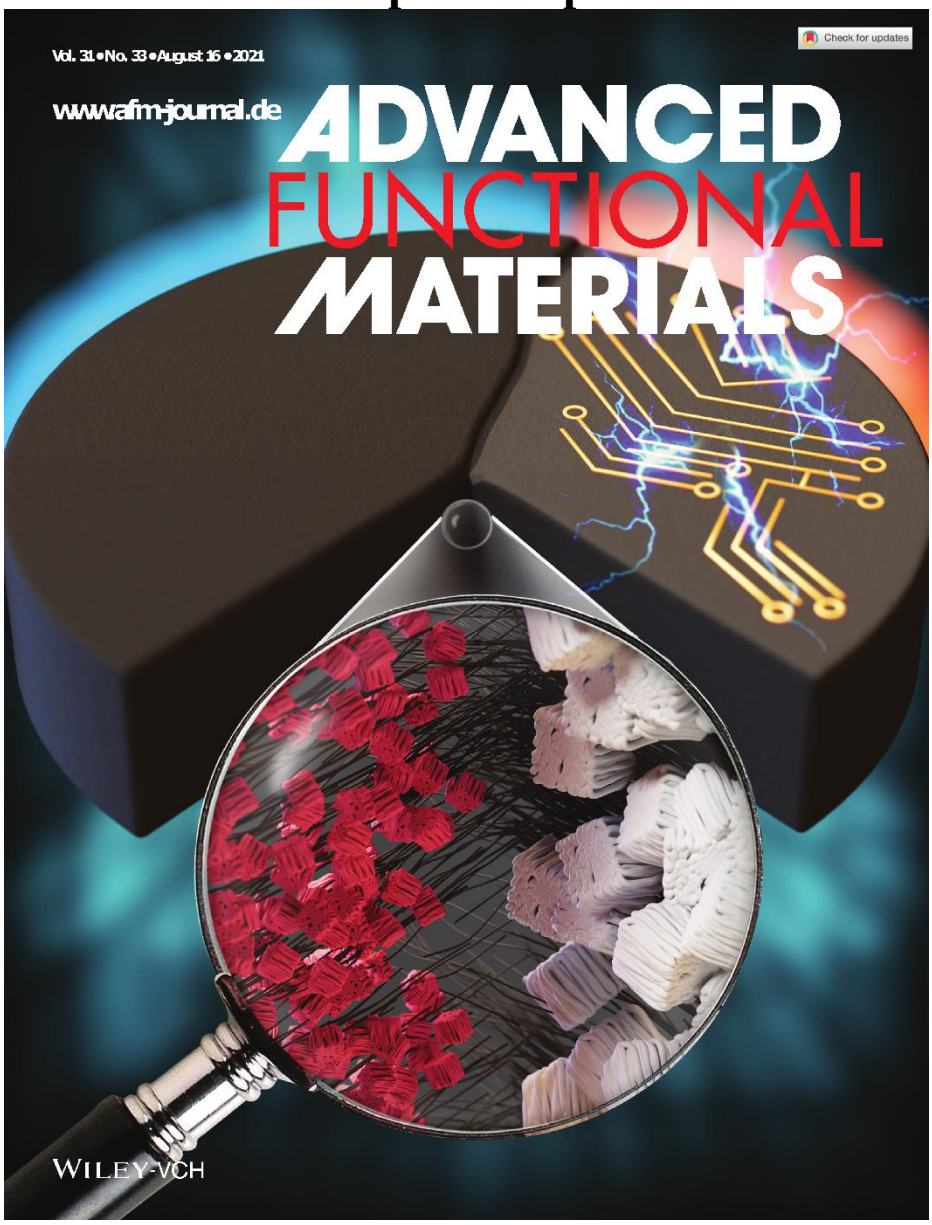

D. Nieto-Castro, F. A.Garcés-Pineda, A. Moneo-Corcuera, I. Sánchez-Molina, J. R. Galán-Mascarós, *Adv. Funct. Mater.* **2021** 2102469.

Abstract

Bistable multifunctional materials have great potential in a large variety of devices, from sensors to information units. However, the direct exploitation of spin crossover (SCO) materials in electronic devices is limited due to their low electrical conductivity. Beyond their intrinsic properties, SCO materials may also work as probes to confer bistability as switchable components in hybrid materials, as controlled by external stimuli acting upon the SCO spin state. Conductors with memory effect may be obtained from the incorporation of SCO probes into a conducting organic polymer matrix. This strategy appeared to be limited by the strict synthetic conditions, since polymerization reactions are harsh enough to attack the redox−unstable SCO component. Because of this, just a few successful examples have been reported. Here a versatile processing protocol is introduced to obtain SCO/conducting polymer composites exploiting a post-synthetic mechanochemical approach that can be applied to any SCO component and any organic polymer. This new protocol allows highly conducting films of polypyrrole, polyaniline, and poly(3,4–ethylenedioxythiophene) (PEDOT) to be obtained, with bulk conductivities as high as 1 $S \cdot cm^{-1}$, and exhibiting a thermal hysteresis in their electrical conductivity above room temperature.

Introduction

SCO materials have been proposed for the construction of memory devices, molecular-based sensors, logic gates and actuators due to features such as wide thermal hysteresis, a colour change and a remarkable increase in lattice volume (≈ 10%).[1–6] The latter showed some of the most successful examples of synergy in SCO/organic polymer hybrids exhibiting large actuation amplitude and stress upon the spin transition, with promising applications in biomimetic artificial muscles.[7–10] One of the most studied SCO materials is $[Fe(Htrz)_2(trz)]_n(BF_4)_n$ (Htrz = 1,2,4–1H–triazole), which preserves its memory effect down to the nanoscale (in 4 nm nanoparticles), an important feature for implementation into electronic devices.[11,12] Regarding electrical conductivity, this compound behaves as an insulator in both phases: LS and HS,[13,14] thus remaining a

bottleneck for its practical use in information storage. Despite this drawback, it has been experimentally confirmed that these nanoparticles show a thermal hysteresis in their electrical properties following the spin transition.[15,16] To lower the electrical resistance in materials exhibiting synergistic SCO phenomena, some synthetic strategies have been proposed,[9,10] as the co-crystallization of SCO cations with conductive anions or the integration of SCO nanoparticles into silver nanowires or in microelectrode devices. Unfortunately, none of these strategies have been successful yet in achieving synergy between SCO hysteresis and electrical conductivity.[17–20]

In 2014, our group reported hybrid conducting materials combining SCO 1D polymers with conducting polypyrrole (PPY), one of the most studied conducting polymers due to its high stability and conductivity, flexibility, low-cost, processability and the possibility of transparency in thin films.[21,22] These composites showed true synergy between SCO and conducting properties, with wide thermal hysteresis (> 40 K) and significant conductivity differences between LS and HS. The synthesis followed the radical polymerization pathway in solution, adding the monomer and the oxidant agent ($[S_2O_8]^{2-}$) to a suspension containing SCO nanoparticles. However, This chemical oxidation was not flexible enough to be applied to most organic conducting polymers as obtained by solution casting,[7] sol-gel techniques,[23] reverse micelle method,[15,24] co-crystallization,[17,19,20] in situ polymerization,[21] spray coating, or electropolimerization.[25] It also severely limits the doping content, as self-controlled by the chemical oxidation process.

In order to obtain two different SCO/PPY composites, as soon as the polymerization reaction started, $[Fe(trz)(Htrz)_2](BF_4)$ or $[Fe(trz–NH_2)_3](BF_4)_2$ were added to the aqueous solution in a 2.5 SC/PPY ratio (in weight). As observed in Figure 1, top, an abrupt increase from a low conductive to a high conductive phase was observed in $Fe(trz)(Htrz)_2](BF_4)$/PPY and $[Fe(trz–NH_2)_3](SO_4)$/PPY) (0.03 $S\cdot cm^{-1}\rightarrow 0.06$ $S\cdot cm^{-1}$ and 0.012 $S\cdot cm^{-1}\rightarrow 0.022$ $S\cdot cm^{-1}$, respectively). Multistability was achieved in a three component film prepared by mixing the two SCO compounds with PPY with a 2.5:2.5:1

ratio (SCO_1:SCO_2:PPY). This composite showed differences in conductivity over 300% and tristability at 360 K (Figure 1, bottom).

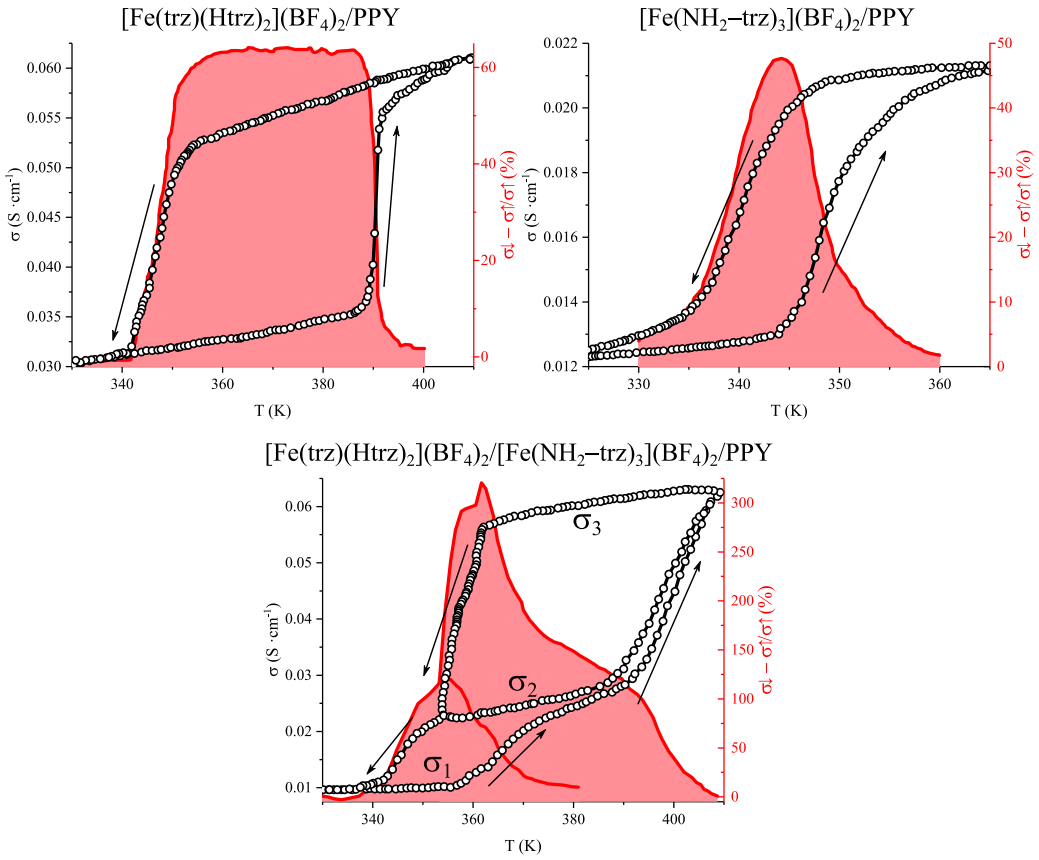

Figure 1. Conductivity (σ) measurements as a function of temperature of Fe(trz)(Htrz)$_2$](BF$_4$)/PPY and [Fe(trz–NH$_2$)$_3$](BF$_4$)$_2$/PPY) (top) and Fe(trz)(Htrz)$_2$](BF$_4$)/ [Fe(trz–NH$_2$)$_3$](BF$_4$)/PPY (bottom). The difference in conductivity during a cooling ($\sigma\downarrow$) and heating ($\sigma\uparrow$) cycle for all the composites is represented with the red filled area.[21]

As many conducting polymers, PPY is prepared from its monomer (pyrrole, C_4H_4NH) by chemical oxidation or electrochemical polymerization. In both cases, the monomer is converted into its cation $C_4H_4NH^+$ which will attack the C–2 carbon of an unoxidized one, producing the dimeric cation $[(C_4H_4NH_2)_2]^{2+}$. The process will be repeated until obtaining $[(C_4H_4NH_2)_2]_n$. The conductive properties of polypyrrole can be modified by

p–doping. In the aforementioned publication, PPY was synthetized by chemical oxidation with $(NH_4)_2[S_2O_8]$ and using p–Toluenesulfonic acid as doping agent. Other important and highly conductive polymers, which could be used instead of PPY, are poly(3,4–ethylenedioxythiophene) (PEDOT), polyaniline (PANI) or polythiophene (PTs), see Figure 2 for structures.

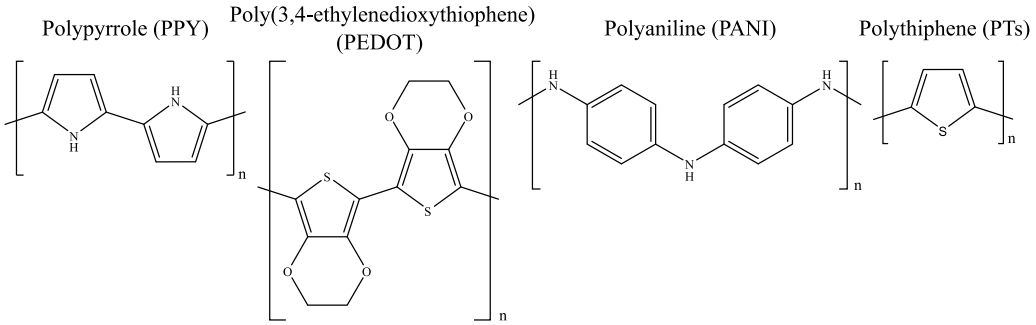

Figure 2. Structure of the organic conducting polymers polypyrrole (PPY), poly(3,4–ethylenedioxythiophene) (PEDOT), polyaniline (PANI) or polythiophene (PTs).

Therefore, we report an alternative production method based in a mechanosynthetic protocol. Many industrial processes use mechanochemistry to homogenize and to reduce particle sizes.[26] We have observed that this solvent–less, waste–free, quick and ecological process yields polymer/SCO composites with strong synergy between electrical conductivity and the spin state of the SCO component.[27] Being a post–synthetic protocol, it offers a general approach to incorporate any organic conducting polymer into the composites, since the polymer can be obtained previously by any suitable technique. Thus, we present here the SCO induced memory effect in the conducting properties of a variety of conducting polymers, such as the electro-polymerized PPY (polypyrrole–paratoluenesulfonate), PANI (polyaniline–sulfate), and PEDOT–PT (poly–(3,4–ethylenedioxythiophene)–paratoluenesulfonate); and the commercially available PEDOT–PSS (poly(3,4–ethylenedioxythiophene) –poly(styrenesulfonate)). Beyond being versatile enough to incorporate a variety of conducting organic polymers, this protocol also yields

hybrid materials with high conductivities (up to 1 $S \cdot cm^{-1}$), thanks to the sequential synthesis introduced in this novel strategy, that separates polymer synthesis and hybrid processing.

Experimental section

$[Fe(trz)(Htrz)_2]_n(BF_4)_n$ (**5**). First, 6.90g of $Fe(BF_4)_2$ (20.4 mmol) and 0.70 g of ascorbic acid (3.9 mmol) were dissolved in 30 mL of water and a solution of 4.60 g of 1,2,4–triazole (66.2 mmol) in 30 mL of water was added dropwise. After 12 h, the pink solution was centrifuged and washed with water several times. The obtained precipitate was dried at 60°C overnight. The solid was homogenized by pestle and mortar, resulting in 6.90 g of 1 (yield = 89%). 0.35 g of **5** were milled for 15 minutes to check the magnetic properties (**5–15**).

$[Fe(NH_2–trz)_3]_n(SO_4)_n$ (**6**). 4.5 g of $FeSO_4$ (16.2 mmol) and 0.70 g of ascorbic acid (3.9 mmol) were dissolved in 30 mL of water and a solution of 3.90 g of 4–aminotriazole (46.4 mmol) in 30 mL of water was added dropwise. After 12 h, the pink solution was centrifuged and washed with water and ethanol several times. The obtained precipitate was dried under vacuum for 5 hours and the powder was homogenized by pestle and mortar, resulting 5.45 g (yield = 83%). 0.35 g of **6** were milled for 15 minutes to check the magnetic properties (**6–15**).

PPY: **PPY** was electrodeposited onto a 6 cm^2 of a clean FTO surface applying 1 V during 40 minutes from a Mili-Q water (45 mL) solution of pyrrole (0.2 M) and p–toluenesulfonic acid (0.5 M). The film obtained was removed by scratching from the glass and ground until homogeneous.

PANI: **PANI** was electrodeposited onto a 6 cm^2 of a clean FTO surface applying 1 V during 40 minutes from a Mili-Q water (45 mL) solution of aniline (0.2 M) and sulfuric acid (0.5 M). The film obtained was removed by scratching from the glass and ground until homogeneous.

PEDOT–PT: **PEDOT–PT** was electrodeposited onto a 6 cm^2 of a clean FTO surface applying 1 V during 40 minutes from an acetonitrile (45 mL) solution of 3,4–ethylenedioxythiophene (0.2 M) and p–toluenesulfonic acid (0.5 M). The film obtained was removed by scratching from the glass and ground until homogeneous.

PEDOT–PSS: CLEVIOS PH 1000 PEDOT–PSS dispersion is commercially available (Heraeus Group). The corresponding solid for ball milling was obtained following the manufacturing protocol to obtain the best conductive properties: 10 mL were dropped on a crystallizing dish and it was dried at 120°C. After 30 minutes, the solvent was evaporated and a film was obtained on the surface of the crystallizing dish. The film was easily removed by scratching with a spatula and ground until homogeneous.

SCO/organic polymer Composites. A conducting organic polymer and **5** or **6** were mixed in the desired ratio (0.12 g in total) and grounded in a 25 mL stainless-steel ball mill mixer with two stainless steel balls (7 g each) for 15 min at a frequency of 25 Hz. These milling conditions were considered optimum since longer milling times may induce decomposition, as previously reported.[28] After ball milling, the as-obtained powders were pressed at 5 metric tons during 5 min using a hydraulic die-press and a micro-macro KBr pellet die of 13 mm diameter pellet die (0.4 GPa), obtaining ≈ 300 μm thick and pellets. The pellets were mechanically split with a cutter in regular fragments for further characterization and analyses (≈ 0.5 × 0.4 cm^2, Figure S5.1). To perform transport measurements (four probe), four copper wires were attached on the surface using silver conductive ink from RS components.

See Annex I for the physical methods used in this chapter: Powder X-ray diffraction (PXRD), Environmental scanning electron microscope (ESEM), Magnetic susceptibility measurements (SQUID), Transport measurements (See also Supporting information).

Results and discussion

Processing and structural characterization

The organic polymer/SCO composites were obtained by mechanochemical milling of the two components mixed in the desired ratio per weight (1:1, 1:3, and 1:5 for organic

polymer/**5**; and 1:5, 1:7.5 and 1:10 for organic polymer/**6**). As organic conducting polymers, we incorporated PPY, PANI, PEDOT–PT and PEDOT–PSS. $[Fe(trz)(Htrz)_2]_n(BF_4)_n$ (**5**) and $[Fe(NH_2–trz)_3]_n(SO_4)_n$ (**6**) were chosen as SCO components. The as-obtained powders were converted into 13 mm thick pellets under pressure (see Experimental Section). The pellets were split into smaller, regular and robust fragments for further characterization and analyses (Figure S5.1). Environmental scanning electron microscopy (ESEM) showed a homogeneous surface and cross-section for all samples (Figure 1 and Figure S5.2 and S5.3). Powder X-ray diffraction (PXRD) patterns for the different composites (Figure S5.4 and S5.5) showed the characteristic diffraction peaks of **5** and **6**, confirming the crystallinity is maintained during the milling process. A slight shift to lower 2θ values and a decrease in the intensity were observed, as expected for these SCO materials, since the ball milling processing provokes small changes in the packing of the 1D chains (Chapter 4).

PEDOT–PSS / $[Fe(trz)(Htrz)_2]_n(BF_4)_n$ (**5**)

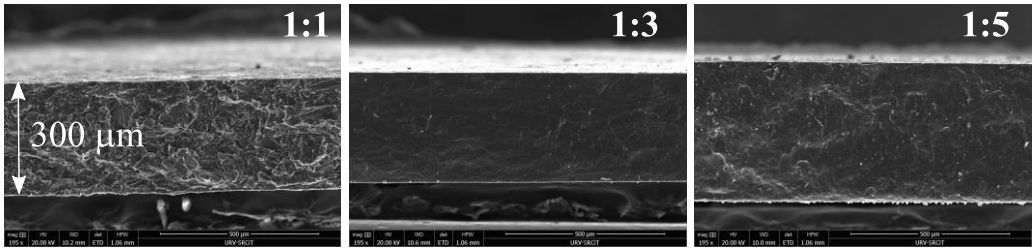

PEDPOT–PSS / $[Fe(NH–trz)_3]_n(SO_4)_n$ (**6**)

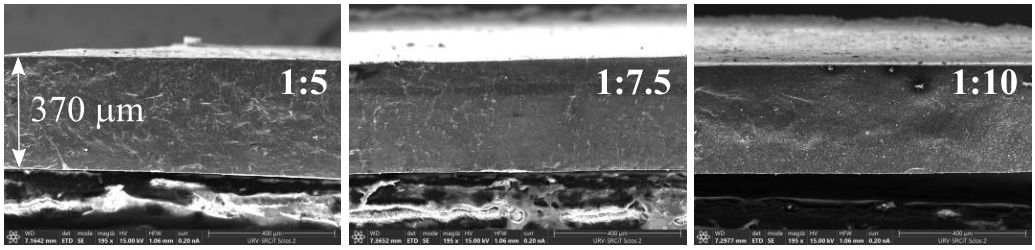

Figure 3. ESEM cross section images of PEDOT–PSS/**5** (top) and PEDOT–PSS/**6** (bottom) composites (ratio polymer:SCO).

Magnetic Properties

The thermal dependence of the spin state of the SCO component in all composites was evaluated by measuring their magnetic susceptibility (χ) in the 250–400 K range. In all

the composites, a small amount of the SCO component appears to be oxidized during the milling protocol, resulting in the appearance of a small paramagnetic impurity which does not participate in the SCO hysteresis cycle (Figure S5.6 and S5.7), as already observed for these SCO materials under milling treatment (Chapter 4).

The as-prepared compound **5** presents a magnetic hysteresis cycle with $T_{1/2}(\uparrow)$ = 380 K and $T_{1/2}(\downarrow)$ = 345 K and a $\chi_m T$ (400 K) = 2.97 emu·K/mol, in good agreement with literature.[29] When **5** is ball milled for 15 min (**5**–**15**), the critical temperatures downshift to $T_{1/2}(\uparrow)$ = 368 K and $T_{1/2}(\downarrow)$ = 329 K, increasing in 4 K the hysteresis width. The $\chi_m T$ (400 K) of **5**–**15** is 2.41 emu·K/mol (Figure S5.8a).[28] The magnetic properties of the organic polymer/**5** composites showed analogous and consistent behavior, with no effect on the nature of the organic polymer (Figure 4 and Table 1). The LS→HS transitions appeared at $T_{1/2}(\uparrow)$ = 380 ± 4 K, and the reverse HS→LS transitions at $T_{1/2}(\downarrow)$ = 325 ± 5 K, resulting in a ≈ 55 K wide hysteresis. $\chi_m T$ (400 K) of all the composites was in between 3 and 2.4 emu·K/mol$_{Fe}$. Interestingly, the amount of remaining paramagnetic impurities in PPY/**5** 1:1, PANI/**5** 1:1, and PANI/**5** 1:3 are much higher than the observed in PEDOT–PT/**5** and PEDOTPSS/**5** (Table 1), suggesting that these conductors protect more effectively **5** toward oxidation during the process, in good agreement with the higher thermal and electrochemical stability reported for PEDOT films when compared with PPY or PANI counterparts.[30,31]

As described in Chapter 4 and observed in Figure S5.8b, when **6** is milled 15 minutes the LS→HS transition temperature increases from 349 K (**6**) to 352 K (**6**–15), while the HS→LS transition temperature downshifts from 329 K (6) to 315 K (**6**–15). In the case of PPY/**6** and PEDOT–PSS/**6**, the shape of the SCO behaviour and the transition temperatures were similar for different organic polymer:**6** ratios (Table 1). However, the transition temperatures of these composites ($T_{1/2}(\uparrow)$ = 328 ± 10 K and $T_{1/2}(\downarrow)$ = 305 ± 4 K) did not match with the ones observed in **6** milled for 15 minutes. Regarding to the polymer protection, the $\chi_m T$ values (≈ 0.30 and 2.45 emu·K/mol$_{Fe}$, in the LS and HS states, respectively) hinted that both polymers effectively protect the SCO polymer. The

lower HS fraction residues can be attributed to a higher resistivity of compound **6** upon short milling times (15 and 30 minutes), also described in Chapter 4.

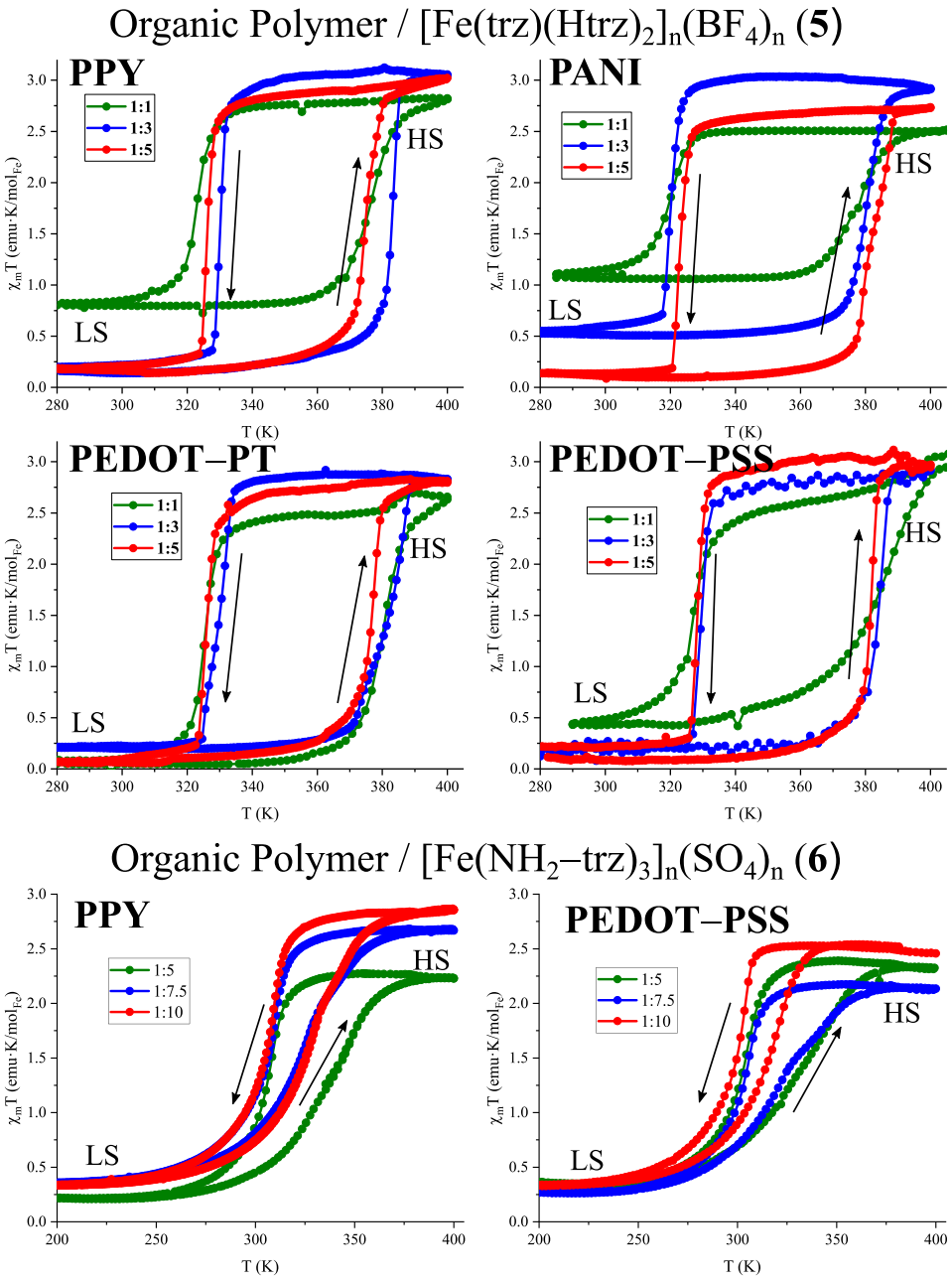

Figure 4. $\chi_m T$ versus T plots of all the organic polymer/**5** (top) and organic polymer/**6** (bottom) composites at a scan rate of 1 K/min in the 280−400 K and 200–400 K regions respectively (ratio Polymer:SCO).

Table 1. Magnetic properties of all the composites. (ratio Polymer:SCO).

Organic Polymer/$[Fe(Htrz)(trz)_2]_n(BF_4)_n$ (**5**)

Sample	Ratio	$T_{1/2}(\uparrow)$ [K]	$T_{1/2}(\downarrow)$ [K]	ΔT [K]	$\chi_m T$(300 K) [emu·K/mol$_{Fe}$]	$\chi_m T$(400 K) [emu·K/mol$_{Fe}$]
PPY/**5**	1:1	376	326	50	0.81	2.81
	1:3	382	330	52	0.16	2.95
	1:5	375	324	51	0.19	2.72
PANI/**5**	1:1	378	320	58	1.07	2.50
	1:3	381	320	61	0.53	2.90
	1:5	383	323	6	0.13	2.72
PEDOT–PT/**5**	1:1	380	325	55	0.08	2.63
	1:3	381	329	52	0.21	2.83
	1:5	377	325	52	0.07	2.79
PEDOT–PSS/**5**	1:1	282	327	55	0.43	2.94
	1:3	383	329	54	0.15	2.91
	1:5	381	328	53	0.09	2.96

Organic Polymer/$[Fe(NH_2{-}trz)_3]_n(SO_4)_n$ (**6**)

Sample	Ratio	$T_{1/2}(\uparrow)$ [K]	$T_{1/2}(\downarrow)$ [K]	ΔT [K]	$\chi_m T$(200 K) [emu·K/mol$_{Fe}$]	$\chi_m T$(400 K) [emu·K/mol$_{Fe}$]
PPY/**6**	1:5	339	308	31	0.21	2.23
	1:7.5	328	309	19	0.36	2.67
	1:10	330	308	22	0.36	2.86
PEDOT–PSS/**6**	1:5	331	303	28	0.36	2.32
	1:7.5	327	305	22	0.26	2.12
	1:10	316	301	15	0.34	2.46

Transport Measurements

Electrical conductivity (σ) was determined with the 4–probe method (see supporting information and Annex I) for all SCO/polymer composites in the 300−410 K range, and also for all polymers as prepared before mechanochemical processing (Figure S5.11). The pristine polymers showed higher conductivity than the corresponding composites (given the insulating behaviour of the increasing SCO content) and followed a typical semiconductor behaviour. The composites were first conditioned during several complete thermal cycles at a scan rate of 10 K/min until two successive cycles were identical, consistent, and reproducible. During these initial cycles, partial desolvation and mechanical stress provoked irreversible changes in conductivity (Figure S5.12 and

S5.13). All pellets were robust enough to complete all the thermal cycling, suffering only the appearance of small surface cracks (Figure S5.14). Once the stable, repeatable regime was achieved, conductivity was measured as a function of temperature at a 1 K/min scan rate (Figure 5).

In general, the transport features of the composites were dominated by the polymer/SCO ratio. Firstly, we will describe the organic polymer/$[Fe(trz)(Htrz)_2]_n(BF_4)_n$ (**5**) composites electric behaviour (Figure 5a–l). For 1:1 composites, only the PEDOT–PT/**5** 1:1 samples showed a small switching in their conductivity (Figure 5g). The 1:1 samples of PPY/**5**, PANI/**5** and PEDOT–PSS/**5** did not show the appearance of any discontinuity in the transport regime, exhibiting typical semiconducting behaviour across the whole temperature range. In contrast, the PEDOT–PT/**5** 1:1 showed a transition between two different conducting states occurring at $T_{1/2}(\uparrow)$ = 372 K and $T_{1/2}(\downarrow)$ = 333 K, thus creating true bistability within a 39 K wide hysteresis loop. These transition temperatures were in good agreement with the $T_{1/2}$ temperatures found in the magnetic measurements (Table 1). The HS state showed higher conductivity, reaching a maximum difference at 360 K, for a HS phase σ_{HS} (360 K) = 1.05 $S \cdot cm^{-1}$ versus LS phase σ_{LS} (360 K) = 0.730 $S \cdot cm^{-1}$.

When the SCO component increased its ratio until 1:3 and 1:5, all samples with all polymers showed an abrupt transition between two distinct conducting states, following the LS↔HS hysteretic behaviour reported in the magnetic measurements (Table 1). All thermal cycles were robust, maintaining consistent values after multiple successive thermal cycles (Figure S5.12).

The nature of the organic polymer is also an important parameter to define the bulk conductivity and its switching (Table 2). PPY/**5** reached a >200% difference for the 1:3 and 1:5 pellets, (Figure 5b and 5c), but with one order of magnitude higher conductivity in the 1:3 sample. Still, the 1:5 sample exhibited an 8 K wider, more robust hysteresis, with the penalty of its higher resistance.

1:3 and 1:5 PANI/**5** composites (Figure 5e and 5f) displayed lower conductivities than the PPY/**5** ones, but a larger enhancement upon the SCO transition. The σ_{HS}/σ_{LS} ratio reaches ≈ 300% for the 1:3 sample and up to a ≈ 1200% in the 1:5 one, with consistent hysteresis width and transition temperatures for both cases, with just 1–2 K differences.

The PEDOT–PT/**5** composites showed a slower increment in σ_{HS}/σ_{LS} ratio at lower SCO ratios, but then from a 150% σ_{HS}/σ_{LS} in the 1:3 sample it grew spectacularly up to ≈2000% in the 1:5 composite (Figure 5h,i), again without any significant differences in width or transition temperatures. These samples exhibited higher conductivities than the PANI/**5** and PPY/**5** composites.

The PEDOT–PSS/**5** samples (Figure 5k,l) showed a much higher enhancement in σ_{HS}/σ_{LS} for the 1:3 (800%) than the rest of 1:3 composites, but then a similar behaviour in the 1:5 sample to the PEDOT–PT analogue. This suggests that this ≈ 2000% σ_{HS}/σ_{LS} ratio may represent a limit for this processing protocol.

To extend the milling protocol to a different 1D SCO polymers, we synthesized organic polymer/**[**$Fe(NH_2–trz)_3]_n(SO_4)_n$ (**6**) hybrid materials (Figure 5m–r). For these composites, higher loadings were necessary to observe hysteresis in the transport properties (1:5, 1:7,5 and 1:10). A smooth transition was observed for PPY/**6** and PEDOT–PSS/**6** 1:5 with a σ_{HS}/σ_{LS} = 20% in both cases. The transition was more abrupt for 1:7.5 and 1:10 ratios with transition temperatures similar than the obtained in the magnetic measurements but different hysteresis shapes (Figure 5 and Table 1). PPY/**6** 1:7.5 exhibited a σ_{HS}/σ_{LS} value of approximately 300%, much higher than in the rest of the composites (≈ 70%). The difference in σ_{HS}/σ_{LS} can be related to the similar amounts of SCO material for 1:7.5 and 1:10 ratios (0,1058 and 0,1090 g of **6** out of 0,12 g, respectively). Moreover, the need of higher SCO loadings than in the organic polymer/**5** composites may be caused by the lower volume expansion of **6**. As described in Chapter 4, the LS→HS transition of **6** is accompanied by an expansion from 648.4 (LS) to 688.5 $Å^3$ (HS), much smaller than the 1146.1 (LS) to 1285.6 $Å^3$ (HS), observed for **5**.

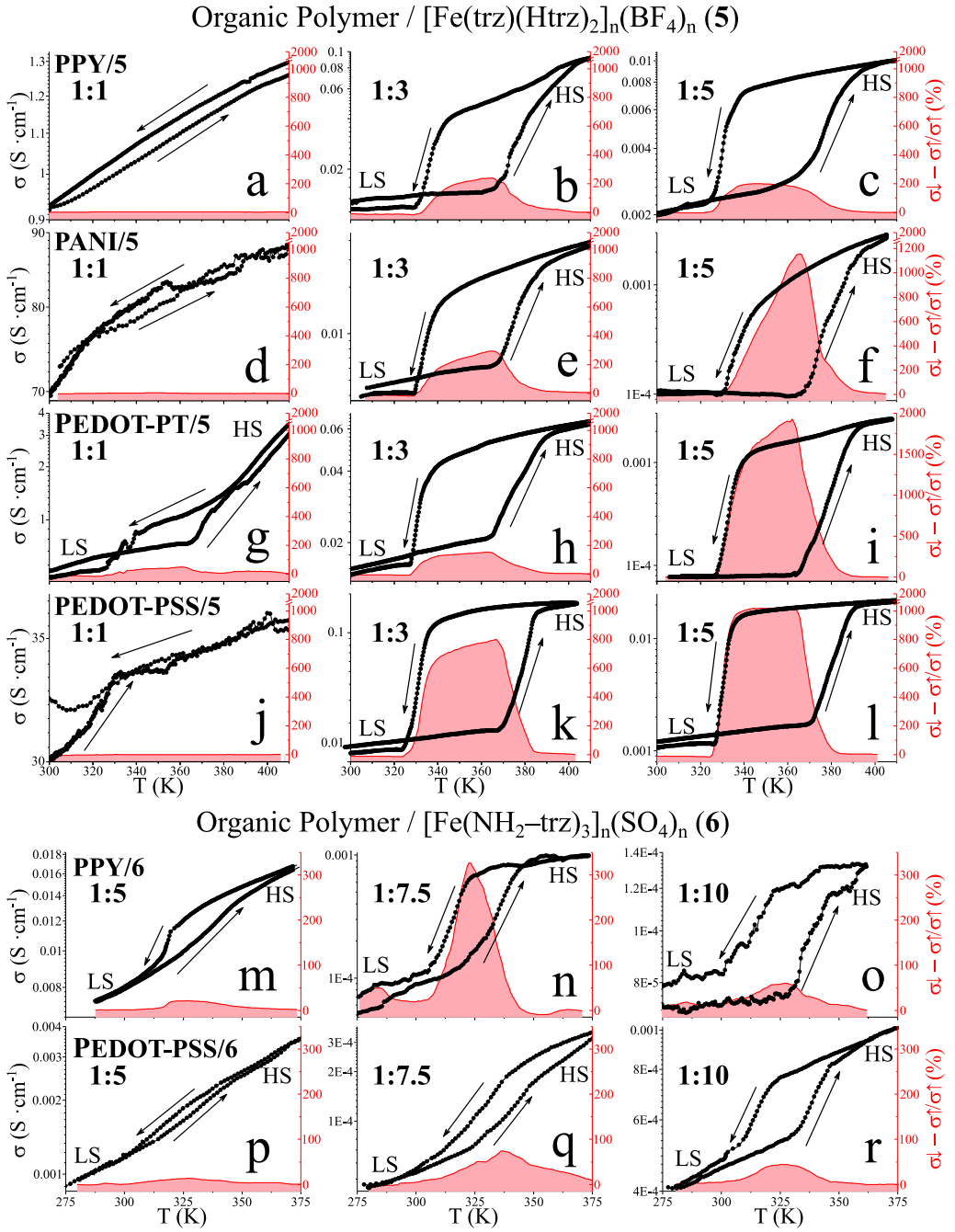

Figure 5. Conductivity measurements for all the organic polymer/**5** (top) and organic polymer/**6** (bottom) composites, with a 1 K min^{-1} scan rate (black dots and line). The difference in conductivity during a cooling ($\sigma\downarrow$) and heating ($\sigma\uparrow$) cycle for all the composites is represented with the red filled area (ratio Polymer:SCO).

Table 2. Conductivity and transition temperatures of all the composites (ratio Polymer:SCO)

Organic Polymer/$[Fe(Htrz)(trz)_2]_n(BF_4)_n$ (**5**)

PPY/**5**	$T_{1/2}(\uparrow)$ [K]	$T_{1/2}(\downarrow)$ [K]	ΔT [K]	σ_{LS} [S·cm^{-1}]	σ_{HS} [S·cm^{-1}]
1:1	–	–	–	0.92739	1.25818
1:3	375	337	38	0.01270	0.09049
1:5	376	330	46	0.00202	0.00989
PANI/**5**	$T_{1/2}(\uparrow)$ [K]	$T_{1/2}(\downarrow)$ [K]	ΔT [K]	σ_{LS} [S·cm^{-1}]	σ_{HS} [S·cm^{-1}]
1:1	–	–	–	70.31854	87.68846
1:3	373	334	39	0.00447	0.03808
1:5	375	337	38	0.00011	0.00282
PEDOT–PT/**5**	$T_{1/2}(\uparrow)$ [K]	$T_{1/2}(\downarrow)$ [K]	ΔT [K]	σ_{LS} [S·cm^{-1}]	σ_{HS} [S·cm^{-1}]
1:1	372	333	39	0.51412	3.13875
1:3	373	331	42	0.01553	0.06246
1:5	377	332	45	0.00008	0.00259
PEDOT–PSS/**5**	$T_{1/2}(\uparrow)$ [K]	$T_{1/2}(\downarrow)$ [K]	ΔT [K]	σ_{LS} [S·cm^{-1}]	σ_{HS} [S·cm^{-1}]
1:1	–	–	–	30.0526	35.36072
1:3	377	331	46	0.01307	0.16320
1:5	374	329	45	0.00009	0.02161

Organic Polymer/$[Fe(NH_2{-}trz)_3]_n(SO_4)_n$ (**6**)

PPY/**6**	$T_{1/2}(\uparrow)$ [K]	$T_{1/2}(\downarrow)$ [K]	ΔT [K]	σ_{LS} [S·cm^{-1}]	σ_{HS} [S·cm^{-1}]
1:5	336	318	18	0.00886	0.01598
1:7.5	334	316	18	0.00006	0.00096
1:10	337	314	23	0.00007	0.00013
PEDOT–PSS/**6**	$T_{1/2}(\uparrow)$ [K]	$T_{1/2}(\downarrow)$ [K]	ΔT [K]	σ_{LS} [S·cm^{-1}]	σ_{HS} [S·cm^{-1}]
1:5	328	317	11	0.00097	0.00307
1:7.5	338	328	10	0.00005	0.00032
1:10	339	314	25	0.00046	0.00096

Given the highly insulating behaviour of the SCO components, we assume transport properties are exclusive of the organic component, as controlled by the efficiency of the hopping transport determined by the supramolecular connectivity among organic polymer chains. Thus, charge transport occurs by incoherent tunneling between localized

sites in the polymer chain. This process can be expressed by the Miller–Abrahams expression (Equation 1):[32]

$$v_{ij} = v_0\, exp(-\gamma \cdot r_{ij})\, exp\left(\frac{-\Delta E_{ij}}{kT}\right) \qquad \text{Equation 1}$$

Where v_0 is the maximum hopping rate, γ is the inverse localization radius, r_{ij} is the separation of the sites with energies E_i, E_j, and E_{ij} is the energy between these two states. We assign the overall increase in conductivity to the internal pressure produced by the expansion of the SCO material inside the composite upon the spin transition into the HS. The SCO volume expansion pushes the organic chains closer, reducing the distance between sites (r_{ij}). Thus, the hopping mechanism is favoured by the shorter interchain distances. It has been well established that the conductivity of organic polymers increases under applied pressure.[33]

In addition, percolation effects could be another plausible hypothesis that has been used in the past to study the behaviour of different SCO devices made of SCO nanoparticles at SiO_2 and graphene monolayers.[16] Percolation theory provides an idea about the optimum conducting filler concentration to convert an insulating matrix to a conductive one.[34]

We found another surprising observation when we fit the conductivity for these semiconducting samples to a simple Arrhenius law, to extract a thermal activation energy (E_a) for each sample and phase (Figure S5.15 and S5.16 and Table S5.2). PPY/**5**, PANI/**5** and PEDOT–PT/**5** exhibit higher E_a in the high conductive region (HS phase) than in the low conductive one (LS), meanwhile PEDOT–PSS/**5** present similar E_a in both regimes. This might seem counterintuitive as a higher activation energy in crystalline semiconductors, directly related with the band gap, typically results in lower overall conductivity,[35] whereas in this case and despite a higher activation energy, the materials are transitioning to a lower resistance phase. This implicitly illustrates the complex synergy between magnetic and transport properties in these composite materials. At the same time, the negligible change in E_a found for the PEDOT–PSS/**5** composites could be at the origin of the significantly stronger enhancement exhibited in the transport

property switching for these composites. In the case of PPY/**6** and PEDOT–PSS/**6**, all the samples exhibited higher E_a in the HS than in the LS state.

Conclusions

We have developed a versatile processing protocol for the preparation of conducting polymer/SCO composites to deliver highly conducting switchable media with robust bistability in their transport properties. This mechanochemical processing can be adapted to any organic conducting polymer, as we demonstrate for a variety of them, including the commercially available PEDOT–PSS. Avoiding a chemical polymerization with oxidants, as in previous examples, we have also increased the scope of SCO materials that can be incorporated. Their chemical stability is guaranteed via this solventless processing, except for some surface oxidation, which does not affect the SCO/transport synergy. Remarkably, the conductivity differences between the LS and HS states are larger, over one order of magnitude in the optimum composites, suggesting that a strong synergy is achieved between both components. The easy synthetic route, the solventless procedure and the ability to use a large range of polymers and SCO materials through this simple and practical protocol opens promising alternatives for the exploitation of SCO probes into electronic devices. We envision that this simple and effective processing method can be exploited also for a variety of SCO complexes, opening interesting venues toward tunable conducting materials with memory effects. The limitations regarding SCO components will depend on the stability of the precursors under mechanochemical treatment, and the synergy will be determined by the electronic and structural changes associated to the spin transition in any given SCO material. In the case of PPY composites, this mechanochemical processing shows better efficiency than chemical methods,[21] where a maximum of 60% increase in conductivity was reported previously.

References

[1] H. J. Shepherd, I. A. Gural'Skiy, C. M. Quintero, S. Tricard, L. Salmon, G. Molnár, A. Bousseksou, Nat. Commun. **2013**, 4, 1.

[2] D. Tanaka, N. Aketa, H. Tanaka, S. Horike, M. Fukumori, T. Tamaki, T. Inose, T. Akai, H. Toyama, O. Sakata, H. Tajiri, T. Ogawa, *Dalt. Trans.* **2019**, 48, 7074.

[3] C. Lefter, R. Tan, J. Dugay, S. Tricard, G. Molnár, L. Salmon, J. Carrey, W. Nicolazzi, A. Rotaru, A. Bousseksou, *Chem. Phys. Lett.* **2016**, 644, 138.

[4] O. Kahn, C. J. Martinez, *Science* **1998**, 279, 44.

[5] H. Voisin, C. Aimé, A. Vallée, T. Coradin, C. Roux, *Inorg. Chem. Front.* **2018**, 5, 2140.

[6] G. Molnár, S. Rat, L. Salmon, W. Nicolazzi, A. Bousseksou, *Adv. Mater.* **2018**, 30, 17003862.

[7] M. D. Manrique-Juarez, F. Mathieu, V. Shalabaeva, J. Cacheux, S. Rat, L. Nicu, T. Leïchlé, L. Salmon, G. Molnár, A. Bousseksou, *Angew. Chem.* 2017, 129, 8186.

[8] S. Rat, V. Nagy, I. Suleimanov, G. Molnár, L. Salmon, P. Demont, L. Csóka, A. Bousseksou, *Chem. Commun.* **2016**, 52, 11267.

[9] Y. C. Chen, Y. Meng, Z. P. Ni, M. L. Tong, *J. Mater. Chem. C* **2015**, 3, 945.

[10] I. A. Gural'Skiy, C. M. Quintero, J. S. Costa, P. Demont, G. Molnár, L. Salmon, H. J. Shepherd, A. Bousseksou, *J. Mater. Chem. C* **2014**, 2, 2949.

[11] A. Rotaru, I. A. Gural'skiy, G. Molnár, L. Salmon, P. Demont, A. Bousseksou, *Chem. Commun.* **2012**, 48, 4163.

[12] A. Rotaru, J. Dugay, R. P. Tan, I. A. Guralskiy, L. Salmon, P. Demont, J. Carrey, G. Molnár, M. Respaud, A. Bousseksou, *Adv. Mater.* **2013**, 25, 1745.

[13] I. Soroceanu, A. Graur, E. Coca, L. Salmon, G. Molnar, P. Demont, A. Bousseksou, A. Rotaru, *J. Phys. Chem. Lett.* **2019**, 10, 7391.

[14] C. Lefter, I. A. Gural'skiy, H. Peng, G. Molnár, L. Salmon, A. Rotaru, A. Bousseksou, P. Demont, *Phys. Status Solidi Rapid Res. Lett.* **2014**, 8, 191.

[15] A. Holovchenko, J. Dugay, M. Giménez-Marqués, R. Torres-Cavanillas, E. Coronado, H. S. J. van der Zant, *Adv. Mater.* **2016**, 28, 7228.

[16] R. Torres-Cavanillas, R. Sanchis-Gual, J. Dugay, M. Coronado-Puchau, M. Giménez-Marqués, E. Coronado, *Adv. Mater.* **2019**, 31, 1900039.

[17] K. Takahashi, H. B. Cui, Y. Okano, H. Kobayashi, Y. Einaga, O. Sato, *Inorg. Chem.* **2006**, 45, 5739.

[18] B. Djukic, M. T. Lemaire, *Inorg. Chem.* **2009**, 48, 10489.

[19] H. Phan, S. M. Benjamin, E. Steven, J. S. Brooks, M. Shatruk, *Angew. Chem.* **2015**, 127, 837.

[20] K. Takahashi, H. B. Cui, Y. Okano, H. Kobayashi, H. Mori, H. Tajima, Y. Einaga, O. Sato, *J. Am. Chem. Soc.* **2008**, 130, 6688.

[21] Y. S. Koo, J. R. Galán-Mascarós, *Adv. Mater.* **2014**, 26, 6785.

[22] G. Prunet, F. Pawula, G. Fleury, E. Cloutet, A. J. Robinson, G. Hadziioannou, A. Pakdel, *Mater. Today Phys.* **2021**, 18, 100402.

[23] C. Lefter, R. Tan, S. Tricard, J. Dugay, G. Molnár, L. Salmon, J. Carrey, A. Rotaru, A. Bousseksou, *Polyhedron* **2015**, 102, 434.

[24] A. Lapresta-Fernández, S. Titos-Padilla, J. M. Herrera, A. Salinas-Castillo, E. Colacio, L. F. C. Vallvey, *Chem. Commun.* **2013**, 49, 288.

[25] A. Enriquez-Cabrera, A. Rapakousiou, M. P. Bello, G. Molnár, L. Salmon, A. Bousseksou, *Coord. Chem. Rev.* **2020**, 419, 213396.

[26] T. F. Grigorieva, A. P. Barinova, N. Z. Lyakhov, *J. Nanopart. Res.* **2003**, 5, 439.

[27] T. Friščić, C. Mottillo, H. M. Titi, *Angew. Chem.* **2020**, 132, 1030.

[28] D. Nieto-Castro, F. A. Garcés-Pineda, A. Moneo-Corcuera, B. Pato-Doldan, F. Gispert-Guirado, J. Benet-Buchholz, J. R. Galán-Mascarós, *Inorg. Chem.* **2020**, 59, 7953.

[29] K. H. Sugivarto, H. A. Goodwin, *Aust. J. Chem.* **1994**, 47, 263

[30] W. Li, Q. Zhang, G. Zheng, Z. W. Seh, H. Yao, Y. Cui, *Nano Lett.* **2013**, 13, 5534.

[31] B. Somboonsub, S. Srisuwan, M. A. Invernale, S. Thongyai, P. Praserthdam, D. A. Scola, G. A. Sotzing, *Polymer* **2010**, 51, 4472.

[32] A. Miller, E. Abrahams, *Phys. Rev.* **1960**, 120, 745.

[33] R. H. Friend, S. Rehmatullah, A. D. Yoffe, D. Jerome, *J. Phys. C Solid State Phys.* **1977**, 10, 1001.

[34] S. Kirkpatrick, *Rev. Mod. Phys.* **1973**, 45, 574.

[35] R. P. Dias, C. S. Yoo, V. V. Struzhkin, M. Kim, T. Muramatsu, T. Matsuoka, Y. Ohishi, S. Sinogeikin, *Proc. Natl. Acad. Sci. U. S. A.* **2013**, 110, 11720.

Supporting Information of Chapter 5.

Mechanochemical Processing of Highly Conducting Organic/Inorganic Composites Exhibiting Spin Crossover–Induced Memory Effect in Their Transport Properties

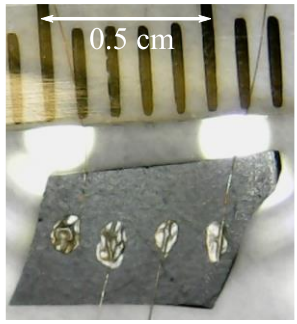

Figure S5.1. Pellet wired

Organic Polymer / $Fe(trz)(Htrz)_2)_n(BF_4)_n$ (**5**)

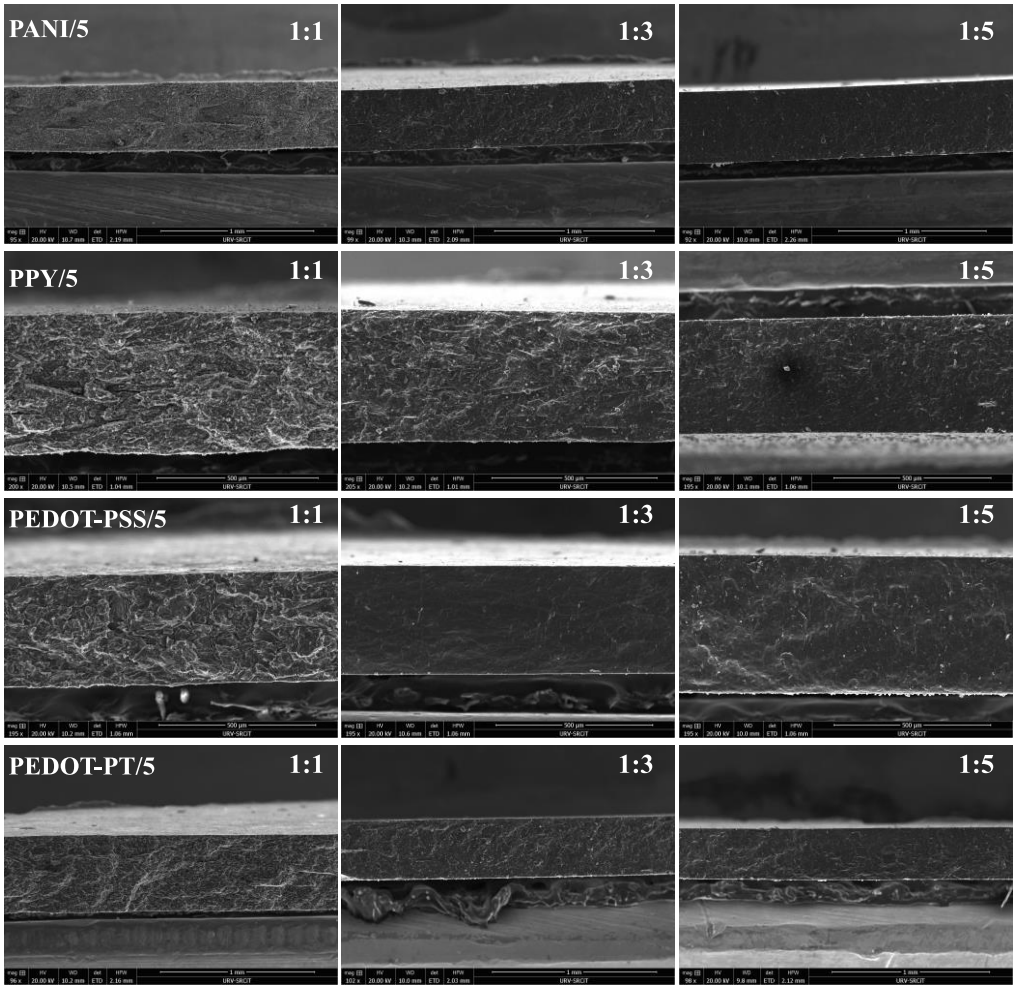

Figure S5.2. ESEM cut section images of organic polymer/**5** composites. (ratio Polymer:SCO)

Organic Polymer / $Fe(NH_2{-}trz)_3)_n(SO_4)_n$ (**6**)

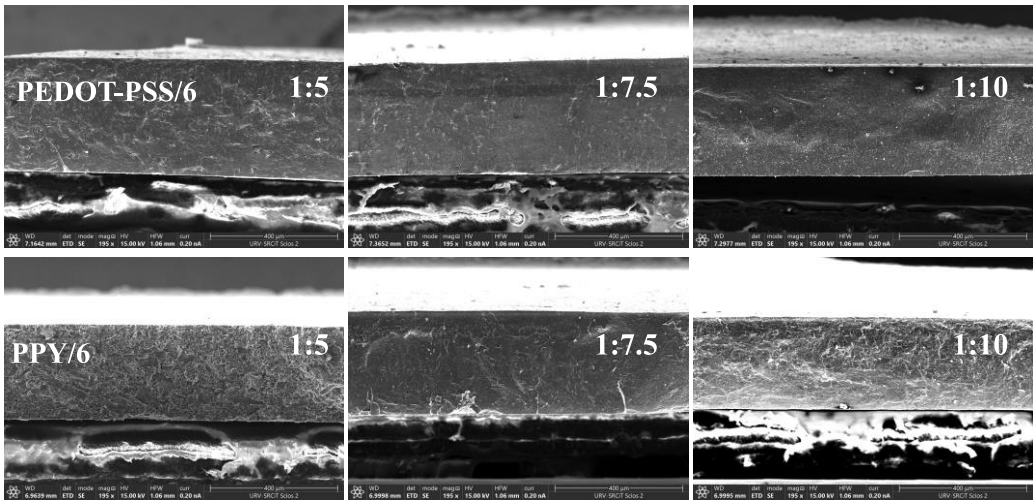

Figure S5.3. ESEM cut section images of organic polymer/**6** composites. (ratio Polymer:SCO)

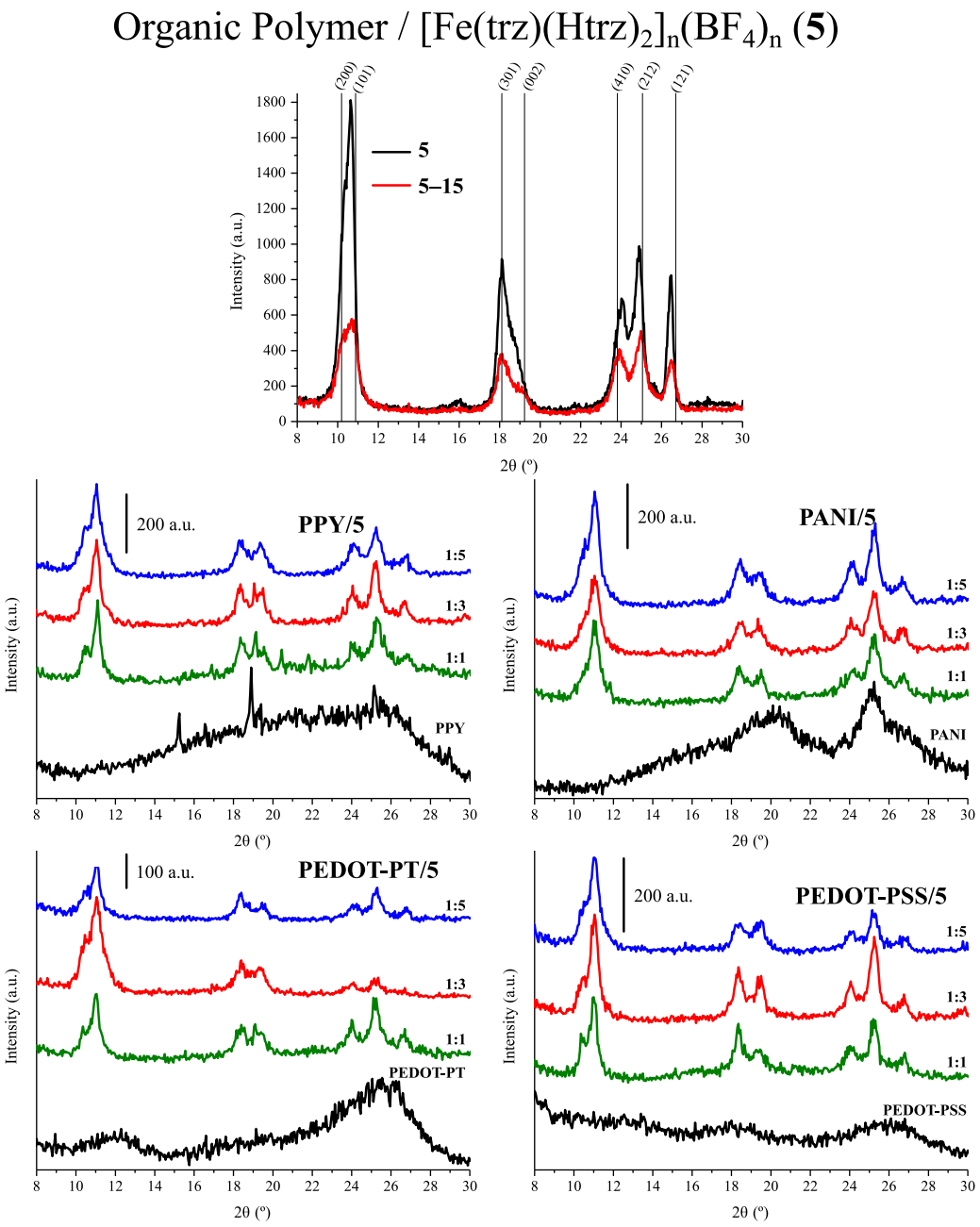

Figure S5.4. PXRD of **5**, **5–15**, the organic polymers and all the organic polymer/**5** composites. (ratio Polymer:SCO)

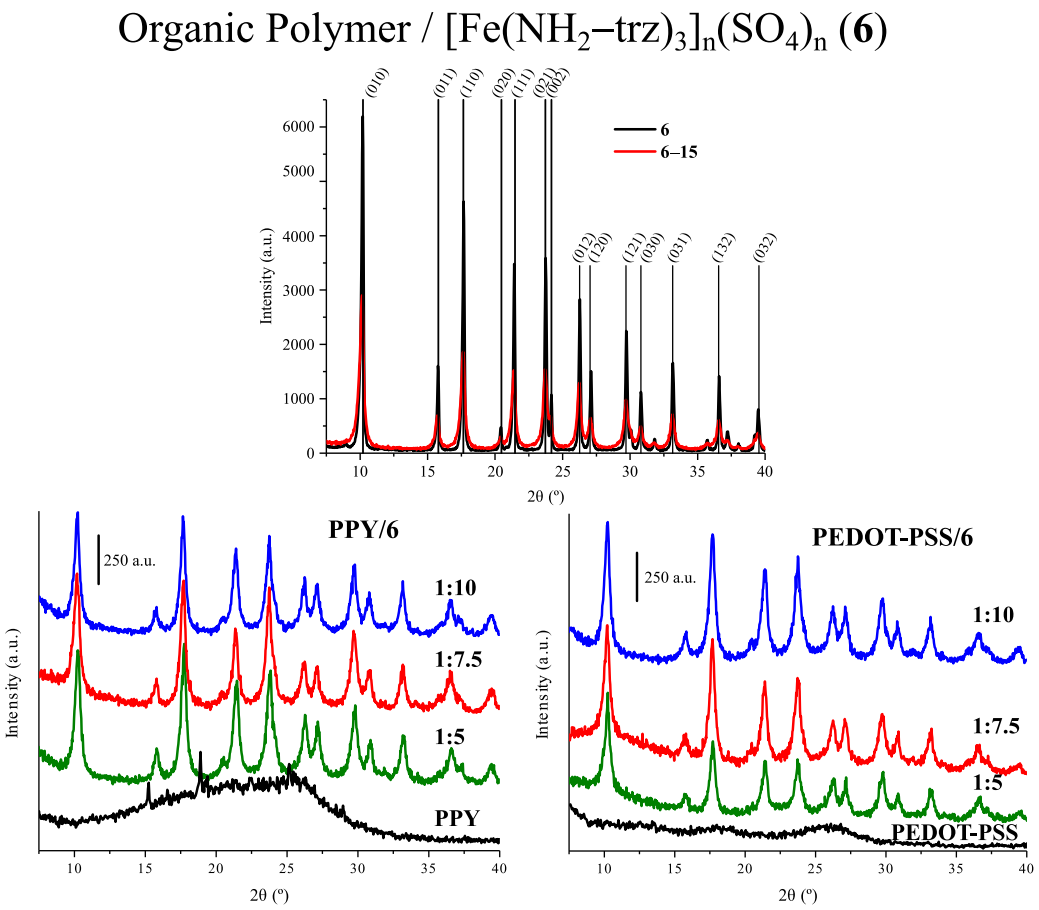

Figure S5.5. PXRD of **6**, **6–15**, the organic polymers and all the organic polymer/**6** composites. (ratio Polymer:SCO)

Temperature-independent paramagnetism corrections

The residual paramagnetism corrections were performed with the Curie-Weiss law (See Annex I).

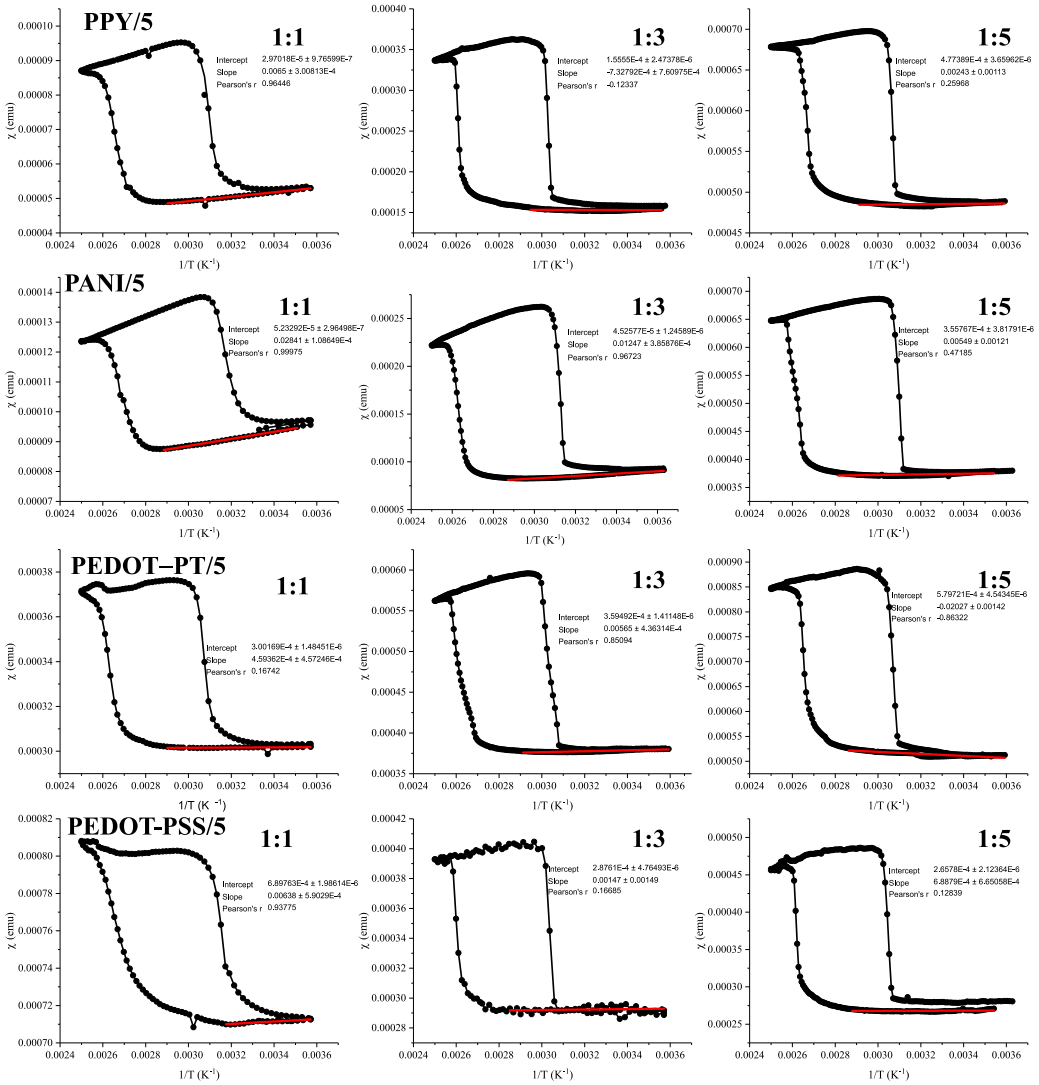

Figure S5.6. χ vs *1/T* of the last cycle and the residual correction (red line) of the organic polymers/**5**.

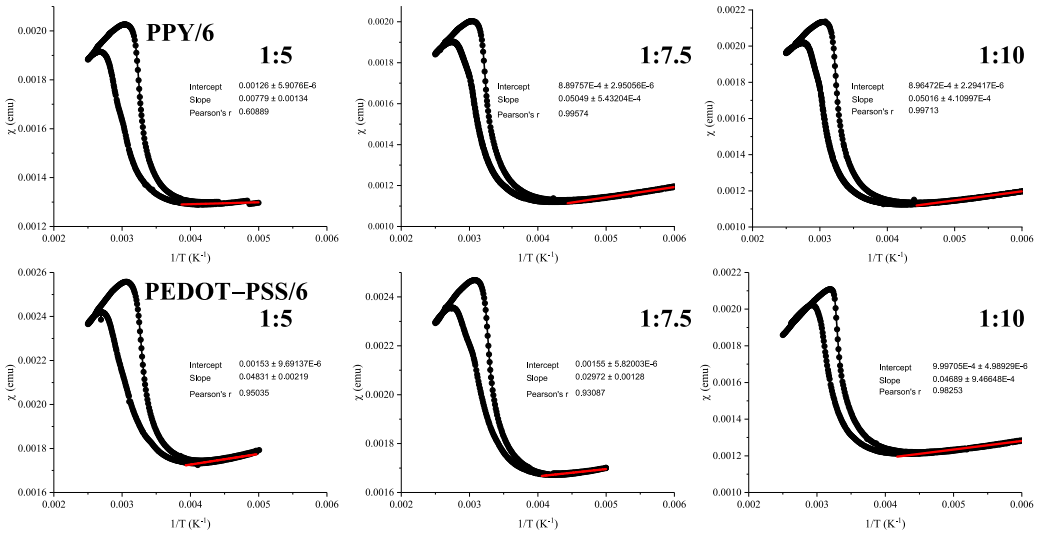

Figure S5.7. χ vs *1/T* of the last cycle and the residual correction (red line) of the organic polymers/**6**.

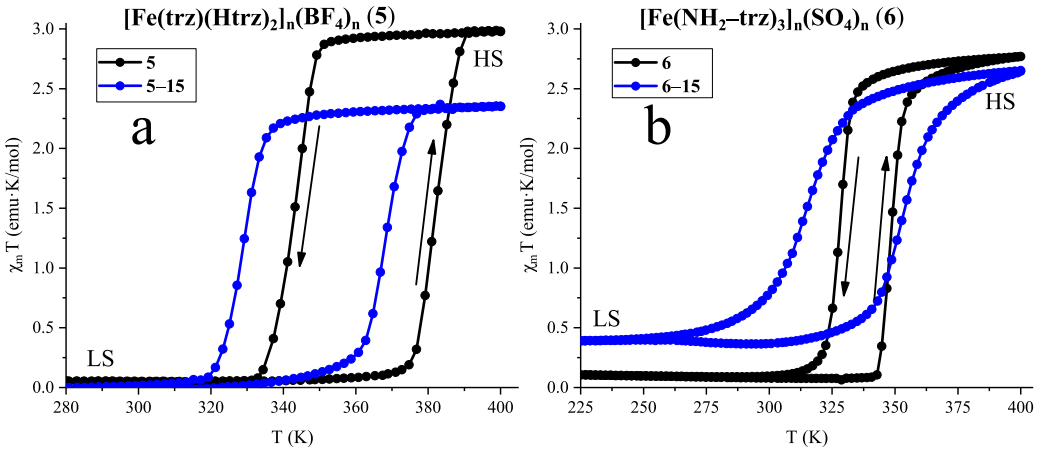

Figure S5.8. $\chi_m T$ vs *T* plot of **5** and **5–15** (a) and **6** and **6–15** (b) at a scan rate of 2 K/min.

The four-probe method

The four-probe method is an electrical impedance measuring technique that uses four equally spaced probes (Figure S5.9) to obtain more accurate measurements of the sheet resistance (R_s) than with the two-probe sensing method. R_s is expressed in ohms per square (Ω/sq).

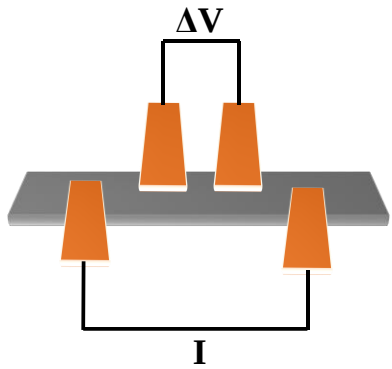

Figure S5.9. Scheme of the four-probe method.

A direct current (DC) is applied between the outer probes (current carriers) and the voltage drop is measured between the inner probes (voltage sensing probes). Resistivity for uniform cross section with a uniform flow electric current can be calculated by:

$$\rho = R \cdot \frac{A}{l} \qquad \text{Equation S5.1}$$

Where R is the electrical resistance, A is the cross-section area (thickness multiplied by width) and l is the length of the film. The units of the resistivity are Ω·m. The conductivity (σ) is the inverse of the resistivity and its units in the international system are siemens per metre (S/m).

If the sample being tested is thicker than 40% of the probe spacing, and additional correction factor is required (Table S5.1). The correction factor depends on the sample thickness (t) and the probe spacing (s).

Table S5.1. Correction parameter for rectangular films**.**

***t*/s**	**Correction Factor**
0.40	0.9995
0.50	0.9974
0.63	0.9898
0.71	0.9798
0.83	0.9600
1.00	0.9214
2.00	0.6336

In our case, all the samples had a s = 1 mm and a t = 0.3 mm. Thus, no correction factor was necessary to apply to the data obtained.

Set up for four-probe method measurements

Electrical conductivity measurements were performed in a set-up with a cryostat (VPF Series, Janis), temperature was monitored with a model 325 cryogenic temperature controller, a current of 10^{-5} A were applied with a Keithley 2400 series sourceMeter and the voltage was measured with a Keithley nanovoltmeter model 2182A.

All the instruments were interconnected with 7007−1 GPIB cables and a GPIB-USB-HS from National Instruments to connect them to a laptop. A LabVIEW program was designed by Dr. Yong Sung Koo, a former postdoctoral researcher in Galán-Mascarós group, to control all the instruments and collect the data (Figure S5.10).

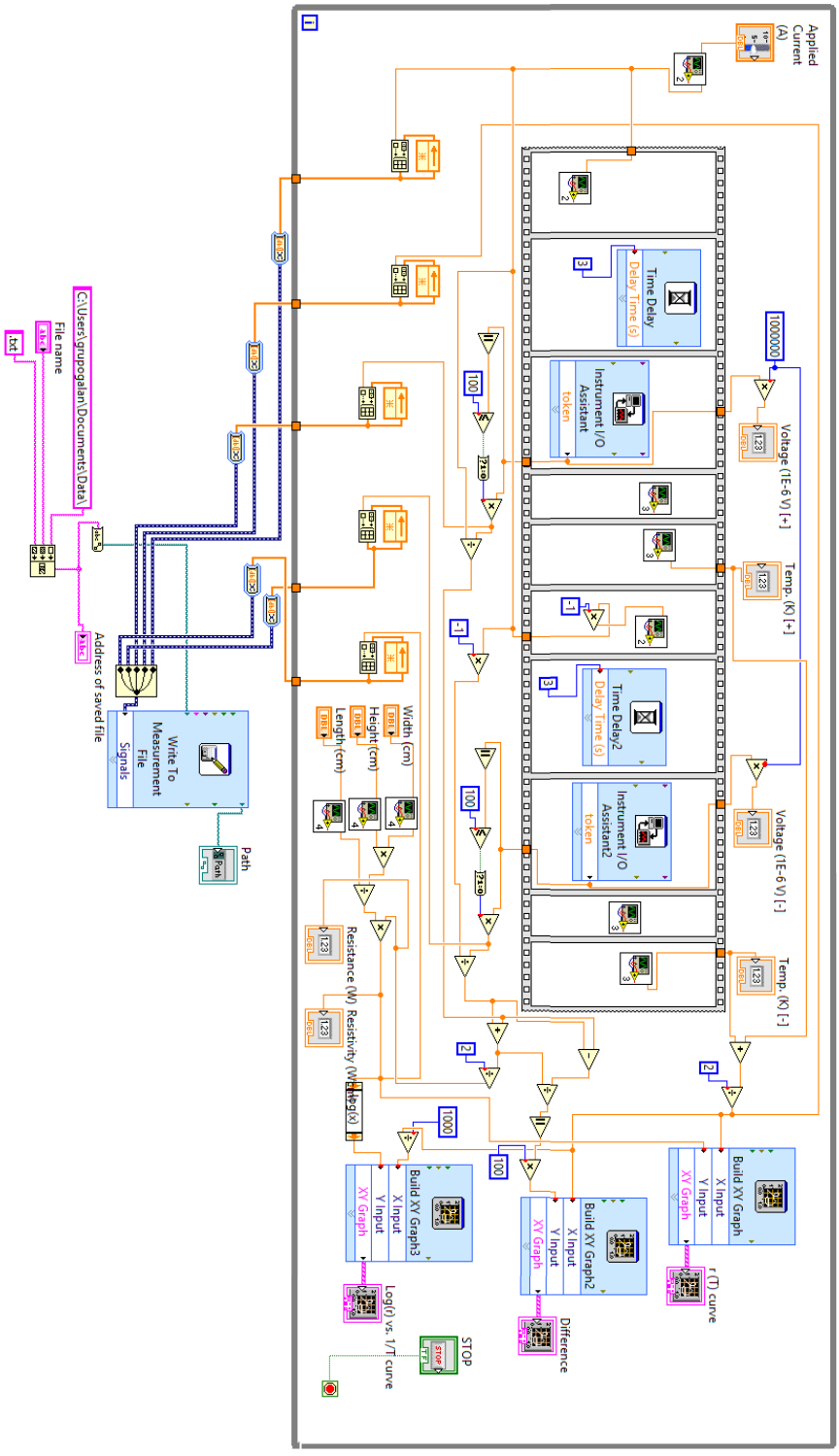

Figure S5.10. LABview program designed for the 4-probe method.

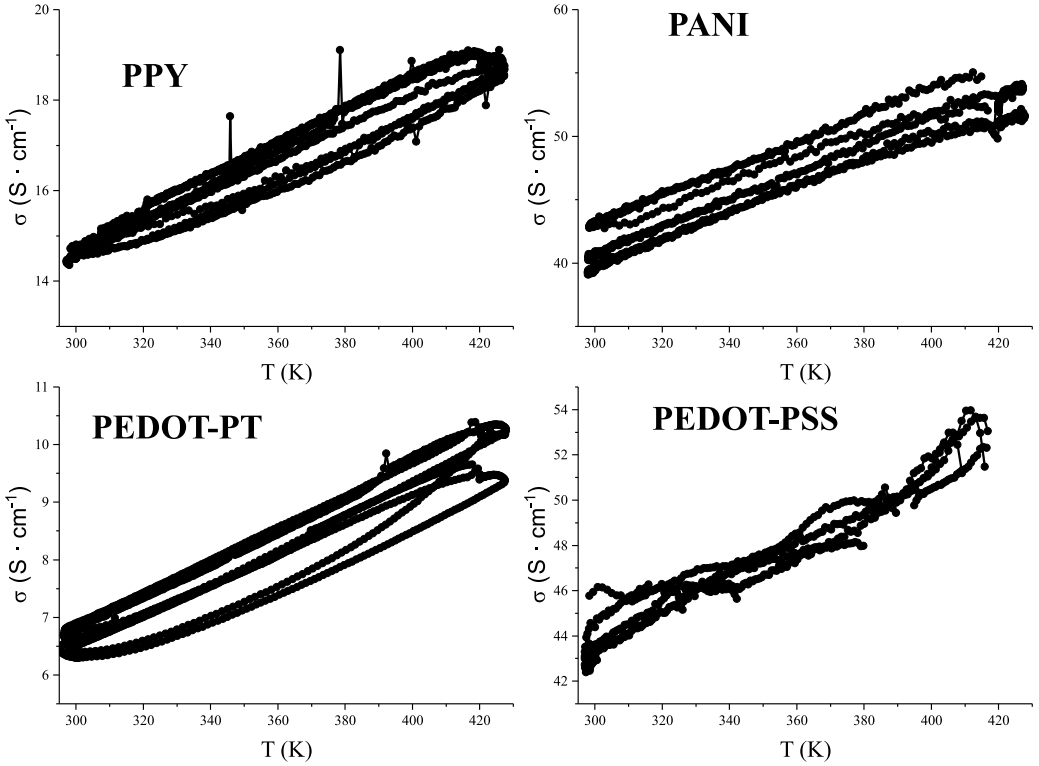

Figure S5.11. Conductivity measurements for the pellets made of the polymer in the 300–420 K range.

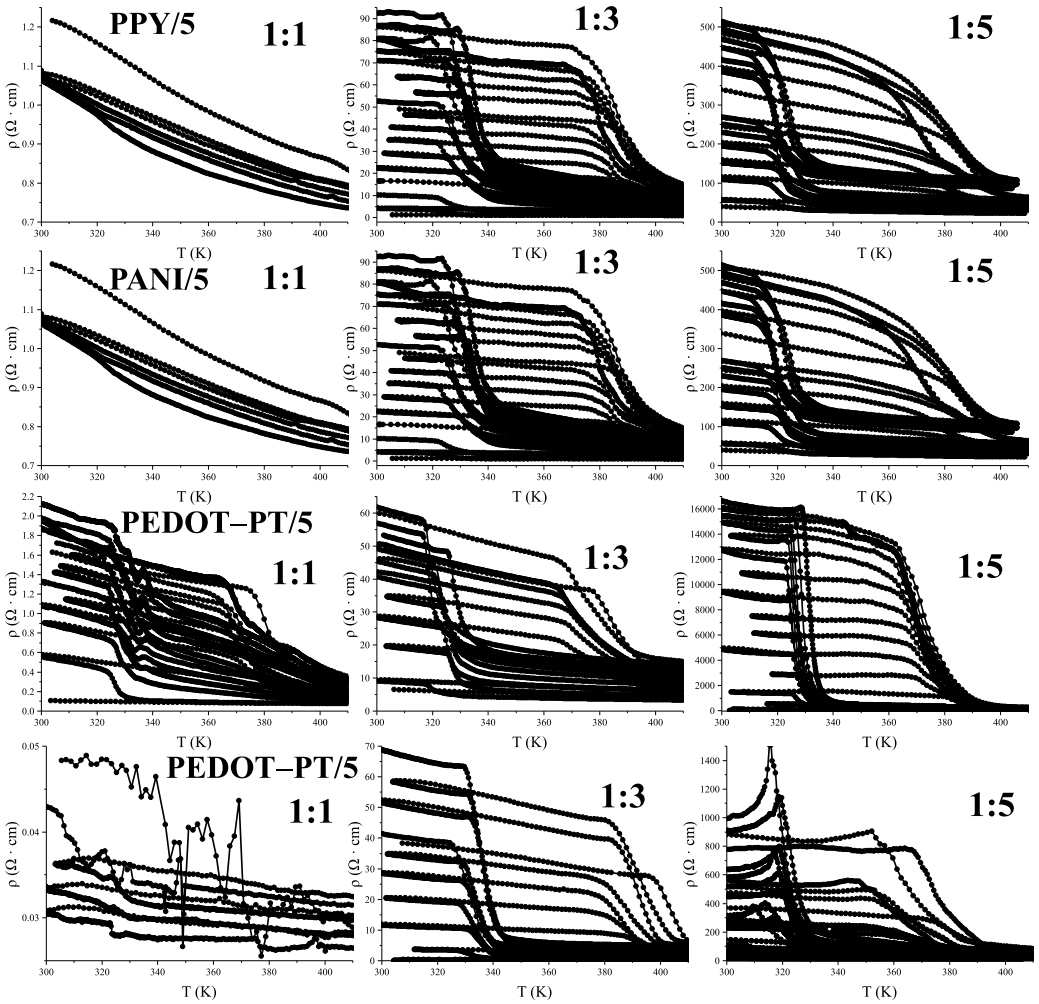

Figure S5.12. Annealing process for organic polymer/**5** composites (Resistivity increases every cycle). (ratio polymer:SCO)

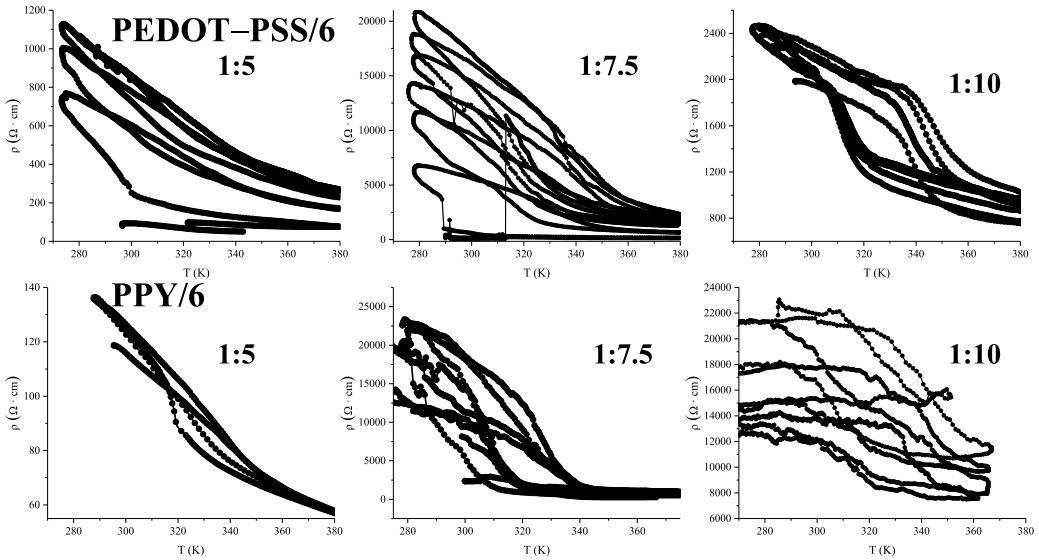

Figure S5.13. Annealing process for organic polymer/**6** composites (Resistivity increases every cycle). (ratio polymer:SCO)

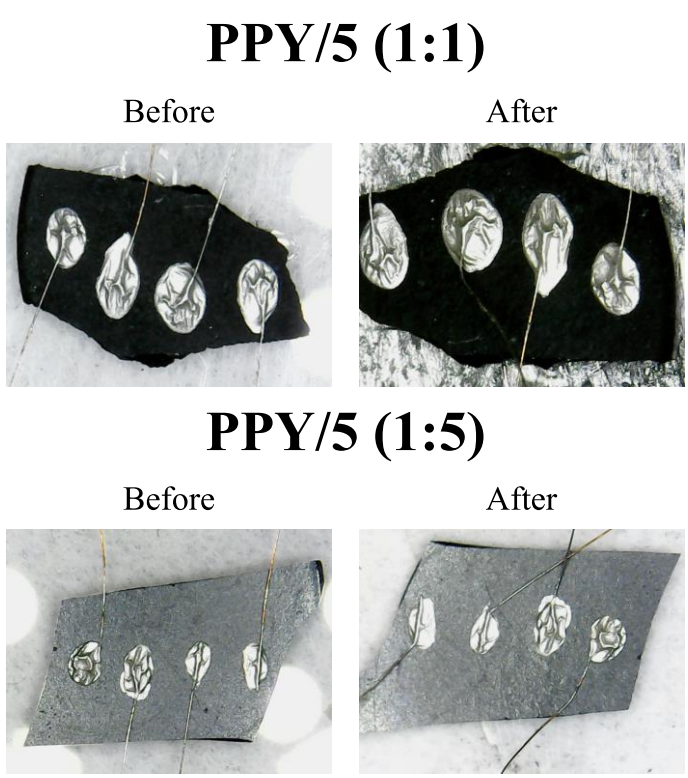

Figure S5.14. Pellets before and after the thermal cycles. (ratio Polymer:SCO)

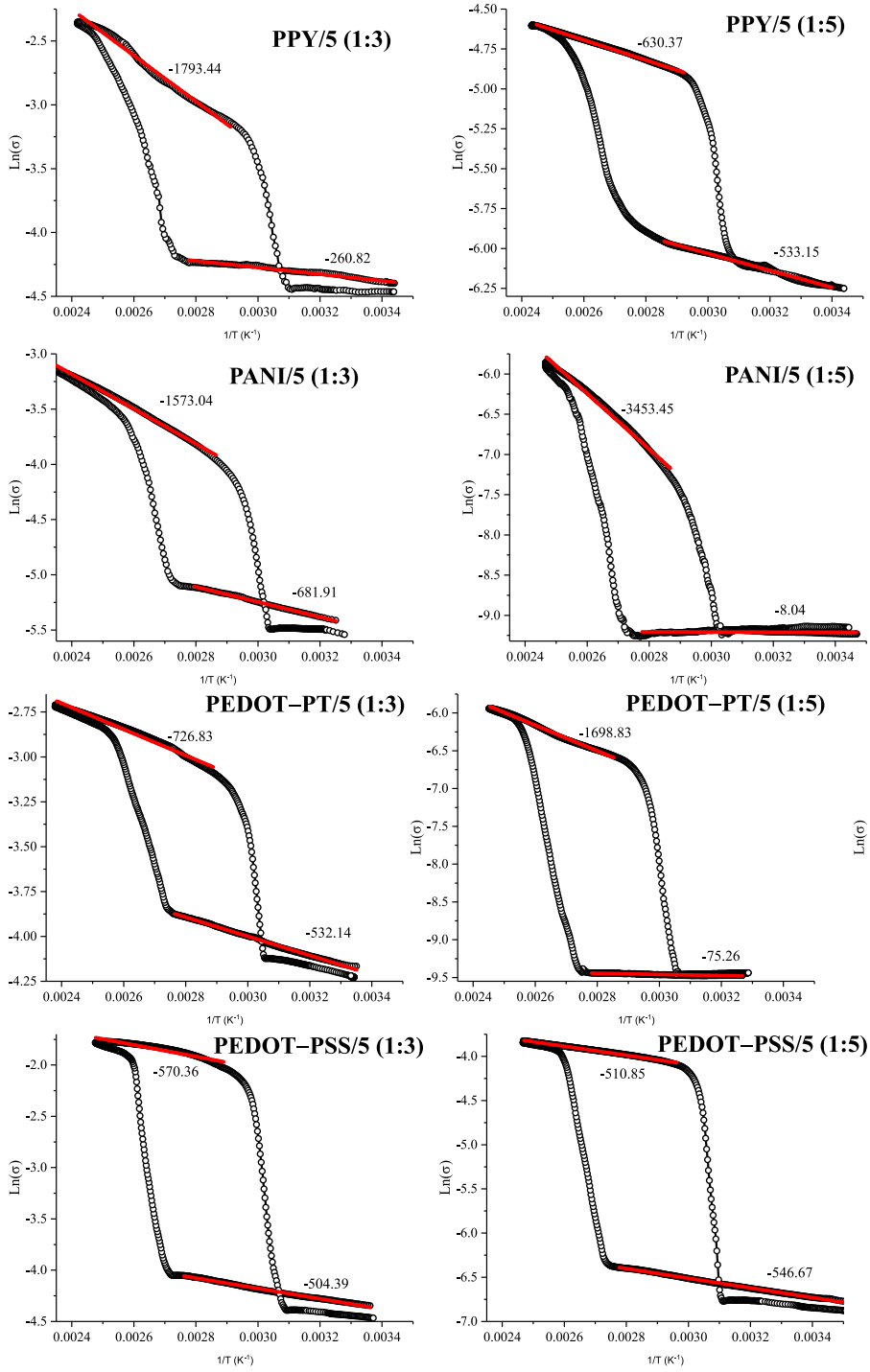

Figure S5.15. Ln (σ) vs *1/T* and Arrhenius fittg for organic polymer/**5** composites. (The numbers indicate the slope of the linear fittings). (ratio Polymer:SCO)

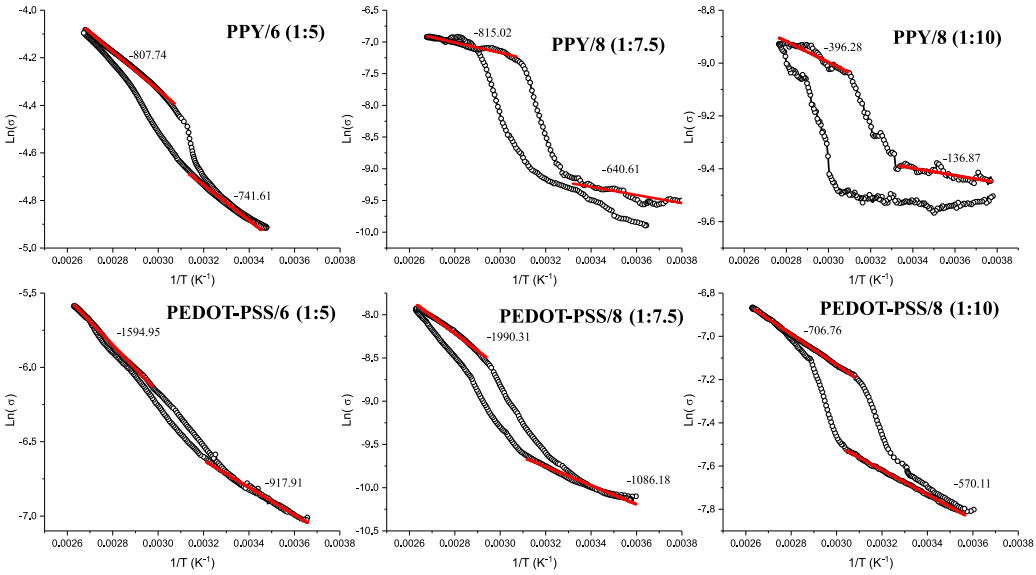

Figure S5.16. Ln (σ) vs *1/T* and Arrhenius fitting for organic polymer/**6** composites (the numbers indicate the slope of the linear fittings). (ratio Polymer:SCO)

The activation energy (*Ea*) can be calculated following the Arrhenius Law:

$$Ln(\sigma) = Ln(\sigma_0) + \frac{-E_a}{k} \cdot \frac{1}{T} \qquad \text{Equation S5.2}$$

Where σ is the conductivity, σ_0 is the DC conductivity pre-exponential factor, E_a the activation energy, k the Boltzmann constant and T the temperature.

Table S5.2. σ_0 and E_a values in HS and LS obtained from the Arrhenius fitting. (ratio Polymer:SCO)

Organic Polymer/$[Fe(trz)(Htrz)_2]_n(BF_4)_n$ (**5**)

PPY/**5**	σ_0 LS	E_a LS (eV)	σ_0 HS	E_a HS (eV)
1:3	0.030	0.0225	7.762	0.1546
1:5	0.012	0.0459	0.047	0.0543
PANI/**5**	σ_0 LS	E_a LS (eV)	σ_0 HS	E_a HS (eV)
1:3	0.041	0.0588	1.806	0.1356
1:5	0.001	0.0007	15.407	0.2976
PEDOT–PT/**5**	σ_0 LS	E_a LS (eV)	σ_0 HS	E_a HS (eV)
1:3	0.091	0.0459	0.984	0.0626
1:5	0.00001	0.0065	0.175	0.1464
PEDOT–PSS/**5**	σ_0 LS	E_a LS (eV)	σ_0 HS	E_a HS (eV)
1:3	0.069	0.0435	0.726	0.0491
1:5	0.008	0.0471	0.077	0.0440

Organic Polymer/$[Fe(NH_2{-}trz)_3]_n(SO_4)_n$ (**6**)

PPY/**6**	σ_0 LS	E_a LS (eV)	σ_0 HS	E_a HS (eV)
1:5	0.094	0.064	0.148	0.069
1:7.5	0.0008	0.055	0.0088	0.0702
1:10	0.0001	0.012	0.0004	0.034
PEDOT–PSS/**6**	σ_0 LS	E_a LS (eV)	σ_0 HS	E_a HS (eV)
1:5	0.025	0.079	0.250	0.137
1:7.5	0.002	0.094	0.071	0.172
1:10	0.003	0.049	0.007	0.061

General conclusions

In this doctoral thesis, different approaches to develop SCO complexes performing abrupt and wide transitions close to room temperature, the modification of previously studied SCO compounds and its implementation into functional composites have been presented.

In chapter 2, we have used a mixing ligand approach to synthetize a neutral SCO chain made of two different triazole-based ligands, one anionic and the other neutral. These ligands individually lead to different dimensional structures (trimeric and 1D polymer structure, respectively). However, together precipitate as a polymeric chain, confirmed via techniques such as PXRD, EDX, SQUID, DSC and elemental analysis.

In chapter 3, a new SCO complex has been mechanosynthesized. This new compound has exhibit different magnetic properties and structure than the solution-synthesized compound with the same precursors. Mechanosynthesis has been postulated as an alternatives synthetic procedure, allowing the obtention of materials that are not reachable via traditional solution-based methods.

In chapter 4, we have found that the SCO phenomena of the 1D $[Fe(trz)(Htrz)_2]_n(BF_4)_n$ and $[Fe(NH_2–trz)_3]_n(SO_4)_n$ can be modified by grinding the compounds via ball milling. The milling protocol induces a recrystallization process that yields a slightly expanded unit cell, stabilizing the HS state and lowering the transition temperatures in both compounds.

In chapter 5, we have developed a versatile processing approach for the preparation of highly conductive composites made of a SCO component ($[Fe(trz)(Htrz)_2]_n(BF_4)_n$ or $[Fe(NH_2–trz)_3]_n(SO_4)_n$) and a conductive organic polymer (PEDOT, PANI or PPY). The composites obtained showed chemical stability and, more importantly, strong synergy between both components, observing remarkable differences in the conductivities between the LS and HS states.

Annex I. Physical Methods

Inductively coupled plasma mass spectrometry (ICP-MS)

Inductively coupled plasma optical emission spectrometry (ICP-MS) was performed ex situ at the Atomic and Molecular Spectroscopy Service of the Universidad de Valencia. Solids were digested by immersion in HNO_3. Analysis was performed on an Inductively coupled plasma mass spectrometry (ICP-MS).

Elemental analysis

CHNS analysis was performed using Flash Smart Eager 200 Elemental Analyzer.

Thermogravimetric Analysis (TGA)

TGA analysis were performed using a TGA/SDTA851 Mettler Toledo with a MT1 microbalance under nitrogen (5 °C·min^{-1} scan rate).

Differential Scanning Calorimetry (DSC)

DSC analyses were performed using a Mettler Toledo/DSC822e instrument with a heating rate of 5, 2, and 1 K/ min in a nitrogen stream. The recorded heat flows were processed by the standard procedure to obtain the mass heat capacity of the sample.

Infrared spectroscopy (IR)

IR spectra were collected with a FTIR Bruker spectrometer model Alpha equipped with an ATR accessory.

Energy Dispersive X-ray (EDX) / Field Emission Scanning Electron Microscopy (FESEM)

FESEM data were obtained using Scios 2 dual Beam (thermofisher scientific) equipment under high-vacuum conditions with a Large-Field Detector at 30 kV. With a coupled EDX detector (Quanta 600 equipment from FEI) a detection area of 100 mm2 was scanned during FESEM. Spectra were analyzed with the Pathfinder software.

Environmental Scanning Electron Microscope (ESEM)

ESEM data were obtained with a QUANTA600 instrument from the FI Company under high vacuum conditions with a large-field detector at 20 kV.

Powder X-ray Diffraction (PXRD)

PXRD measurements were made using a Siemens D5000 diffractometer (Bragg−Brentano parafocusing geometry and vertical θ−θ goniometer) fitted with a curved graphite diffracted-beam monochromator, incident and diffracted-beam Soller slits, a 0.06° receiving slit, and a scintillation counter as a detector. The angular 2θ diffraction range was between 5° and 50°. The data were collected with an angular step of 0.05° at 10 s per step and sample rotation for all the compounds but $[Fe(NH_2trz–trz)_3]_n(SO_4)_n$ (**8**) in chapter 4. A low background Si(510) wafer was used as sample holder. Cu Kα radiation was obtained from a copper X-ray tube operated at 40 kV and 30 mA. This diffractometer was also used to characterize the compounds at different temperatures in chapters 2 and 3. Diffractograms of $[Fe(NH_2–trz)_3]_n(ClO_4)_n$ (**1**) were taken at 113 K (LS) and 300 K (HS) under vacuum under vacuum ($5.2 \cdot 10^{-3}$ mbar) to avoid ice crystallization . Diffractograms of $[Fe_3(L)_6(H_2O)_6](Me_2NH_2)_6$ (**2**), $[Fe(L)(NH_2–trz)_2]$ (**3**), $[Fe(L)_3]_n(Me_2NH_2)_{4n}$ (**4**)and $[Fe(L)(NH_2–trz)_2]$ (**5**) were taken at 300 K (LS) and 400 K (HS).

In chapter 4, The PXRD patterns at different temperatures were measured on a Bruker Apex II Duo single crystal diffractometer using Cu Kα radiation; a diffractogram was taken every 5 K in the 4−50° range with a step of 0.02°, and the temperature ramp was at a rate of 5 K/ min.

Single crystal X-ray diffraction (SCXRD)

Single crystal X-ray diffraction measurements were performed on a Bruker-Nonius diffractometer with an APPEX 2 4 K CCD area detector at 100 K. Crystal structure solution and refinement were performed using SHELXTL Version 6.10.

Extended X-ray absorption fine structure (EXAFS)

EXAFS measurements were conducted at the BL22-CLAESS beamline at ALBA Synchrotron in Spain. The X-ray was produced from a storage ring at energy of 3 GeV with an electron current of 200 mA. The beamline source was wiggle based and was able to exhibit theoretical maximum energy of 70 keV. We ran the experiment for the absorption edge of Fe at 7.112 keV at 300 K.

For this measurement, pellets of $[Fe(NH_2–trz)_3]_n(SO_4)_n$, $[Fe_3(L)_6(H_2O)_6](Me_2NH_2)_6$ (**2**) and $[Fe(L)(NH_2–trz)_2]$ (**3A**) were made by mixing 27 mg, 32 mg and 27 mg of the respective compounds with boron nitride until a total weight of 120 mg. The powder was homogenized with an agate mortar for 15 minutes and converted into pellets by pressing at 0,37 GPa for 5 minutes.

Nuclear Magnetic Resonance (NMR)

^{1}H NMR spectra were recorded on a Bruker Fourier 300 NMR spectrometer. The residual solvent peak was used as internal reference.

Magnetic Susceptibility Measurements

The magnetic properties of all the samples were measure in different temperature ranges using a Quantum Design Magnetic Property Measurement System (MPMS) SQUID magnetometer. The temperature control module (TCM) of this equipment allows to measure magnetic properties between 1.9 and 400 K and the superconducting magnet with two Josepshon junctions (DC) can generate magnetic fields between −7 and 7 Teslas. In all our samples, the magnetif field applied was of 0.1 T (1000 Oe).

In chapters 3,4 and 5, as the residual paramagnetic impurities in the SCO systems are very high, we experimentally subtracted the residual constant for every sample using the Curie−Weiss law:

$$\chi = \frac{C}{(T - \theta)} + \chi_{residual}$$

where C is the Curie constant, θ is the correction term or Weiss constant and $\chi_{residual}$ is the magnetic susceptibility of the residual temperature-independent paramagnetism. The residual corrections corrections were performed sustracting the intercept in the x axis of the plots to the original χ values.

Transport Measurements

Transport properties were measured by a 4-point probe method with a sourcemeter (2400, Keithley) and nanovoltmeter (2182A, Keithley) in a liquid nitrogen cryostat (VPF Series, Janis).

UNIVERSITAT
ROVIRA i VIRGILI